Highly active chromosome regions preferentially associate with two perispeckle networks that partition the interchromatin space

Authors:

Neha Chivukula Venkata[1], Jiah Kim[1], Gabriel Faber[2], Saireet Misra[1], Atabek Bektash[3,4], Pankaj Chaturvedi[1], Gabriela Hernanadez[1], Joseph Dopie[1], Masato T. Kanemaki[3,4,5], Kyu Young Han[6], Yaron Shav Tal[2] and Andrew S. Belmont[1,7,8]

Affiliations

1. Department of Cell and Developmental Biology, University of Illinois at Urbana-Champaign, Urbana, IL
2. The Mina and Everard Goodman Faculty of Life Sciences, Bar-Ilan University, Ramat Gan 5290002, Israel.
3. National Institute of Genetics, Research Organization of Information and Systems (ROIS), Mishima, Shizuoka 411-8540, Japan.
4. Graduate Institute for Advanced Studies, SOKENDAI, Mishima, Shizuoka 411-8540, Japan
5. Department of Biological Science, Graduate School of Science, The University of Tokyo, Tokyo 113-0033, Japan
6. CREOL, The College of Optics and Photonics, University of Central Florida, Orlando, FL, USA
7. Center for Biophysics and Quantitative Biology, University of Illinois at Urbana-Champaign, Urbana, IL
8. Carl R. Woese Institute for Genomic Biology, University of Illinois at Urbana-Champaign, Urbana, IL

Key Words:

Genome organization, active chromatin, interchromatin compartment, nuclear speckles

Abstract

A subset of highly active chromosomal "hot zones" reproducibly positions adjacent to nuclear speckles (NS). Genes within these regions amplify their expression only with NS contact. However, gene expression differences inversely correlate with differences in NS distance, genome-wide. We hypothesized the existence of additional gene expression "niches" away from, but spatially correlated with, NS. Here we report the identification of two dynamic perispeckle patterns of protein concentrations extending outwards from NS and persisting even after NS are eliminated. Highly active chromosome regions which weakly associate with NS instead show close, NS-independent association with these perispeckle patterns. Additionally, transcripts from model intron-containing versus intronless genes associate differentially with these two patterns. While genes within NS-associated genomic regions are predominantly downregulated upon NS depletion, genes associated with perispeckle patterns are biased towards upregulation. We suggest the interchromatin space is partitioned into additional gene expression “niches”- surrounding and extending from NS - that may be involved in mRNA and gene dynamics.

Introduction

Nuclear speckles (NS) were first suggested to act as a gene expression hub for a subset of active genes based on a survey of ~20 active genes using fluorescence in situ hybridization (FISH) (Smith et al., 1999; Hall et al., 2006). Over the past several years, this model has now been validated by multiple orthogonal genome-wide approaches, including TSA-seq, SPRITE, and highly multiplexed immuno-FISH (Quinodoz et al., 2018; Chen et al., 2018; Su et al., 2020; Takei et al., 2021; Zhang et al., 2021; Gholamalamdari et al., 2025). A distinct subset of chromosomal regions- GC-rich, gene-dense, and enriched with shorter genes with fewer introns and house-keeping genes- show high frequency association with NS and mean NS distances of just several hundred nm (Chen et al., 2018). While several developmentally regulated genes have been shown to move from the nuclear lamina to NS after their gene activation, unexpectedly most of these Speckle-Associated Domains (SPADs) are highly conserved across multiple cell types (Zhang et al., 2021; Takei et al., 2021, 2023; Bhat et al., 2024). The most highly expressed genes show a pronounced enrichment in SPADs, as do CTCF binding sites, super-enhancers, and active marks such as H3K27ac, H3K9ac, and K3K79me3 (Chen et al., 2018; Yu et al., 2023b; Wang et al., 2021; Joo et al., 2023). In addition to this correlation of high levels of gene expression with NS association, live-cell imaging revealed a striking increase in *HSPA1* gene expression occurring within several minutes of gene movement and contact with NS (Khanna et al., 2014; Kim et al., 2020). Similar “amplification of gene expression” with NS association was inferred for several genes flanking the *HSPA1* locus (Kim et al., 2020), for the *HSPH1* gene (Zhang et al., 2021), and for several hundred p53-

responsive genes (Alexander et al., 2021). Additionally, NS proximity has been shown to increase the efficiency of RNA splicing (Bhat et al., 2024).

While these results firmly establish NS as a nuclear hub for a subset of active genes, they raise the obvious next question of whether other nuclear compartments might similarly act as a hub for different subsets of active genes. Several previous observations led us to speculate that there might be additional nuclear compartments which act as local niches for gene expression.

First, we observed two types of chromosome regions with similarly elevated levels of gene expression; both types of these gene expression "hot-zones", on average several hundred kbp in size, aligned with SON TSA-seq local maxima (Chen et al., 2018) (Gholamalamdari et al., 2025). Whereas high-amplitude, "Type I" SON TSA-seq peaks corresponded to chromosome regions strongly associated with NS, low-amplitude, "Type II" SON TSA-seq peaks corresponded to chromosome regions with weak association with NS (Gholamalamdari et al., 2025). Second, based on the shapes of the Type I SON peaks, aligned with corresponding Lamin B TSA-seq valleys, we inferred chromosome trajectories extending from the nuclear lamina and terminating adjacent to NS for the several hundred to thousand kbp lying between Type I SON TSA-seq peaks and the nearest LAD, as validated for several trajectories by DNA FISH (Chen et al., 2018). By analogy, we hypothesized similar chromosome trajectories extending from the nuclear lamina towards an unknown nuclear body/compartment that Type II SON TSA-seq peaks would associate with instead of NS. Third, chromosome regions shifting in different cell types from far to moderate distances to NS showed similar biases towards increases in gene expression as other chromosome regions that

97 shifted from moderate to near distances to NS (Zhang et al., 2021). Fourth, live-cell
98 imaging revealed repeated nucleation and then movement of small NS towards larger
99 NS within DNA-depleted channels connecting the NS (Kim et al., 2019). Despite the
100 known fast "constrained diffusion" of chromosome loci over radii of ~500-1000 nm
101 (Marshall et al., 1997; Chubb et al., 2002; Levi et al., 2005), these channels remained
102 DNA-depleted over tens of minutes suggesting that some unknown non-chromatin
103 component(s) might be occupying these channels.

104 Our observations showing an inverse relationship between changes in gene
105 expression and changes in NS proximity across a wide range of NS distances created
106 an apparent paradox when compared to our live-cell imaging observations which
107 instead showed amplification of gene expression of certain genes only after actual
108 microscopic contact with NS. To resolve this paradox, we hypothesized that just as
109 certain genes might need to actually contact NS to enhance their gene expression,
110 other genes might need to contact a different nuclear body/compartment to enhance
111 their gene expression. If these putative additional nuclear bodies/compartments were
112 themselves spatially correlated with NS, then a gene movement leading to actual
113 contact with these nuclear bodies/compartments would appear by SON TSA-seq as a
114 relative movement towards but not close to NS, resolving the apparent paradox.

115 Here we describe identification of several markers for each of two interwoven
116 perispeckle staining patterns. Together, these perispeckle patterns meet our predictions
117 of additional novel compartment(s) surrounding and extending from NS and serving as
118 alternative gene expression hubs for a subset of highly active genes not associated with
119 NS. The differential association of intron-rich versus intron-poor mRNAs with these two

120 perispeckle staining patterns, together with the known roles of many of their marker
121 proteins in RNA processing and/or RNA export, additionally suggests that these
122 perispeckle staining patterns may define nuclear compartments that help spatially
123 integrate the processes of transcription, RNA processing, and nuclear export.
124

RESULTS

Screening for potential markers of alternative "gene expression hubs"

As summarized in the Introduction, we postulated the existence of a nuclear compartment(s), itself spatially correlated with NS, that might act as an alternative hub for the several hundred kbp chromosome gene expression "hot-zones" that were not closely associated with NS (Fig. 1A). We imagined that such a compartment(s) might lie adjacent to and/or extend outwards from NS. Thus, shifts of chromosome regions towards this compartment(s) would then score as an increase in the NS TSA-seq score, which probes the proximity of chromosome regions to NS on an approximately micron-length scale.

We previously applied Tyramide Signal Amplification coupled to mass spectrometry (TSA-MS) to identify NS-enriched proteins (Dopie et al., 2020). Similarly to TSA-seq, TSA-MS exploits the predicted and measured exponential decay of tyramide (phenol)-biotin free radicals as they diffuse outwards from the immunostained target. Given the ~1-micron radius of this spreading (Chen et al., 2018), we realized that tyramide labeling of proteins would extend beyond the NS to proteins in a significant volume surrounding each NS. We therefore ranked proteins by their relative enrichment in NS versus near centromeres, stained by CENPA, to distinguish between proteins specifically enriched near NS versus proteins present throughout the nucleus, including near centromeres; we expected that centromeres would represent a nuclear local environment with low levels of proteins involved in gene expression.

Whereas 74% of the top 91 ranked proteins had been previously reported as colocalizing with NS, the next 92-200 top ranked proteins showed a sharp decrease in

148 previously reported NS colocalization to ~13% (Dopie et al., 2020). Despite this drop in
149 NS colocalization, a large fraction of these proteins, similar to the fraction of known NS-
150 enriched proteins, was connected to various steps in gene expression. Therefore, we
151 reasoned these moderately-ranked proteins were likely enriched in transcriptionally
152 active regions surrounding NS, and thus were candidates for proteins marking our
153 hypothesized gene expression compartment(s) surrounding and extending outwards
154 from NS (yellow regions in Fig. 1A).

155 We identified 25 candidate proteins from this list of moderately-enriched proteins
156 that were reported to show non-diffuse immunostaining within the interchromatin space
157 (ICS), based on the literature and/or the Human Protein Atlas (Pontén et al., 2009). As
158 a first screen, we examined the nuclear distribution of each of these candidate proteins
159 relative to both NS and DNA-staining, looking for candidate proteins that formed distinct
160 staining patterns within and/or surrounding NS and extending out into areas of low
161 DNA-staining corresponding to the ICS (Fig. 1B, left). We visualized their nuclear
162 distribution either using transiently expressed EGFP fusion proteins or through
163 immunostaining when antibodies were available.

164 Among these 25 proteins, essentially all showed some type of nondiffuse pattern,
165 with foci of higher intensity throughout the nucleoplasm (SFig. 1A-B). However, there
166 was a continuum in the extent of the nuclear area occupied outside of NS by higher
167 than background intensities. Proteins such as SRRM2 and RBM25 showed little
168 staining outside of NS, while proteins such as DDX41 and PNN showed staining
169 occupying most of the nucleus (SFig. 1A-C). We focused on proteins which showed
170 intermediate occupancy between these extremes, with patterns of staining extending

171 between NS and throughout the nucleus, even extending all the way to the nuclear
172 periphery (Fig. 1B, SFig. 1A-C).
173 For these proteins in this intermediate nuclear occupancy category (SFig. 1B-C),
174 we observed two "perispeckle" categories of staining. We chose DDX39B and THRAP3
175 as founding members of these two intermediate patterns (SFig. 1C), which both
176 occupied ~40% of the nuclear area outside of NS (SFig. 1B). First, we observed
177 proteins distributions similar to THRAP3 in which the protein was not concentrated
178 within NS but was high in concentration surrounding NS (Fig. 1C, SFig. 1A). Second,
179 we observed protein distributions similar to DDX39B in which the protein was most
180 highly concentrated within NS (Fig. 1D, SFig.1A). These differences were made clearer
181 by comparison of the cumulative protein intensities within versus outside NS (SFig. 1C).
182 Finally, there were proteins that showed non-diffuse staining throughout the nuclear
183 interior, but with little relationship to NS. Examples included SAFB and HNRNPM (SFig.
184 1A, 1C).
185 We decided to ask whether proteins within the same perispeckle categories
186 might colocalize with each other. We did this by comparing protein colocalization with
187 THRAP3 for the first category and DDX39B for the second category (Fig. 1B, right
188 panel). To facilitate this screening, we used CRISPR-mediated knock-ins to
189 fluorescently tag endogenously expressed proteins, constructing U2OS cell lines stably
190 expressing either the combination of EGFP-SON and mCherry-THRAP3 or EGFP-SON
191 and mCherry-DDX39B (see Methods). This avoided the overexpression induced
192 changes in protein distribution sometimes seen after transient transfection (Fig. 1B).
193 We then used immunofluorescence to ask which other candidate proteins overlapped

194 extensively with either DDX39B or THRAP3 (Fig. 1B). Due to the lack of a suitable
195 antibody for MAGOH, we utilized lentivirus-based transduction of a mCherry-MAGOH
196 expression cassette followed by immunostaining of THRAP3/DDX39B.
197 Several additional candidate proteins shared high colocalization for either
198 THRAP3 or with DDX39B, suggesting that they were additional components of these
199 perispeckle patterns. We named the intranuclear protein distribution overlapping with
200 THRAP3 as "Perispeckle THRAP3 Pattern" (PSTP) and the intranuclear protein
201 distribution overlapping with DDX39B as "Perispeckle DDX39B Pattern" (PSDP) (Fig.
202 1C-E). Additional proteins showed their own distinctive nuclear distributions (SFig. 1D);
203 thus, the ICS is likely further subdivided into additional novel
204 networks/condensates/bodies that might partially overlap with PSTP and/or PSDP. For
205 example, PLRG1 was enriched inside NS, similar to PSDP, but outside of NS
206 colocalized with PSTP (SFig. 1D, F).
207 PSTP markers currently include THRAP3 (BCLAF2) and its paralog BCLAF1
208 (Fig. 1 B-C,1E). Additionally, PLRG1 overlaps with PSTP outside of nuclear speckles
209 (SFig. 1E). PSDP markers currently include DDX39B (UAP56), RBM8A (Y14), MAGOH,
210 and POLDIP3 (Fig. 1D,F, SFig. 1D). DDX39B was previously described as enriched in
211 NS but also enriched in the region surrounding NS (Kota et al., 2008). Here we show
212 that DDX39B together with other PSDP components also radiate outwards from NS in
213 thread-like projections that frequently connect neighboring speckles (Fig 1. D,F) while
214 forming a network-like pattern which in some nuclear regions show small foci lining up
215 in linear arrangements (Fig 1D- inset orange box).

Next, we examined how MALAT1 localized relative to these perispeckle patterns, as MALAT1- a long, noncoding RNA (lncRNA)- is spatially related to NS (Fei et al., 2017). Functionally, MALAT-1 associates with certain transcription factors and coactivators (Arun et al., 2020) and has been implicated in the regulation of alternative splicing (Miao et al., 2022). Using an oligolibrary containing 100 probes targeted against MALAT1, we observed both the high NS-enrichment of MALAT1 as well as single RNAs within the ICS. MALAT1 single RNAs away from NS were seen either overlapping or at the edge of both THRAP3 and DDX39B foci (SFig. 1G). Specifically, ~50-60% of MALAT1 RNA signal within the interchromatin space overlapped with both THRAP3 and DDX39B outside NS, using Otsu thresholding (Otsu, 1979) to segment MALAT1, THRAP3, and DDX39B intensities (SFig. 1G).

In summary, we have identified two novel “perispeckle patterns” that subdivide the interchromatin space, as defined by the specific localization patterns of nuclear proteins already reported to be involved in gene expression. Moving forward, we focused the differential localization of THRAP3 (PSTP) versus DDX39B (PSDP) as markers of these two perispeckle staining distributions.

Highly dynamic PSTP and PSDP networks which repeatedly recur within the same or nearby interchromatin space

Projections of higher intensity THRAP3 and DDX39B staining extend outwards from NS forming apparent networks within the interchromatin space.

Fixation can alter the cellular distribution of intrinsically disordered domain-containing proteins (Irgen-Gioro et al., 2022). We therefore used live-cell imaging in

239 U2OS cells to confirm similar PSTP and PSDP distributions in live cells and visualize
240 their dynamics over seconds (Fig. 2A-B) to hours (Fig. 2C-D) using the dual SON and
241 THRAP3 or SON and DDX39B tagged cell lines.

242 Both THRAP3 and DDX39B show non-diffuse high local concentration in linear
243 extensions that appear and disappear every few seconds in the vicinity of speckles (Fig.
244 2A&A', 2B&B', Videos 1&2). Summing these 2D projections over a time of 1 minute
245 reveals a clearer network distribution for both THRAP3 and DDX39B due to repeated
246 recurrence of these projections in the same spatial locations (Fig. 2A-B, white arrows).
247 Thus, while both the PSTP and PSDP are highly dynamic in a timescale of seconds,
248 their extensions averaged over time are quasi-stable over a timescale of minutes.

249 Over a much longer timescale of up to 10 hours, PSTP and PSDP networks
250 preserve their overall nuclear distributions despite their fast dynamics (Fig. 2C-D). NS
251 show occasional movements and fusion and fission events within relatively stable DNA-
252 depleted regions (Videos 3&4). PSTP and PSDP were more dynamic, showing
253 repeated appearance/disappearance of thread-like extensions over several minute
254 intervals within the same DNA-depleted spaces surrounding and between NS (Fig.
255 2C&D Videos 3&4). Because these projections tend to reform in the same or similar
256 regions over time, the overall nuclear distributions of PSTP and PSDP remain relatively
257 stable over longer time periods. In a companion paper, we explore these dynamics in
258 greater detail for both SON and two PSDP members- DDX39B and MAGOH (Kim et al.,
259 2025).

260

261 **PSTP and PSDP subdivide the interchromatin space and respond differently to**
262 **functional and physiological perturbations**

263 THRAP3 and DDX39B, our marker proteins for PSTP and PSDP respectively,
264 were both previously reported as overlapping with and/or surrounding NS (Lee et al.,
265 2010; Kota et al., 2008). Because PSTP and PSDP markers also occupy
266 interchromatin space further away from NS and throughout the nucleus, we next
267 examined their relative spatial distribution outside of NS. Across the range of spatial
268 resolution provided by wide-field deconvolution and STORM super resolution light
269 microscopy, THRAP3 and DDX39B staining “networks” appear largely juxtaposed rather
270 than coincident within the interchromatin space outside of NS (Fig. 3A-B). They are
271 significantly less colocalized relative to each other than the colocalization seen for other
272 components of PSTP with THRAP3 or other components of PSDP with DDX39B
273 (Fig.1E-F, SFig.1F-G).
274 After transcriptional inhibition, many NS components, including SON and a
275 number of splicing factors, are known to concentrate further within NS with a
276 concomitant decrease in their nucleoplasmic concentrations (Spector and Lamond,
277 2011); this is accompanied by NS rounding, enlargement and fusion (Kim et al., 2019).
278 However, the THRAP3 and DDX39B staining networks responded differently
279 after transcriptional inhibition, providing further support for their independent nuclear
280 localization. Between 0-2 hours of transcriptional inhibition by DRB (5,6-dichloro-1-beta-
281 D-ribofuranosylbenzimidazole), the thread-like, diffuse network of THRAP3 staining
282 outside of NS consolidates into fewer but more distinct threads, that then breakup into
283 distinct foci aligned along linear paths, plus larger concentrations adjacent to and
284 surrounding NS (Fig. 3C, Video 5). In contrast, the DDX39B distribution appeared
285 relatively intact, although their stability over time may decrease as reported elsewhere

286 (Kim et al., 2025) (Fig. 3D). DRB inhibits CDK9 and thus transcriptional pause release
287 (Bensaude, 2011; Yankulov et al., 1995). We observed similar disruption but to a lesser
288 extent after inhibiting transcription instead using either Triptolide (SFig 3A, which inhibits
289 the XBP subunit of TFIIH and thus transcriptional initiation (Titov et al., 2011), and α-
290 amanitin (SFig. 3B), which initially inhibits but then degrades RNA Pol II over the ~6 hr
291 treatment time (Nguyen, 1996).
292 To quantify the changes in THRAP3 network upon DRB treatment, we used a
293 function "skeletonize" which uses binary thinning/erosion until a one-pixel wide
294 representation remains. These one-pixel wide chains are called "skeletons" that retain
295 both the shape and connectivity of the original image (SFig. 3C). Using this skeletonize
296 function, we measured two parameters per nucleus: 1) total skeleton length, defined as
297 the sum of all skeletons; 2) the number of connections, where each connection is
298 defined as group of connected pixels >5 pixel length.
299 Based on these parameters, the THRAP3 distribution shows both a reduction in
300 total skeleton length and in the number of connections. In contrast, the DDX39B
301 distribution remains relatively intact (Fig. 3E-F). DRB treatment similarly disrupted PSTP
302 member BCLAF1 distribution which also formed foci which colocalized with THRAP3
303 foci (SFig. 3D-E). However, PSDP member RBM8A remains relatively unchanged
304 (SFig. 3F-G).
305 In summary, we conclude that PSTP and PSDP form spatially and functionally
306 distinct networks that subdivide the interchromatin space.
307
308 **RNA Pol II Ser2p foci localize in close proximity to the PSTP and PSDP networks**

309 We next examined the spatial distribution of RNA Pol II foci relative to PSTP and
310 PSDP (Fig. 4). Antibodies against the Ser5p and Ser2p epitopes of the C-terminal
311 domain (CTD) of the largest RNA Pol II subunit recognize the early initiation versus
312 later elongating forms of RNA Pol II, respectively (reviewed in (Egloff and Murphy,
313 2008)). Immunostaining using these antibodies reveals ~60 nm diameter foci, originally
314 termed "RNA Pol II factories" that map near sites of transcription (Jackson et al., 1993;
315 Iborra et al., 1996; Pombo, 1999). Initially proposed as actual transcription sites (Martin
316 and Pombo, 2003; Xie et al., 2006), the functional significance of these transcription
317 factories remains unclear.
318 Although an increased density of RNA Pol II Ser5p and Ser2p foci have
319 previously been described as surrounding the NS periphery, large numbers of RNA Pol
320 II Ser2p and Ser5p foci away from NS are distributed throughout the nuclear interior in
321 no obvious pattern (Chen et al., 2018) (Fig. 4A&D). Immunostaining, however, now
322 reveals a striking spatial correlation of these RNA Pol II foci localized away from NS
323 with the THRAP3 and DDX39B networks (Fig. 4B-C and 4E-F).
324 We used an intensity threshold of 40% of local intensity maxima to segment foci
325 of both THRAP3 and DDX39B (SFig. 4). Median distances of both Ser5p and Ser2p
326 RNA Pol II foci are ~0.2 μm to the nearest edges of THRAP3 foci (Fig. 4K, magenta and
327 purple). Ser5p RNA Pol II foci are similarly close to DDX39B foci (Fig. 4K, light green),
328 while Ser2p RNA Pol II foci show a somewhat increased distance distribution but
329 remain mostly within ~0.5 μm to DDX39B foci (Fig. 4K, dark green).
330 Thus, RNA Pol II foci, used as proxies for mapping sites of active transcription,
331 nearly all map within a few hundred nm of THRAP3 or DDX39B foci, supporting the idea

332 of PSTP and PSDP acting as additional nuclear niches closely associated with
333 transcriptionally active chromosome loci.
334
335 **Gene expression hot zones interact preferentially with PSTP and PSDP as**
336 **measured by TSA-seq**
337 To follow up our demonstration of the close association of RNA pol II foci with
338 perispeckle patterns, we next asked if, as hypothesized (Fig. 1A), Type II SON TSA-seq
339 peaks would show a close association with one or both perispeckle patterns similar to
340 how Type I SON TSA-seq peaks show a close association with NS. More specifically,
341 we used TSA-seq to compare the association of Type II SON TSA-seq peaks with the
342 PSTP and/or the PSDP versus NS.
343 We combined the “super-saturation” TSA-seq 2.0 protocol (Zhang et al., 2021)
344 with the use of dithiothreitol (DTT) to improve the TSA-seq spatial resolution, as
345 described in the original TSA-seq 1.0 protocol (Chen et al., 2018). DTT improves spatial
346 resolution by decreasing the lifetime, and therefore the diffusion radius of the tyramide
347 free-radical, while the "super-saturation" protocol greatly reduces the number of cells
348 required for TSA-seq 2.0. To compensate for the reduced labelling due to quenching by
349 DTT, we increased the tyramide-biotin concentration by 10-fold.
350 Both in HCT116 (Fig. 5A-B) and U2OS cells (SFig. 5A-B), DDX39B and THRAP3
351 TSA-seq peak and valley patterns qualitatively roughly parallel the SON TSA-seq peak
352 and valley pattern. Quantitatively, however, there are informative differences. We
353 interpret DDX39B and THRAP3 TSA-seq peaks as corresponding to genomic regions
354 that associate closest to foci of DDX39B and THRAP3 staining. The highest amplitude

355 DDX39B and THRAP3 peaks do align with the largest, Type I SON TSA-seq peaks
356 (yellow highlights, Fig. 5A, SFig. 5A). However, we interpret the disproportionally higher
357 amplitude of DDX39B and THRAP3 relative to smaller SON TSA-seq peaks as
358 evidence for the association of these genomic regions near foci of DDX39B and
359 THRAP3 when they are not located near NS. For example, DDX39B and THRAP3
360 TSA-seq peak amplitudes are nearly the same over Type I SON TSA-seq peaks that
361 vary two-fold in SON TSA-seq amplitudes (yellow highlights, Fig. 5A, SFig. 5A). As
362 hypothesized, Type II SON TSA-seq peaks with near-zero SON TSA-seq amplitudes
363 show disproportionally larger DDX39B and, especially, THRAP3 TSA-seq peak
364 amplitudes (blue highlights, Fig. 5A, SFig. 5A) that in some cases approach similar
365 THRAP3 peak amplitudes as observed over Type I peaks (yellow highlights, Fig. 5A,
366 SFig 5A). This disproportionate scaling extends more generally over larger regions of
367 the genome as appreciated in scatterplots of DDX39B or THRAP3 versus SON TSA-
368 seq which show a lower slope for higher versus lower values of SON TSA-seq (Fig. 5B).
369 Finally, DDX39B and THRAP3 peaks are significantly broader and more rounded
370 than their corresponding SON TSA-seq peaks, and they extend over most of the iLADs
371 in which they are embedded, in contrast to the narrower SON TSA-seq peaks. This
372 trend is somewhat more pronounced in the THRAP3 versus DDX39B TSA-seq.
373 We interpret this broader shape of DDX39B and THRAP3 TSA-seq peaks relative to
374 SON TSA-seq peaks as due to the extent to which DDX39B and THRAP3 networks
375 extend throughout the nuclear interior such that iLAD regions are never that distant from
376 the nearest DDX39B or THRAP3 foci. The even broader shape of the THRAP3 versus
377 DDX39B TSA-seq peaks would then be consistent with the greater extent to which the

378 THRAP3 network spreads throughout the nuclear interior relative to the DDX39B
379 network.
380
381 **FISH validation of close association of gene expression hot-zones with PSTP and**
382 **PSDP**
383 To test these TSA-seq interpretations, we first selected 7 large SON TSA-seq
384 Type I peaks and 8 Type II SON TSA-seq local maxima (small peaks or "peak-within-
385 valleys") for immuno-FISH validation in both HCT116 (Fig. 5C) and U2OS (SFig. 5C)
386 cells. We used pooled oligonucleotide probes that targeted simultaneously either all 7
387 Type I peaks or all 8 Type II SON TSA-seq peaks (STable 1). To determine distances
388 to the nearest NS, defined by SON staining, or to the nearest DDX39B or THRAP3 foci,
389 we used a local segmentation of the immunostaining based on an intensity threshold
390 corresponding to 50% of the peak intensity of the nearest staining focus (see Methods).
391 As expected, the aggregated Type I SON TSA-seq peaks localized near NS (Fig.
392 5C-D, SFig. 5C-D), with median distances of 0.20 (HCT116) and <0.20 (U2OS) μm from
393 NS. The aggregated Type II peaks instead localized at varying distances from NS, with
394 median distances of 0.74 (HCT116) and 0.54 (U2OS) μm. In contrast, in both HCT116
395 and U2OS cells Type I and II SON TSA-seq peaks positioned close to THRAP3 or
396 DDX39B foci, with median distances of ≤ 0.25 μm, including alleles that are positioned
397 away from NS (Fig. 5B-G, SFig. 5C-G).
398 We next used DNA FISH in U2OS cells to paint chromosome "trajectories" from
399 the nearest LAD/iLAD boundary to either the apex of a SON TSA-seq Type I peak or to
400 the apex of a SON TSA-seq Type II peak (Fig. 6). In both cases, we used

401 oligonucleotide libraries designed to target 7-9 ~100 kb regions spaced approximately
402 evenly along these trajectories.

403 In most cells (~70-90%), both chromosome trajectories showed multiple,
404 individual DNA FISH spots corresponding to the iLAD regions flanking the TSA-seq
405 peak locations, consistent with a partly to more fully extended iLAD chromosome
406 trajectory (Fig. 6). In some cells (~10-30%), however, these FISH spots merged into a
407 single, compact signal, larger than the wide-field diffraction limit, suggesting a more
408 localized folding of the iLAD trajectory (Fig. 6). Interestingly, a high fraction of the
409 extended trajectories aligned relative to the THRAP3 (40-51%) and, especially, the
410 DDX39B staining foci (55-73%) (Fig. 6).

411 The arms of both extended and compact trajectories appeared nearly always
412 (~70-90%) as close or further from the nearest SON, THRAP3, or DDX39B foci than the
413 DNA FISH spot corresponding to the apex of the TSA-seq peak location ("Apex") (Fig.
414 6).

415 To compare quantitatively the association of different trajectory regions with the
416 perispeckle patterns and NS, we segmented and divided the DNA-FISH arm signal into
417 three parts based on their proximity to the Apex: 1) "Arm-close" region (pixels with
418 distances $\leq 25^{th}$ percentile closest to Apex); 2) "Arm-center" region (pixels with distances
419 within the 26th-75th percentile from Apex); and 3) "Arm-far" region (pixels with distances
420 $>75^{th}$ percentile from Apex). Then for the Apex and each of these three arm regions, we
421 calculated the shortest Euclidian distance of the center of mass to the nearest
422 segmented NS or protein foci edge. (Note that the nearest NS or protein foci edge could
423 be different for the Apex and each of these three regions; see Methods.)

424 For the Type I trajectory, the Apex was closer to SON, THRAP3 or DDX39B foci
425 compared to Arm regions (Fig. 6A, left lower panel). Moreover, the "Arm-close", "Arm-
426 center", and "Arm-far" regions showed a progressive increase in distances relative to
427 the nearest NS or protein foci edge, respectively. As predicted from the rounded shape
428 of the DDX39B and THRAP3 TSA-seq Type II peaks, the entire Type II iLAD
429 chromosome trajectory typically lies within several hundred nm of some part of the
430 DDX39B and THRAP3 network (Fig. 6B). Distances of the Apex of the Type II peak
431 from the nearest NS edge as expected were larger than for the Type I peak (~0.4
432 versus <0.2 μm). The Type II Apex compared to the Arm-far region was significantly
433 closer to the THRAP3 foci (Fig. 6B, lower left panel). However, the distances to the
434 edge of the nearest DDX39B foci were similar for the Apex and all three arm regions
435 (Fig. 6B, lower left panel), which might reflect the apparent higher alignment of the Type
436 II overall trajectory with the DDX39B network noted previously.
437 In summary, these results confirm that the chromosome gene expression hot-
438 zones corresponding to SON TSA-seq local maxima associate close to DDX39B and
439 THRAP3 foci, even when they are positioned at a distance from NS.
440
441 **Interactions of specific RNAs with PSTP and PSDP**
442 NS were first proposed to act as gene expression hubs not only because a
443 subset of active genes closely associated with the NS periphery but also because a
444 subset of the RNAs transcribed from these genes, for example from the *COL1A1* and
445 *actin* genes, specifically entered and concentrated within the adjacent NS (Hall et al.,
446 2006). We later described how HSPA1A RNA also entered and concentrated within NS

447 (Hu et al., 2009). As reviewed elsewhere, the trafficking of a large number of specific
448 RNAs through NS has now been suggested using genome-wide sequencing-based
449 methods (Wu et al., 2024; Barutcu et al., 2022; Khyzha et al., 2025). Most NS-enriched
450 factors are involved in some aspect of RNA processing and/or export, and the idea of
451 NS acting as a gene expression hub has always included the concept that proximity of
452 genes and RNAs to NS might increase overall gene expression levels largely through
453 their acceleration of post-transcriptional RNA processing and export events (Smith et
454 al., 2020; Bhat et al., 2024; Barutcu et al., 2022; Wu et al., 2024; Wang et al., 2018).
455 The marker proteins for PSTP and PSDP that we identified here have similarly
456 been functionally tied to various aspects of RNA processing, stability, and export.
457 Therefore, using two experimental systems we decided to explore whether PSTP and/or
458 PSDP networks might not only be associated with specific chromosome regions but
459 also with specific pre-mRNAs and mRNAs, similarly to NS. Because Type I versus Type
460 II chromosome regions are enriched in genes with low versus high intron-content,
461 respectively (Gholamalamdari et al., 2025), we specifically compared the localization of
462 RNAs from intronless versus intron-containing genes.
463 First, we used two cell lines, described elsewhere (Mor et al., 2010; Brody et al.,
464 2011), carrying different stably integrated, multi-copy transgene arrays. Because these
465 transgene arrays express at high levels, they produce large numbers of RNPs whose
466 locations can be mapped relative to NS and perispeckle patterns with high statistical
467 power within individual nuclei. The “E6” cell line contains a synthetic transgene with β-
468 globin derived sequences including 6 exons and 5 introns, whereas the “Mini-
469 dystrophin” cell line ("mini-Dys") contains a truncated dystrophin transgene with a single

470 exon and no introns. Both transgene RNAs contain 24 MS2 repeats and both cell lines
471 express the MS2 coat protein (MCP) tagged with YFP that binds to this MS2 RNA
472 repeat. Because of the hundreds of transcripts per nucleus, we used an automated
473 image processing pipeline that segments the SON, DDX39B or THRAP3 intensities,
474 using Otsu global thresholding, and then computes the distance of the center of each
475 detected RNP to the nearest segmented staining feature (see Methods).
476 As our second experimental system, we used HSPA1 and HSPH1 endogenous
477 genes, thereby allowing us to complement our results using the transgene arrays.
478 Unlike most endogenous genes, HSPA1 and HSPH1 genes produce a high number of
479 transcripts. We chose times after heat shock (HS) producing high numbers of HSPA1
480 and HSPH1 transcripts per nucleus, allowing us to avoid the use of transgenes while
481 still acquiring measurements for ~10-20 RNPs per nucleus away from the site of
482 transcription. Whereas the highly homologous *HSPA1A* and *HSPA1B* genes expressed
483 from the HSPA1 locus (situated within a SON Type I peak) produce short transcripts
484 less than 1kb with no introns, the 27 kb *HSPH1* gene (resident within a SON Type II
485 peak) contains 17 introns. The smaller number of transcripts per nucleus of these heat
486 shock genes allowed us to use a semi-automated local intensity thresholding and
487 measure distance of each RNP to the nearest staining foci by an automated algorithm
488 (see Methods). This local thresholding allows detection of lower intensity staining foci
489 which are missed by global thresholding approaches. The short length of HSPA1 genes
490 results in significantly faster induction after HS as compared to the much longer HSPH1
491 gene. We chose different times after HS- 30 mins for HSPA1 and 60 mins for HSPH1,

492 which maximized the number of nuclear RNPs present in the nucleus away from their
493 transcription site for each gene.
494 In both experimental systems, the intron-rich E6 and HSPH1 RNAs localized very
495 close to THRAP3 foci in absolute distances (0.12 and 0.03 μm mean and median (E6);
496 0.13 and 0.07 μm mean and median (HSPH1)) and closer than the localization to
497 THRAP3 foci of the intronless mini-dystrophin and HSPA1 RNAs (0.30 and 0.23 μm
498 mean and median (mini-dystrophin); 0.34 and 0.30 μm mean and median (HSPA1))
499 (Fig. 7A-B,E&G, I-J). However, both intron-rich and intronless transcripts showed very
500 close and similar distances to the nearest DDX39B foci (0.10 and 0.04 μm mean and
501 median (E6); 0.17 and 0.06 μm mean and median (HSPH1); 0.11 and 0.05 μm mean
502 and median (mini-dystrophin); 0.15 and 0.06 μm mean and median (HSPA1)) (Fig. 7C-
503 D, F&H, I-J). These distances to the nearest DDX39B and THRAP3 foci for all these
504 transcripts are significantly lower than their distances to NS (SON and SRRM2); this
505 indicates that a significant fraction of the transcripts associate with DDX39B and
506 THRAP3 foci away from NS.
507 Overall, these results from both transgene arrays and endogenous genes
508 indicate that the transcripts from intron-containing genes preferentially associate with
509 PSTP within the interchromatin space while transcripts from both intron-containing and
510 intronless genes show close association with PSDP.
511
512 **THRAP3 and DDX39B networks are largely maintained after NS knockdown**
513 We next asked whether the maintenance of PSTP and PSDP networks depends
514 on NS. One possibility is that NS nucleate these PSTP and PSDP networks and

515 therefore these perispeckle networks would require NS for maintenance. Alternatively,
516 these perispeckle networks might be maintained independently of NS, possibly even
517 with NS then preferentially nucleating within regions of high local PSDP protein
518 concentrations.

519 Previous work had concluded that SON and SRRM2 are core NS proteins and
520 essential for NS formation (Ilik et al., 2020). We used simultaneous degradation of both
521 SON and SRRM2 using an improved auxin-inducible degron (AID2) system (Fig. 8A,
522 SFig. 8A) (Yesbolatova et al., 2020). Both endogenous alleles of SON and SRRM2 in
523 HCT116 cells were modified with degron tags and mClover and mCherry fluorescent
524 tags, respectively. Fixed and live-cell microscopy both show NS, identified by SON and
525 SRRM2 concentrations, shrinking and then in most cases disappearing within 0-4 hours
526 of analog 5-Ph-IAA treatment (Fig. 8B-C, SFig. 8B). Live-cell imaging reveals NS initially
527 shrinking, while maintaining elevated concentrations of SON during this shrinkage (Fig.
528 8B, 20-40 mins), consistent with SON existing as a condensate within NS.

529 Immunostaining of DDX39B and THRAP3 shows similar staining networks both
530 before and after NS depletion (Fig. 8C). We used transfection to express a HaloTag-
531 DDX39B construct and performed live-cell imaging after two weeks of drug selection.
532 The cells were imaged 20-25 minutes after adding 5-Ph-IAA-containing media. These
533 live-cell movies reveal a ~20% reduction of DDX39B intensity within the regions
534 formerly occupied by NS after SON and SRRM2 double knockdown (DKD); a
535 concomitant increase in DDX39B intensities is seen in the network staining outside of
536 the regions formerly occupied by NS (Fig. 8B).

537 At later time points (>45 mins), NS SON levels drop to just a few percent of their
538 value at 20 mins (Fig. 8B), while DDX39B levels within the same NS decrease by only
539 ~25%. Importantly, the overall nuclear DDX39B intranuclear distribution is largely
540 maintained, including the DDX39B concentrations over regions previously occupied by
541 SON in NS.

542 The previous conclusion that SON and SRRM2 are required for NS nucleation
543 and maintenance was based on the dispersion of several other NS markers throughout
544 the nucleus after simultaneous SON and SRRM2 DKD using siRNA (Ilik et al., 2020;
545 Zhang et al., 2024). An alternative explanation, however, could be that SON and
546 SRRM2 are required only for recruitment of this subset of NS components but not for
547 NS nucleation and maintenance per se. Our observation of an initial shrinking of the NS
548 after SON and SRRM DKD using AID2 (Fig. 8A, B), simultaneous with retention of
549 elevated SON and SRRM2 concentrations within these shrinking NS, is consistent with
550 the shrinkage and then disappearance of an actual condensate dependent on SON and
551 SRRM2, thus supporting a primary role of SON and SRRM2 in nucleating and
552 maintaining NS.

553 NS have been operationally defined as the light microscopy equivalent of the
554 Interchromatin Granule Clusters (IGCs) first identified by electron microscopy; these
555 granules were demonstrated by immunostaining to contain RNA (reviewed in (Chen and
556 Belmont, 2019)). At the light microscopy level, NS were also operationally defined by
557 their local concentration of polyadenylated RNAs (Carter et al., 1991, 1993).

558 We therefore next examined the distribution of polyA-RNA after SON and
559 SRRM2 acute DKD using RNA FISH. Indeed, we observed the dispersion of locally
560 concentrated polyA-RNA "islands" after SON and SRRM2 DKD (Fig. 8D).
561 We therefore conclude first that NS are indeed depleted after SON and SRRM2
562 DKD and second that the DDX39B and THRAP3 perispeckle networks are largely
563 maintained after NS depletion.
564
565 **Nuclear genome positioning relative to PSTP and PSDP is largely maintained**
566 **independent of NS**
567 Given the general alignment of THRAP3 and DDX39B with SON TSA-seq
568 signals, plus the maintenance of PSTP and PSDP after NS elimination, we next asked
569 whether chromosome positioning relative to PSTP and/or PSDP was dependent on
570 maintenance of NS. We performed DDX39B and THRAP3 TSA-seq after 4 hours of 5-
571 Ph-IAA induced SON and SRRM2 DKD, the earliest time point we had sampled
572 showing maximum KD of both SON and SRRM2 expression (Fig. 8A). We observed
573 little change in chromosome positioning relative to PSTP and PSDP after this several
574 hour loss of SON and SRRM2 and NS, including over gene expression hot-zone
575 chromosome regions corresponding to both Type I and II SON TSA-seq peaks (Fig. 8E,
576 SFig. 8B-E).
577 Overall, both the THRAP3 and DDX39B TSA-seq reveal little change after NS
578 elimination. Quantitative comparisons show a slight, largely statistically insignificant
579 increase in DDX39B TSA-seq values after NS elimination (SFig. 8B). Conversely,
580 THRAP3 TSA-seq shows a small overall decrease in signal after NS elimination, which

581 does score as statistically significant (SFig. 8C); this small change in THRAP3 TSA-seq
582 scores appears to reflect a systematic variation in scaling across the genome after SON
583 and SRRM2 DKD. Specifically, THRAP3 TSA-seq peaks are decreased in amplitude
584 slightly while valleys are deepened slightly. The reasons for these subtle genome-wide
585 changes in DDX39B and THRAP3 TSA-seq score amplitudes remain unclear but may
586 be related to small shifts in DDX39B and THRAP3 intranuclear distribution after NS KD.
587 Despite these small changes in scaling of the DDX39B and THRAP3 TSA-seq
588 signals, we do not see any significant or specific changes in the overall patterns of
589 peaks corresponding to NS and perispeckle pattern associated domains (Fig.8E,
590 SFig.8B-E).
591 Finally, we asked how genes differentially positioned relative to NS might change
592 their expression as a function of SON and SRRM2 DKD. SON depletion is known to
593 arrest cell growth through perturbation of the cell cycle, particularly during mitosis
594 (Sharma et al., 2010; Ahn et al., 2011). To minimize changes in gene expression due to
595 changes in cell cycle progression, we combined an extended 16 hr DKD of SON and
596 SRRM2 with a cell-cycle arrest in late G1/early S-phase. We applied the DKD in cells
597 as they progressed from G1-arrest into a late G1/early S phase block (see Methods).
598 RNA-seq analysis revealed that NS-proximal genes within +/- 500 kb of Type I
599 SON TSA-seq peaks showed a systematic bias towards decreased gene expression
600 after SON and SRRM2 DKD (Fig. 8F-H). In contrast, genes within +/- 500 kb of Type II
601 SON TSA-seq peaks, showed no strong bias towards decreased versus increased
602 differential gene expression after SON and SRRM2 DKD. We note that the SON TSA-
603 seq peak-calling used Hi-C subcompartment identity to classify Type I versus Type II

peaks, which caused some degree of misclassification of SON TSA-seq positive peaks (Type I) versus "peak-within-valley" SON TSA-seq local maxima (Type II). Instead, defining Type II peaks as those with SON TSA-seq scores ≤ 0.0 (Fig. 8G, dashed line), we observe a more pronounced ~2-fold bias of increased (123 genes) versus decreased (62 genes) differentially expressed genes within Type II peaks after NS KD (Fig. 8G, left of dashed vertical line).

Thus, we conclude that chromosome positioning relative to PSTP and PSDP networks, including regions originally near NS defined by SON TSA-seq peaks, remain unchanged for at least several hours after NS elimination. This observation raises the possibility that the perispeckle patterns might maintain genome organization independent of the NS defined by SON and SRRM2. Despite this maintenance of genome organization of Type I and II gene expression hot-zones, genes in Type I hot-zones do appear dependent on NS to sustain their normal levels of gene expression.

619 **Discussion**

620 **Summary**

621 We set out to resolve an apparent paradox. On the one hand, live-cell imaging
622 (Kim et al., 2020) and RNA FISH (Zhang et al., 2021; Alexander et al., 2021) both
623 suggested actual contact with NS was required for gene expression amplification. On
624 the other hand, a strong correlation was observed genome-wide between changes in
625 gene expression and positioning of these genes relative to nuclear speckles, even when
626 these changes in positioning did not involve changes in actual nuclear speckle close
627 association (Zhang et al., 2021; Gholamalamdari et al., 2025). To reconcile these two
628 distinct observations, we hypothesized the existence of a previously unidentified gene
629 expression hub(s) that was itself spatially correlated with but distinct from NS.

630 Here we describe the identification of two perispeckle patterns, characterized by
631 the concentrations of specific proteins, which are both tightly spatially correlated with
632 NS (Fig. 9). PSTP components surround NS, defined by SON and SRRM2
633 immunostaining, and in some cases may colocalize but not concentrate within NS, while
634 PSDP components concentrate within NS. More importantly, both extend outwards and
635 throughout the nuclear, DNA-depleted interior in thread-like patterns from NS. Together
636 PSTP and PSDP subdivide the ICS. Meanwhile, other proteins that concentrate within
637 the ICS overlap with neither PSTP nor PSDP, suggesting that these two perispeckle
638 patterns together still occupy only a fraction of the total ICS; this would leave substantial
639 additional space which other condensates might occupy.

640 PSTP and PSDP appear to represent an alternate gene expression hub in the
641 sense that a large fraction of the chromosomal regions with high gene expression levels

642 not localized near NS are instead localized very close to the thread-like patterns of
643 PSTP and PSDP. Similarly to nuclear speckles, PSTP and PSDP contain a mixture of
644 components involved in various steps of gene expression, especially RNA splicing and
645 export. Additionally, we show the preferential association of RNAs from two model
646 intron-containing genes with PSTP as compared to the RNAs from two model intron-
647 less genes. In contrast, the RNAs from both intron-containing and intronless genes are
648 closely associated with PSDP. Thus, we speculate that the PSTP and PSDP
649 perispeckle networks may additionally facilitate a spatial coupling between the
650 machinery of transcription and RNA processing and export for a subset of active genes
651 and their transcripts (Fig. 9).
652
653 **Possible resolution of our paradox**
654 We propose that the close association of highly active chromosomal regions not
655 near NS with these perispeckle patterns may resolve the apparent paradox between our
656 previous live-cell imaging and genomic analysis of the relationship of active genes
657 relative to NS. Because of the close spatial arrangement of PSTP and PSDP relative to
658 NS, repositioning of chromosomal regions with gene activation to bring them into
659 contact with these perispeckle patterns (Fig. 9, right panel) will also bring these active
660 chromosomal regions closer to NS on average over the cell population. Most RNA Pol II
661 Ser2p and Ser5p foci localize within several hundred nm of PSDP and, especially,
662 PSTP foci, even those positioned away from NS. Similarly, chromosomal gene
663 expression hot-zones, identified as Type I and Type II SON TSA-seq peaks, localize
664 within several hundred nm of PSTP and PSDP foci. This is true even when positioned

665 away from NS, as is the case for the majority of alleles of Type II SON TSA-seq peak
666 regions. Moreover, as predicted in our original model (Fig. 1A), we showed that a
667 chromosome gene expression hot-zone corresponding to a Type II SON TSA-seq was
668 the closest chromosome region to a PSTP or PSDP foci over the entire chromosome
669 iLAD trajectory stretching from the nearest LAD to this Type II SON TSA-seq peak.
670

671 **Perispeckle patterns are dynamic networks rather than stable nuclear bodies**

672 In our original hypothesis, we had envisioned Type II SON TSA-seq peaks as
673 interacting with an alternative nuclear body/compartment of comparable stability to NS.
674 Instead, we observe both PSTP and PSDP networks away from NS to be highly
675 dynamic over a time period of seconds to tens of seconds, even though we see their
676 repeated recurrence in similar spatial patterns on a time scale of minutes such that
677 time-averaging reveals a more definite network pattern. In a companion paper, we
678 more thoroughly examine dynamics of PSDP components DDX39B and MAGOH and
679 show that their preferential concentration into stable time-averaged patterns disappears
680 with ATP-depletion and at least partially with transcriptional inhibition (Kim et al., 2025).
681 We also show directional, bulk transfer of SON condensates between NS within PSDB
682 network connections (Kim et al., 2025).
683

684 **Relationship of DDX39B perispeckle pattern to NS**

685 Despite the close spatial relationship of PSTP and PSDP to NS, both THRAP3
686 and DDX39B distributions are largely maintained after NS disruption. SON and SRRM2
687 were considered to be required for NS integrity because their double KD (DKD) led to

688 dispersal of several other known NS proteins (Ilik et al., 2020). DDX39B, and possibly
689 other PSDP components, retain the same high concentrations within bodies that
690 originally colocalized with NS even after SON and SRRM2 KD that is reported to
691 eliminate NS (Ilik et al., 2020). Should these high-concentration DDX39B bodies then
692 be considered as NS that persist after SON and SRRM2 DKD with SON and SRRM2
693 necessary only for retention of a subset of NS proteins?

694 NS were described originally as clusters of RNPs and foci of polyA accumulation.
695 From this functional view of NS as concentrators of RNPs, we therefore suggest that the
696 observed loss of NS- associated poly-A RNA accumulations after SON and SRRM2
697 DKD means NS are indeed eliminated after SON and SRRM2 KD. Just as nucleolar
698 GC proteins such as nucleolin can mix with the FC (Lafontaine et al., 2021), we suggest
699 PSDP components have the ability to mix with NS components. Similar to how the
700 dense fibrillar component and fibrillar centers (FC) form within the granular
701 compartment (GC) of nucleoli, we suggest that NS form within accumulations of PSDP
702 components

703 A second question is whether gene positioning is controlled not by NS per se but
704 by PSDP, given that gene positioning is largely maintained for at least several hours
705 after NS disruption, and what functions NS may impart separate from PSDP. The
706 observation of gene expression amplification with NS contact (Kim et al., 2020;
707 Alexander et al., 2021; Chaturvedi and Belmont, 2024), plus the observed reduced
708 expression specifically of a subset of genes positioned very close to NS after SON and
709 SRRM2 KD, suggests that NS are indeed required for the increased expression of a
710 subset of NS proximal genes.

711 **Connections of perispeckle patterns to RNA processing and trafficking**

712 Similar to NS, which are enriched especially for proteins related to multiple levels
713 of RNA processing, modification, and export, the perispeckle pattern marker proteins we
714 identified here are all related to RNA splicing and export. Our demonstration of close
715 association of RNA with these two perispeckle patterns raises the interesting possibility
716 that these perispeckle patterns might be pathways for mRNAs moving away from the
717 gene and trafficking through the nucleus.

718 Among the PSTP marker proteins, THRAP3 (TRAP150) was described as a
719 member of the TRAP/Mediator complex (Ito et al., 1999) but also associates with mRNA
720 export factor TAP (Lee et al., 2010) and has been shown to play roles in pre-mRNA
721 splicing (Lee et al., 2010; Lee and Tarn, 2014; Vohhodina et al., 2017), mRNA
722 degradation (Lee et al., 2010), and R-loop resolution (Kang et al., 2021). BCLAF1 has
723 known roles in pre-mRNA splicing (Vohhodina et al., 2017), nuclear retention of RNAs
724 (Varia et al., 2013) and as a transcriptional repressor (Shang et al., 2022) . PLRG1 is a
725 component of the cell division cycle 4-like (CDC5L) complex which is part of the
726 spliceosome (Ajuh, 2000) and is involved with alternative splice-site selection (Llères et
727 al., 2010), as well as DNA repair (Zhang et al., 2005) and the ATR-response (Zhang et
728 al., 2009). During development, PLRG1 regulates proliferation and apoptosis
729 (Kleinridders et al., 2009). Interestingly, we observed the mRNAs from intron-rich
730 genes, but not intronless genes, associating closely with PSTP.

731 Among the PSDP marker proteins, DDX39B is a DEAD-box RNA helicase
732 already known to regulate release of spliced mRNAs from NS (Hondele et al., 2019;
733 Taniguchi and Ohno, 2008; Luo et al., 2001; Fan et al., 2018). DDX39B is also

734 essential for R-loop resolution (Pérez-Calero et al., 2020) and is a member of the TREX
735 export complex (Dias et al., 2010; Wang et al., 2018; Shen et al., 2008). RBM8A (Y14)
736 and MAGOH are both members of the core Exon Junction Complex (EJC) that
737 assembles on pre-mRNAs over the junction of two exons that are spliced together (Le
738 Hir, et al. 2000) and provides binding platform for additional factors involved in mRNA
739 export and nonsense-mediated decay (NMD) (Le Hir, Hervé, et al. 2001).
740 Interestingly, DDX39B previously was suggested to regulate the entry and
741 release of RNAs from phase-separated condensates in an ATP-dependent manner
742 (Hondele et al., 2019). Immunogold EM against DDX39B coupled to EDTA-regressive
743 staining showed DDX39B associating at the periphery of IGCs and thread-like, likely
744 RNA-containing projections extending from IGCs into the interchromatin space (Kota et
745 al., 2008). DDX39B is evolutionarily-conserved and is essential for the export of spliced
746 RNA and intronless RNA (Jensen et al., 2001; Gatfield et al., 2001; Kota et al., 2008;
747 Dias et al., 2010; Wang et al., 2018). Higher-order assembly of export-competent
748 mRNPs is also mediated by DDX39B (Xie et al., 2023). Cosistent with a role of DDX39B
749 in nuclear RNA export, we observed mRNAs from both intron-rich and intron-less genes
750 associating closely with PSDP.
751 All together, these observations raise the hypothesis of RNPs being moved
752 sequentially through different spatially organized “processing” condensates before and
753 during export out of the nucleus.
754
755 **Future Directions**

Our description of perispeckle patterns suggest multiple avenues for future investigation. Of central interest will be going beyond correlation to test causality between chromosomal and RNA association with PSTP and PSDP networks with modulation of gene expression, including RNA export. Future live-cell imaging will be valuable to test the temporal correlation between contact with PSTP and/or PSDP and changes in gene expression and/or RNA movements as well as monitoring changes in gene expression after acute knockdown of PSTP and PSDP components. Beyond gene expression, we anticipate future investigations into the possible role of perispeckle patterns in DNA repair and genome stability given that multiple PSTP and PSDP components have been implicated in both R-loop resolution (THRAP3, DDX39B, POLDIP3) (Kang et al., 2021; Pérez-Calero et al., 2020; Björkman et al., 2020) and DNA repair and genome stability (THRAP3, BCLAF1, RBM8A, DDX39B, PLRG1) (Vohhodina et al., 2017; Yu et al., 2023a; Chuang et al., 2019; Xu et al., 2020; Choi et al., 2023).

Two additional functions of perispeckle patterns are suggested by our work and others. First, a role of PSDP in bulk trafficking of NS components is suggested by a companion study. Using live-cell imaging, we demonstrated the directional bulk transfer of SON protein as small condensates between NS in ATP-dependent "connections" marked by dynamic DDX39B, MAGOH, and SON multi-phase protein concentrations whose interactions form a more stable unit that any of the individual components (Kim et al., 2025). Second, perispeckle patterns may play a role in genome stability, as multiple components of both PSTP and PSDP have been implicated in both R-loop resolution (THRAP3, DDX39B, POLDIP3) (Kang et al., 2021; Pérez-Calero et al., 2020;

779 Björkman et al., 2020) and DNA repair and genome stability (THRAP3, BCLAF1,
780 RBM8A, DDX39B, PLRG1) (Vohhodina et al., 2017; Yu et al., 2023a; Chuang et al.,
781 2019; Xu et al., 2020; Choi et al., 2023).
782 Finally, although we focused here on PSTP and PSDP, our initial screening
783 suggested that there will be additional perispeckle patterns/ protein condensates that
784 further subdivide the interchromatin space. We therefore suggest additional
785 investigations will be needed to fully appreciate the integration of these dynamic protein
786 condensates with each other and with important nuclear functions.
787
788

789 **Methods:**

790 **Cell lines and cell culture**

791 U2OS and HCT116 cells were obtained through the ATCC, expanded through
792 pyramid stocking, and maintained as per the 4D Nucleome SOP
793 (https://data.4dnucleome.org/resources/experimental-resources/cell-lines). U2OS cell
794 lines containing E6 β-globin and mini-Dystrophin A1 transgenes were described
795 previously (Mor et al., 2010; Brody et al., 2011).

796 All cells were grown at 37°C in a humidified incubator with 5% CO_2. Specifically,
797 both U2OS and HCT116 cells were cultured in McCoy's 5A medium (UIUC cell media
798 facility) supplemented with 10% fetal bovine serum (FBS) (VWR, cat# 97068-091, Lot
799 #035B15). Cells were passaged (or harvested) at 70%-80% confluency using Trypsin-
800 EDTA (0.05%) (Thermo Fisher Scientific, cat# 25300062).

801 U2OS cell lines with the E6 β-globin and mini-Dystrophin transgenes were
802 cultured in low glucose containing DMEM (UIUC cell media facility). The E6 β-globin cell
803 line was maintained with 10 μg/ml Puromycin (Puromycin Dihydrochloride, Gibco, cat#
804 A1113803) and 0.54 mg/ml Zeocin (Gibco, cat# R25001). The mini-dystrophin A1 cell
805 line was cultured with 50 μg/ml Hygromycin (Gibco, cat#10687010) and 0.54 mg/ml
806 Zeocin (Gibco, cat# R25001). Cells were passaged using Trypsin-EDTA (0.05%)
807 (Thermo Fisher Scientific, cat# 25300062).

808 For all cell lines, cells were cultured for a maximum of 10-12 passages after
809 thawing.

810

811 **cDNA Constructs and screening**

812 For the screening of selected protein candidates, PCR amplicons were prepared
813 from cDNA. For genes with multiple transcript variants, the longest protein-coding
814 transcript sequence was chosen for PCR amplification and cloned into pEGFP-C1
815 vector as described previously (Dopie et al., 2020). Briefly, total RNA was isolated using
816 the RNeasy kit (Qiagen, cat#74104) and 1μg total RNA was reverse transcribed using
817 the Protoscript First Strand cDNA Synthesis Kit (New England Biolabs, cat# M0368S) to
818 generate cDNA. Using primers containing the appropriate restriction enzyme sites
819 (STable 1), cDNA amplicons were PCR amplified with Q5 High-Fidelity DNA
820 Polymerase (New England Biolabs, cat# M0491S), purified and cloned into pEGFP-C1
821 (originally obtained from Clonetech). The sequences of all plasmids generated were
822 validated by Sanger sequencing before their use.
823 For transfections, ~120,000 U2OS cells were seeded per well in a 6-well plate
824 containing 12mm diameter #1.5 coverslips (Electron Microscopy Sciences, cat#72230-
825 01) and the next day, 500 ng of plasmid was transfected using 5ul Lipofectamine 2000
826 (Thermo Fisher Scientific, cat#11668019) in OptiMEM (Thermo Fisher Scientific, cat#
827 31985070) as per the manufacturer's instructions. After 24 hours, cells were fixed with
828 freshly prepared 4% paraformaldehyde (Sigma, cat#P6148) in calcium and magnesium
829 free phosphate buffered saline (CMF-PBS) for 10 mins at room temperature (RT). Cells
830 were washed for 5 mins 3 times with CMF-PBS and then either mounted directly using
831 Mowiol-DABCO antifade mounting medium or processed further.
832
833 **Antibody generation**

834 A rabbit polyclonal anti-DDX39B antibody (Pacific Immunology) was generated
835 against the 24 amino acid synthesized peptide (Cys)-DRFEVNISELPDEIDISSYIEQTR,
836 conserved across human, mouse and Chinese hamster DDX39B protein sequences.
837 Briefly, two rabbits were immunized once with AdjuLiteTM Complete Freund's Adjuvant
838 followed by three rounds of AdjuLiteTM Incomplete Freund's Adjuvant immunizations.
839 The first production bleed was validated by ELISA against the peptide used for
840 immunization. After validation, serum from both rabbits was pooled prior to affinity
841 purification. 25 mL pooled serum was subjected to affinity purification using the same
842 target peptide. This affinity-purified antibody was diluted in 50% glycerol for long-term
843 storage at a concentration of 0.6 mg/ml. The antibody was further validated by
844 demonstrating its colocalization after immunostaining with the mCherry-DDX39B signal
845 in a U2OS cell line with the endogenous DDX39B gene tagged with mCherry (See "Cell
846 Line Construction" Section, below).
847
848 **Immunostaining**
849 Cells were fixed with freshly prepared 4% (w/v) paraformaldehyde solution in
850 CMF-PBS (pH 7.0) (Sigma-Aldrich, cat# P6148) for 10 mins at RT. Coverslips were
851 washed three times with CMF-PBS and cells were permeabilized with 0.5 % Triton X-
852 100 in CMF-PBS for 10 mins at RT. Washes for 5 mins with CMF-PBS were repeated
853 three times followed by blocking for 1 hr at RT in 5% (v/v) goat serum solution prepared
854 in 0.1 % Triton X-100 in CMF-PBS. Primary antibodies were diluted as stated (STable
855 1) in blocking buffer and applied to coverslips overnight at 4°C for 12-16 hours in a
856 humidified chamber. Coverslips then were washed for 5 mins three times using 0.1 %

857 Triton X-100 in CMF-PBS at RT. Secondary antibodies were diluted as stated (STable
858 1) in blocking buffer and applied to coverslips for 1 hr at RT in a humidified chamber
859 before 5 min washes with 0.1 % Triton X-100 in CMF-PBS repeated three times.
860 Coverslips were mounted using Mowiol-DABCO antifade mounting medium without or
861 with DAPI (Sigma-Aldrich cat#D9542) (10ug/ml).
862
863 **Cell line construction**
864 Knock-in cell lines containing endogenous gene sequences tagged with different
865 fluorescent proteins were constructed using CRISPR/Cas9 as described previously
866 (Gholamalamdari et al., 2025). For gRNA synthesis, a 2-step overlap PCR strategy was
867 employed. In the first step, a forward primer including the T7 promoter sequence
868 followed by the target specific sequence 20bp immediately upstream of the PAM
869 sequence and a reverse primer containing the tracrRNA template sequence (5'-
870 AAAAGCACCGACTCGGTGCCACTTTTTCAAGTTGATAACGGACTAGCCTTATTTTAA
871 CTTGCTATTTCTAGCTCTAAAAC -3') (STable 1) were used. This first step generated
872 a 120bp T7-gRNA-tracr fragment. In the second step, we amplified this DNA template
873 using a T7 promoter sequence forward primer (5'-TAATACGACTCACTATAG-3') and a
874 reverse primer sequence (5'- AAAAGCACCGACTCG-3').
875 This DNA template was gel purified (QIAGEN # 28704) and used for an in vitro-
876 transcription reaction to generate gRNA. 1 µg of DNA template was incubated with
877 2.5mM ribonucleotides (NTP, New England Biolabs cat#N0466S), 1U/µl Ribolock
878 RNase inhibitor (Thermo Fisher Scientific, cat# EO0381), 8 µl T7 RNA Polymerase
879 (purified in the laboratory) in 50 µl reaction volume in IVT buffer (50mM Tris-HCl, pH

880 7.6, 15mM magnesium chloride, 5mM dithiothreitol (DTT) and 2mM spermidine). The
881 reaction was incubated at 37°C for 6-16 hours in a thermocycler. In-vitro transcribed
882 product was treated with 2.5 U DNase I (2 U/µl; New England Biolabs cat# M0303S) at
883 37°C for 15 mins to remove the DNA template prior to purification. gRNA was purified
884 using the RNeasy plus kit (QIAGEN cat# 74134). Purified gRNAs eluted in RNase-free
885 water (Accugene cat#51200) were stored as aliquots at -80°C.

886 2 µg of target-specific gRNAs were complexed with 3µg purified Cas9 Nuclease
887 V3 (Integrated DNA Technologies, cat# 1081058). gRNA sequences and primers used
888 for homology arms of Donor DNA sequences are provided in STable 1. Primers 70-90
889 bp long with their 5' end modified with an amine group coupled to a C6 linker (Yu et al.,
890 2020) were used for generating donor DNA with homology arms including sequences
891 upstream and downstream of the target genomic DNA cut site; (STable 1). PCR
892 amplification of the donor DNA used Q5 High-Fidelity DNA Polymerase (New England
893 Biolabs, cat# M0491S) and was applied to a plasmid or BAC template DNA containing
894 sequences coding for the fluorescent protein and linker peptide to be added to the NH2-
895 terminus of the target protein (STable1). This donor DNA was purified after the PCR
896 using magnetic beads (MAGBIO, HighPrep PCR, cat#AC-60050). Nucleofection was
897 performed using an Amaxa Nucleofector II device (Lonza) as per the manufacturer's
898 instructions.

899 After 5 days of recovery, fluorescence-positive cells were sorted using the FACS
900 ARIA II sorter at the UIUC Roy J. Carver Biotechnology Center. Using this approach,
901 the "U2OS EGFP-SON C5" cell clone was first generated. U2OS EGFP SON C5 was
902 then further modified to generate the "U2OS EGFP-SON C5 mCherry-DDX39B C11"

903 cell clone and the "U2OS EGFP-SON C5 mCherry-THRAP3 gRNA#1" mixed clonal cell
904 line. Similarly, a U2OS HaloTag-SON" mixed clonal cell line was generated and then
905 further modified to generate the "U2OS HaloTag-SON EGFP-THRAP3 gRNA#1" mixed
906 clonal cell line (STable1).

907 HCT116 SON and SRRM2 double-degron cell line (expressing mAID-Clover-
908 SON and SRRM2-mAID-mCherry) was generated by CRISPR-Cas9-mediated genome
909 editing as previously described (Yesbolatova et al. Nat. Commun., 2020; Saito et al.
910 Current Protocols, 2021). Briefly, we initially fused mAID-mCherry to the C-terminus of
911 SRRM2. For this, we designed a CRISPR-Cas9 plasmid for targeting the SRRM2 locus
912 (5'-AGGTCTCCATAAATTGTCTT(TGG)-3'). A donor plasmid harboring mAID-mCherry
913 and a selection marker (BSD) with two homology arms (approximately 500 bp each)
914 was constructed. HCT116 cells stably expressing OsTIR1(F74G) from the AAVS1 locus
915 were transfected with the CRISPR and donor plasmids. Clones surviving blasticidin
916 selection were screened for biallelic by genomic PCR, and expression of the fusion
917 protein was confirmed by immunoblotting. Subsequently, we fused mAID-Clover to the
918 N-terminus of SON. For this, we designed a CRISPR-Cas9 plasmid for targeting the
919 SON locus (5'-AGAGAACGGAGCGGACGCCA(TGG)-3'). A donor plasmid harboring
920 HygroR-P2A-mAID-mClover with two homology arms was constructed. The SRRM2-
921 mAID-mCherry cells were transfected with the CRISPR and donor plasmids for tagging
922 SON. Clones surviving hygromycin selection were screened for biallelic insertion of the
923 tagging construct by genomic PCR, and expression of the fusion protein was confirmed
924 by immunoblotting. To induce degradation of SON and SRRM2, 5-Ph-IAA was added to
925 the final concentration of 1 μM.

926

927 **Transcriptional inhibition treatment**

928 30,000 U2OS cells were seeded per #1.5 12 mm diameter coverslip (Electron
929 Microscopy Sciences, cat# 72230-01) in a 24-well plate. After two days, cells were
930 treated with 50 µg/ml DRB (Sigma-Aldrich, cat# D1916), 50 µg/ml α-amanitin (Sigma-
931 Aldrich, cat# A2263), or 0.1 µg/ml triptolide (Sigma-Aldrich, cat# T3652) added in
932 McCoy's 5A media for the time indicated and fixed. For heat shock experiments, cells
933 were seeded on #1.5 12 mm coverslips placed within 35mm dishes (Corning, cat#
934 430165) at 120,000 cells per dish. After two days, cells were incubated in a water bath
935 at 42°C after sealing the dishes with parafilm (Parafilm, cat# S25929) for the indicated
936 time and fixed immediately.

937

938 **Tyramide Signal Amplification-sequencing (TSA-seq)**

939 A detailed protocol for TSA-seq is described elsewhere (Zhang et al., 2022). For
940 high-resolution mapping, we combined the use in the original TSA-seq 1.0 procedure
941 (Chen et al., 2018) of both sucrose and Dithiotheitol (DTT) to increase spatial resolution
942 with the higher tyramide concentration and longer TSA reaction time used in the TSA-
943 seq 2.0 protocol, which saturated the protein TSA labeling but increased the DNA
944 tyramide labeling without saturation (Zhang et al., 2021). More specifically, we used a
945 TSA reaction buffer prepared in CMF- PBS with 50% sucrose: 1.5 mM DTT (Millipore
946 Sigma, cat#233155-10GM), and 0.33 mM tyramide-biotin (Apex-Bio, cat# A8011) with a
947 reaction time of 30 mins. By boosting the tyramide concentration beyond previous TSA-
948 seq 2.0 TSA reaction conditions, we compensated for the decreased TSA-labeling

949 caused by the addition of the DTT, while keeping the nucleic acid labeling
950 undersaturated as judged by microscopy as described previously (Zhang et al., 2021).
951 For each TSA-seq sample in U2OS cells, cells were grown in two T-300 flasks
952 (~15 million cells per T-300 flask). For each TSA-seq sample in HCT116 cells, cells
953 were grown in one T-150 flask (~30-40 million cells). For the TSA-seq of the HCT116
954 mAID-Clover-SON SRRM2-mAID-mCherry CMV-OsTIR1(F74G) cell line, cells in T-150
955 flasks were first treated with either DMSO (Avantor # IC0219605590) or 5μM 5-Ph-IAA
956 (Tocris Biosciences #7392) for 4 hours before proceeding to the TSA-seq procedure.
957 All TSA-seq libraries were prepared using 3-10 ng of purified DNA using the
958 TruSeq ChIP Library Preparation Kit (Illumina, cat# IP-202-1012) as per the
959 manufacturer's instructions. Libraries were PCR-amplified for 8 cycles and purified
960 using AMPure XP magnetic beads (Beckman Coulter, cat# A63881). Concentrations of
961 individual libraries were estimated by qPCR and then pooled accordingly. They were
962 then sequenced from one end of the fragments on a NovaSeq X Plus with V1.0
963 sequencing kits. FASTQ files were generated and demultiplexed with the bcl-convert
964 v4.1.7 Conversion Software (Illumina). TSA-seq normalization, scores and identification
965 of changed regions were performed using a previously reported pipeline (Chen et al.,
966 2018; Zhang et al., 2021).
967
968 **Oligolibrary design and probe synthesis**
969 For DNA FISH of TSA-seq peaks, we used an oligolibrary containing ~500 FISH
970 probes targeted to DNA sequences within each ~100 kb targeted peak region (STable
971 1). Oligo probes (STable 1) were designed using PAINTSHOP (https://paintshop.io/) as

972 per published recommendations (Beliveau et al., 2012, 2017). Briefly, selected genomic
973 region coordinates were uploaded and advanced probe settings specified as: no
974 repeats allowed, max off-target score 15, max K-mer count 5, Min prob value 0 and
975 probe set optimized to generate ~500-523 probes per 100 kb target with “trim” setting
976 for each region. Each probe set was appended with universal outer primers for each
977 TSA-seq peak type, and a unique inner primer set for each 100 kb genomic peak
978 region. The 3’ inner and outer primer was followed by the T7 promoter sequence.
979 For trajectory mapping, the distances between two consecutive ~100 kb regions
980 were kept at least 200 kb apart between the nearest edges of two neighboring regions.
981 The outer primer was unique for “Apex” and “Arm” regions and each 100 kb genomic
982 region had a unique inner primer set. The 3’ inner and outer primer was followed by the
983 T7 promoter sequence. Otherwise, settings for probe selection were kept the same as
984 for the TSA-seq peak probe selection.
985 For RNA-FISH, ~100 probes were selected for MALAT1 RNA. The outer primer
986 was unique for the target. The outer primer was followed by the T7 promoter sequence.
987 Otherwise, settings for probe selection were kept the same as used for the DNA FISH
988 probe selection.
989 The detailed protocol used for probe preparation is described elsewhere
990 (Beliveau et al., 2017). Briefly, probes were amplified using PCR with Q5 High-Fidelity
991 DNA Polymerase for 7-8 cycles, followed by in-vitro transcription using HiScribe T7 High
992 Yield RNA Synthesis Kit (New England Biolabs cat# E2040S) and reverse-transcription
993 using Maxima H Minus Reverse Transcriptase (Thermo Fisher Scientific cat# EP0751)
994 as described previously (Beliveau et al., 2017).

995 2 μl of reactions were loaded on a urea-TBE gel to check for the desired ~70-
996 80% incorporation of reverse transcription RT primer (20bp) into the probes (~150 bp).
997 Probes were purified using Zymo DCC-25 columns as described previously (Beliveau et
998 al., 2017).
999 2 μg purified probes were end-labelled using 12U Terminal Deoxynucleotidyl
1000 Transferase (TdT 20U/μl; Thermo Scientific, cat# EP0161) in TdT buffer (Thermo
1001 Scientific, cat# EP0161) with 108μM unlabelled dATP or dTTP and 54μM Biotin-dATP
1002 (Invitrogen #19524016) or Digoxigenin-11-dUTP (Roche #11093088910) respectively in
1003 a 25 μl reaction volume. Reactions were incubated at 37°C for 1hr in a thermocycler.
1004 Probes were purified using the QIAquick Nucleotide Removal kit (QIAGEN, cat# 28306).
1005 Probes were eluted in 100 μL molecular biology grade water (Accugene, cat#51200)
1006 and human Cot-1DNA (Invitrogen #15279011) was added to each probe such that
1007 human Cot-1 DNA was 10x higher than the probe concentration. The resulting probe
1008 solutions were concentrated using a Vacufuge concentrator (Eppendorf) with the
1009 settings for aqueous solutions at 45°C for 45 mins until the probe solutions were
1010 reduced to ~2-5 μl volumes. To these solutions, equal volumes of 100% formamide
1011 (Sigma-Aldrich, cat#F9037) and 2x hybridization buffer (20% w/v dextran sulphate
1012 (Sigma-Aldrich, cat# D8906) in 4x Saline-Sodium Citrate (SSC) buffer) are added such
1013 that the final probe concentrations are 25 ng/μl in hybridization buffer (10% w/v dextran
1014 sulphate in 2X SSC buffer with 50% formamide).
1015
1016 **DNA-FISH**

1017 Cells were fixed and immunostained as described previously (Solovei and
1018 Cremer, 2010). Briefly, cells were immunostained as described above with the
1019 exception of replacing the goat serum with 5% Bovine Serum Albumin (Sigma-Aldrich
1020 cat#A9418) for blocking and post-fixing after the immunostaining using 2%
1021 paraformaldehyde in CMF-PBS buffer. After three 5 min washes with CMF-PBS,
1022 coverslips were incubated with 20% glycerol (Fisher Scientific, cat# BP229-1) in CMF-
1023 PBS for 24 hours. Coverslips underwent 6 rounds of freezing and thawing in 20%
1024 glycerol in PBS with liquid nitrogen immersion followed by three 5 min washes with
1025 CMF-PBS containing 0.1% Triton X-100 (Thermo Fisher Scientific, cat# 28314).
1026 Coverslips were then rinsed with 0.1 N HCl in molecular biology grade water
1027 (Accugene, cat#51200) and incubated in same at RT for 10 mins. Three 5 min washes
1028 with CMF-PBS containing 0.1% Triton X-100 were followed by immersion in 2x SSC
1029 containing 50% formamide at 4°C for at least 3 days and up to 15 days. For
1030 hybridization, oligolibrary probes (100-125ng of labelled oligoprobes in 10% dextran
1031 sulphate in 2X SSC buffer containing 50% formamide and 1μg of unlabelled human Cot-
1032 1 DNA (Invitrogen cat#15279011) were added to a glass slide and the 12 mm circular
1033 #1.5 mm coverslip was inverted and sealed using rubber cement (Elmers).
1034 The slide was placed on a heating block at 75°C for 3 mins and then immediately
1035 moved to a humidified chamber at 37°C for 4 days of hybridization. Post-hybridization,
1036 coverslips were removed from the slide and washed for 10 mins three times with 2x
1037 SSC at 37°C followed by two 5 min washes with 0.1x SSC at 60°C.
1038 Probes were detected using anti-Digoxin antibody (Jackson #200-602-156) or
1039 Streptavidin (Jackson #016-600-084) conjugated to Alexa 647 diluted 1:200 in 4% BSA

1040 in 4x SSC containing 0.2% Tween20 (Sigma-Aldrich, cat# P1379) at RT for 1 hr in a
1041 humidified chamber. Three 5 min washes were performed using 4x SSC with 0.2%
1042 Tween20 at 37°C. Coverslips were rinsed with CMF-PBS containing 0.1% Triton X-100
1043 and mounted with DABCO containing mounting medium with/without DAPI.
1044
1045 **RNA-FISH**
1046 smRNA-FISH was performed as reported previously (Kim et al., 2020). All
1047 reagents used for this procedure were RNase free and/or diethyl pyrocarbonate
1048 (DEPC)-treated (Sigma-Aldrich cat# D5758). Cells were fixed with 4%
1049 paraformaldehyde for 10 mins at RT in CMF-PBS. Three 5 min washes in CMF-PBS
1050 were followed by permeabilization with 0.5% Triton X-100 in CMF-PBS for 10 min at RT
1051 followed by 3x 5 min washes in CMF-PBS. Cells were equilibrated using 10%
1052 formamide in 2X SSC for 30 min at RT.
1053 smRNA FISH probes designed against HSPA1A (Kim et al., 2020), HSPH1
1054 (Zhang et al., 2021), and oligolibrary probes designed against MALAT1 (STable 1) were
1055 used at a final concentration of (~300-500nM in hybridization buffer composed of 10%
1056 formamide, 10% (w/v) dextran sulphate (Sigma-Aldrich, cat# D8906), 1 mg/ml
1057 Escherichia coli tRNA (Sigma-Aldrich, cat# R8759), 2 mM ribonucleoside vanadyl
1058 complex (NEB, cat# S1402), and 0.02% RNase-free BSA (Invitrogen, cat# AM2618) in
1059 2X SSC. For Stellaris MALAT1-Quasar670 probes (Stellaris, cat# SMF-2046-1), 1.25μM
1060 final concentration was used instead of the recommended 0.125μM. Probe solution in
1061 hybridization buffer were applied to coverslips followed by incubation at 37°C for 15
1062 hours in a humid chamber. Two 30 min washes with 10% formamide in 2X SSC at 37°C

1063 were followed by post-fixation with 3.6 % paraformaldehyde in CMF-PBS buffer for 10
1064 min at RT, followed by 3 x 5 min washes with CMF-PBS.
1065 Coverslips were incubated with blocking buffer containing 1% BSA (RNase-free,
1066 Invitrogen, cat# AM2618), 0.5% Triton X-100 and 20μM ribonucleoside vanadyl complex
1067 (NEB, cat# S1402) in CMF-PBS for 30 min at RT. Coverslips were then rinsed three
1068 times with CMF-PBS, followed by incubation with the appropriate antibody titer (STable
1069 1) diluted in CMF-PBS with 0.1% Triton X-10 containing 0.4 U/μl Ribolock RNase
1070 inhibitor (Thermo Fisher Scientific, cat# EO0381) for 45 min-1 hour at RT in a humid
1071 chamber. Coverslips were then washed 3 x 5mins with 0.1% Triton X-100 in CMF-PBS
1072 for 5 minutes each. Secondary antibody incubation was performed similar to the primary
1073 antibody incubation except that the fluorescently tagged Goat anti-Rabbit / Goat anti-
1074 Mouse secondary antibodies (STable 1) were diluted at 1:500. Subsequently, coverslips
1075 were washed 3 x 5 mins in CMF-PBS with 0.1% Triton X-100 and mounted using
1076 Mowiol-DABCO antifade mounting medium.
1077
1078 **Wide-field fixed-cell imaging**
1079 Wide-field images were acquired (0.08 um pixel size) using an OMX V4
1080 microscope (Applied Precision) equipped with a U Plan S-Apo 100×/1.40-NA oil-
1081 immersion objective (Olympus), two Evolve electron-multiplying Charge-Coupled Device
1082 cameras (Photometrics). Images were aligned and deconvolved using the conservative
1083 deconvolution option within the Softworx program (Applied Precision).
1084
1085 **STORM imaging**

1086 For 2-color STORM imaging, we used the U2OS cell line expressing mEOS3.2-
1087 DDX39B from the endogenous locus as described elsewhere (Kim et al., 2025). Cells
1088 were fixed with 3.6% paraformaldehyde in CMF-PBS for 15 mins at RT, washed 3 x 5
1089 mins in CMF-PBS, and then incubated in blocking buffer (3% BSA (Thermo Scientific,
1090 cat# 37520), 0.5%Triton X-100 in CMF-PBS) for 30 mins at RT, followed by 3 x 5 min
1091 washes in CMF-PBS. Coverslips were incubated overnight at 4°C with the anti-THRAP3
1092 primary antibody (Santa Cruz Biotechnology Inc, cat# sc-133250) at 1:300 dilution in
1093 1% BSA in CMF-PBS.
1094 Coverslips were then washed 3 x 5 mins in CMF-PBS and then incubated for 2
1095 hours at RT with the goat anti-mouse Fab (Jackson ImmunoResearch, cat# 115-007-
1096 003) labeled with Alexa 647 at 5μg/ml at final concentration in 1% BSA in CMF-PBS.
1097 The Fab fragment was labeled with Alexa 647 (Invitrogen, Cat A20006) as described
1098 elsewhere (Hermanson, 2013; Bates et al., 2013). After this secondary antibody
1099 staining, coverslips were washed 3 x 5 mins in 0.1%Triton X-100 in CMF-PBS and then
1100 washed 2 x 5mins in CMF-PBS.
1101 The STORM imaging microscope system was described elsewhere (Kim et al.,
1102 2025). Alexa 647 signals were collected first, under continuous excitation with 647 nm
1103 laser (2kW/cm^2) and brief manual illumination with 405 nm LED illumination (0.1-0.5%
1104 intensity, Aura Light, Engine) for dye reactivation. Imaging was performed using a
1105 previously described imaging buffer (Bates et al., 2007), containing 5% glucose (Sigma-
1106 Aldrich, cat# G8270), 1% Glox (0.5mg/ml glucose oxidase, Sigma-Aldrich, cat#
1107 G2133), 40mg/ml catalase (Sigma-Aldrich cat# C100, in 50mM Tris with 10mM NaCl
1108 and 100 mM beta-mercaptoethanol (BME, Sigma-Aldrich, cat# M6250)). mEOS3.2

1109 signals were then acquired under continuous excitation with 561 nm laser (1.5kW/cm^2),
1110 and with brief manual illumination with 405 nm LED illumination for dye reactivation.
1111 Images were acquired at 15-20ms per frame in continuous mode, for a total of
1112 30000~50000 frames. Localization, drift correction, and chromatic alignment were
1113 performed using SMAP (Li et al., 2018; Ries, 2020).
1114
1115 **Live cell imaging**
1116 **Rapid wide-field imaging for short-term dynamics (second-timescale)**
1117 Cells were plated (~48 hours before imaging) on uncoated glass bottom 35 mm
1118 dishes with 14mm diameter and 1.5 thickness coverslip (MatTek, cat# P35G-1.5-14-C)
1119 such that cells were ~80-90% confluent at the time of imaging. For cell lines expressing
1120 proteins tagged with HaloTag, conditioned media containing Janelia Fluor(R) 646
1121 HaloTag(R) Ligand (Promega, cat# GA1120) diluted 1:5000 was added for 1-2 hours
1122 before imaging.
1123 For live-cell imaging we used the OMX V4 microscope together with a live cell
1124 incubator chamber (Applied Precision) and system including separate temperature
1125 control for the objective lens and incubator chamber and a humidified, 5% CO_2 air
1126 supply. Both the objective lens and incubator heaters were set to 37°C; after these
1127 temperatures were reached, the cell culture dish was placed on the microscope and
1128 cells were allowed to acclimatize to these conditions for ~1hr before beginning imaging.
1129 Imaging was performed using simultaneous solid-state illumination with 31.3%
1130 transmittance for THRAP3/DDX39B and 10% transmittance for SON using 10-15 ms

1131 exposure for each Z-section. Optical section z-stacks (Z spacing 200 nm, ~ 1 micron z-
1132 depth) were acquired every 1 sec for 1-2 mins.
1133
1134 **Wide-field imaging for long-term dynamics (multiple hour-timescale)**
1135 Live cell imaging for greater than 10 hours was performed as described elsewhere (Kim
1136 et al., 2025) using a custom-built microscope setup.
1137
1138 **5-Ph-IAA induced SON-SRRM2 degradation**
1139 SON and SRRM2 double knockdown in the HCT116 mAID-Clover-SON SRRM2-
1140 mAID-mCherry cell line was achieved by adding to the media 5-phenyl-1H-indole-3-
1141 acetic acid (5-Ph-IAA, Tocris Biosciences, cat # 7392) to a final concentration of 5μM
1142 using a stock solution of 10mM in dimethyl sulphoxide (DMSO, Avantor cat#
1143 IC0219605590).
1144 For live cell visualization of DDX39B during SON and SRRM2 DKD, the HCT116
1145 mAID-Clover-SON SRRM2-mAID-mCherry cell line was transfected with the Halotag-
1146 DDX39B plasmid (STable 1) and selected in cell culture media containing 450 μg/ml
1147 G418 (Gibco,cat# 10131035) for ~ 2 weeks. Cells expressing Halotag-DDX39B were
1148 stained overnight with JF646 (50 pM Promega cat# GA1120). After adding 10~20μM 5-
1149 Ph-IAA, we acquired live cell movies to observe SON and SRRM2 degradation while
1150 visualizing Halotag-DDX39B.
1151
1152 **RNP transgene induction and RNP localization relative to DDX39B, THRAP3, and**
1153 **SON / SRRM2 (NS)**

1154 U2OS cell lines stably expressing the E6 β-globin and mini-Dystrophin A-1
1155 transgenes tagged with the MS2 repeats and expressing a YFP-fused MS2 binding
1156 protein (Mor et al., 2010; Brody et al., 2011), were seeded (~30,000 cells) on 12mm
1157 #1.5 coverslips (Electron Microscopy Sciences cat# 72230-01). For E6, cells were
1158 treated with 15 µg/ml doxycycline (Sigma-Aldrich cat#D5207) for 6, or 16 hours, while
1159 mini-dystrophin cells were treated with 1 µg/ml Ponasterone A (Enzo Life Sciences) for
1160 the same durations to induce transgene expression. Cells were fixed in 4% PFA for 20
1161 mins at RT. Cells were permeabilized in 0.5% Triton X-100 in 1x PBS for 10 min, and
1162 blocking was applied using a buffer composed of 0.1% Triton X-100 and 5% bovine
1163 serum albumin (BSA) fraction V (MP Biomedicals cat# 160069) for 1 hour at RT.
1164 Primary antibodies were diluted in blocking buffer (STable 1) and applied to coverslips
1165 overnight at 4°C for 16 hours in a humidified chamber. Coverslips then were washed for
1166 5 mins three times using 0.1 % Triton X-100. This was followed by incubation with
1167 secondary antibodies for 1 hour at RT and then washes for 5 mins three times using 0.1
1168 % Triton X-100. The nucleus was stained with SYTOX deep red nucleic acid stain
1169 (Invitrogen cat# S11381) for 20 min, followed by final rinses with 1x PBS. Secondary
1170 antibodies used; Alexa Fluor 405-conjuated goat anti rabbit IgG (1:500, Abcam cat#
1171 ab175652) and Rhodamine red-conjugated donkey anti mouse IgG (1:250, Jackson
1172 Immunoresearch cat# 715-297-003).
1173 Confocal imaging was performed on a Leica SP8 inverted microscope. The
1174 objective used was 100x 1.4 NA, with Leica immersion oil, at room temperature. The
1175 mounting medium was custom made 80% glycerol with p-phenylenediamine antifade
1176 (Sigma). The resulting images were deconvolved with Huygens Professional (Scientific

1177 Volume Imaging, Hilversum, The Netherlands) using the CMLE algorithm, with signal-
1178 to-noise ratios of 12 and 5 iterations, using the Huygens confocal module.
1179
1180 **RNA-Seq sample preparation and analysis**
1181 **Cell synchronization and protein depletion:** For synchronization at the G1/S
1182 boundary (JavanMoghadam-Kamrani and Keyomarsi, 2008), HCT116 mAID-Clover-
1183 SON SRRM2-mAID-mCherry CMV-OsTIR1(F74G) cells were seeded in 6-well plates
1184 and grown to approximately 80% confluency, followed by treatment with 20 μM
1185 Lovastatin (Mevinolin; LKT Laboratories, cat# M1687) for 24 hours. To release the G1
1186 arrest but block cells at the G1/S boundary, cells were rinsed three times with pre-
1187 warmed, CO_2-equilibrated culture medium supplemented with 2 mM Mevalonic acid
1188 (Mevalonolactone; Millipore-Sigma cat# M4667) and 2 mM thymidine (Millipore-Sigma,
1189 cat# T9250).
1190 Degradation of AID-tagged proteins was induced by the addition of 5 μM 5-Ph-
1191 IAA simultaneously with the release of the G1 block by addition of the Mevalonic
1192 acid/thymidine-containing media. Cells were incubated for 16 hours after this G1 block
1193 release. Control cells were treated the same except that an equivalent volume of DMSO
1194 without added 5-Ph-IAA was added. The G1 arrest followed by addition of 5-Ph-IAA
1195 coincident with the release of this block for the G1/early S synchronization was used to
1196 minimize cell cycle-related variability between DMSO-treated controls and the
1197 SON/SRRM2-depleted samples.
1198

1199 **RNA extraction and RNA-seq:** Cells in a 6-well plate were rinsed twice with ~1
1200 mL of cold CMF-PBS per well, and total RNA was extracted immediately using the
1201 RNeasy Plus Mini Kit (Qiagen, cat# 74134), following the manufacturer's protocol.
1202 Purified RNA eluted in RNase-free water was treated with 2U DNase I (New England
1203 Biolabs, cat# M0303S) for 20 mins at 37°C, followed by DNase I inactivation by adding
1204 5 μM EDTA (Thermo Fisher Scientific, cat# J15694.AE) and 10 mins incubation at 75°C.
1205 RNA integrity was assessed at the DNA Services Facility, Roy J. Carver
1206 Biotechnology Center (University of Illinois at Urbana-Champaign), using an Agilent
1207 Bioanalyzer. All samples exhibited RNA Integrity Numbers (RIN) of 10. Ribosomal RNA
1208 was depleted using the FastSelect HMR kit (Qiagen, cat# 334386). RNA-seq libraries
1209 were prepared with the KAPA HyperPrep Stranded mRNA Library Kit (Roche, cat#
1210 KK8580), quantified by qPCR, pooled, and sequenced on a NovaSeq X Plus instrument
1211 using V1.0 sequencing chemistry for 151 paired-end cycles. Adapter trimming was
1212 performed on the 3′ ends of reads, using the first 33 nucleotides of the adapter
1213 sequences for trimming. FASTQ files were generated and demultiplexed using
1214 Illumina's bcl2fastq v2.20 software.
1215
1216 **RNA-seq analysis:** The quality of trimmed reads was assessed using FastQC
1217 with default parameters. High-quality reads were aligned to the human reference
1218 genome (GRCh38/hg38) using STAR aligner (Dobin et al., 2013), with the
1219 corresponding GTF annotation file obtained from Ensembl. Differential gene expression
1220 analysis was performed using the DESeq2 R package (Love et al., 2014) using DMSO-

1221 treated samples as controls. Genes with an adjusted p-value (Padj) < 0.05 (Benjamini-
1222 Hochberg correction) were considered significantly differentially expressed (STable 2).
1223
1224 **Image analysis**
1225 All fixed-cell images shown are single optical sections unless indicated
1226 otherwise. Non- linear exponential gamma scaling of 0.8 was applied to all images of
1227 DDX39B, MALAT1 and RBM8A to reduce the intensity dynamic range and thus facilitate
1228 the visualization of low-intensity nuclear regions. Images presented in the live-cell
1229 imaging videos are 2D maximum-intensity projections of the original optical section z-
1230 stacks acquired at each time point. All images were processed using Fiji (ImageJ)
1231 (Schindelin et al., 2012).
1232
1233 **Protein-intensity quantification within and outside NS**
1234 A single optical z-section containing the max-signal over the entire z-stack for NS
1235 (SON or SRRM2) was selected using the np.max function in the Python NumPy
1236 package (Harris et al., 2020). The intensity distribution of each candidate protein inside
1237 versus outside of NS was assessed as follows: Pixels with intensities < 10% of the
1238 maximum signal of the protein were considered “noise” and discarded. A nuclear mask,
1239 established by DAPI staining, was applied to both the NS and candidate protein images.
1240 NS were defined by SON/SRRM2 intensity thresholds established using Otsu
1241 thresholding (Otsu, 1979). The remaining pixels showing candidate protein "positive"
1242 signals (>10% maximum intensity threshold) were then divided into two categories:
1243 “Protein within NS” for pixels overlapping with the NS segmented regions and “Protein

1244 outside NS" for remaining positive pixels outside the NS segmented regions. The
1245 resulting images were displayed using the "viridis" LUT color-map. Cumulative-intensity
1246 percentile plots of the "Protein within NS" and "Protein outside NS" staining distributions
1247 were generated using the Python package Matplotlib (Hunter, 2007).
1248

1249 **Network changes upon transcriptional inhibition with DRB**

1250 A Fiji macro ("Skeletonize", See Code Availability Section) was created for this
1251 quantification. Briefly, for each image, the SON channel was used to generate a NS
1252 mask. Then, all pixels of the protein channel that overlapped with the NS mask were set
1253 to zero intensity to generate an image of only the protein outside NS. The resultant
1254 image was converted into a binary image using Otsu thresholding (Otsu, 1979). Using
1255 the Fiji Skeletonize function (fiji.sc/Skeletonize3D), "protein skeletons" were generated,
1256 and branch lengths and number of branches/skeleton were calculated. Total skeleton
1257 length was computed by summing the lengths of all the skeletons within a nucleus.
1258 Number of connections was the number of unique skeletons (length > 5 pixels)
1259 identified within a single nucleus.
1260

1261 **Distance measurement for RNA Pol II foci relative to SON, THRAP3 and DDX39B**
1262 **networks**

1263 RNA Pol II Ser2p and Ser5p staining foci locations were determined using the
1264 'Find Maxima' function in ImageJ. Detected locations were assigned a pixel value of 1,
1265 while all other pixel values were set to 0, converting the Pol II image into a binary image
1266 containing only Pol II locations. The binary image was then imported into a custom

1267 MATLAB code for distance measurements relative to NS
1268 (https://github.com/Jiahkim/distancebtwlocusNS.git) . Pol II-positive pixels were first
1269 classified based on whether they overlapped with NS regions. NS areas were defined
1270 by segmentation of a target NS marker using local thresholding (Bradley and Roth,
1271 2007). For Pol II-positive pixels outside NS area, distances to the nearest pixel at the
1272 NS boundary were as calculated.
1273

1274 **Distance measurement for Type I and Type II DNA-FISH spots relative to SON,**
1275 **THRAP3 and DDX39B**

1276 To measure distance of a spot to SON, THRAP3 and DDX39B, we used the
1277 Loci_Compartment_Distance ImageJ plugin described elsewhere (Kumar et al., 2024).
1278 Since the THRAP3 and DDX39B networks are widely distributed within the nucleus, and
1279 due to limited Z-resolution, we used a single optical section for THRAP3 and DDX39B
1280 analysis. For NS detection, we used the sum-projection of 3 optical sections centered
1281 over the brightest spot of the locus. To define the edge of the compartment boundary,
1282 the intensity drop of 50% of the local maximum intensity (after background correction)
1283 was used to locally segment the image. The center of mass of the DNA FISH spot
1284 signal was used as the spot center location and the shortest distance between the spot
1285 center to the nearest compartment edge was measured.
1286

1287 **Categorizing and assessing alignment of DNA-FISH trajectories relative to SON,**
1288 **THRAP3 and DDX39B foci**

1289 To eliminate DNA FISH background staining signals, for the DNA FISH mapping
1290 of chromosome trajectories, only the "Apex" biotin signals that colocalized adjacent to
1291 DNA-FISH signals for the “Arm” regions were considered as true positive Apex signals.
1292 Additionally, the Apex signal had to be at least 2-fold higher intensity than single biotin
1293 spots seen elsewhere in the nucleus to be considered for analysis. For analysis, a sum-
1294 projection was generated of all the consecutive optical sections which contained an
1295 individual trajectory FISH signal consisting of positive DNA-FISH Apex and Arm signals.
1296 Chromosome trajectories were categorized as condensed if the Arm region appeared
1297 as a single spot or blob next to an Apex DNA-FISH spot. Any Arm region appearing as
1298 2 or more spots was termed “decondensed”. For alignment, a trajectory was considered
1299 aligned only if all the spots of the Arm and Apex were either overlapping or adjacent and
1300 in-contact to THRAP3 or DDX39B foci. In all other cases, the chromosome trajectory
1301 was classified as not aligned.
1302
1303 **Distance measurements of Trajectory Apex versus Arm regions from nearest NS,**
1304 **THRAP3, or DDX39B foci**
1305 DNA-FISH spots for Trajectory Apex and Arm were detected using the "blob log"
1306 function within the scikit-Image Python package (Van Der Walt et al., 2014) and were
1307 clustered using DBSCAN (Ester et al., 1996). For this clustering, an iterative threshold
1308 estimation method was employed such that the number of clusters per nucleus was 3-4.
1309 For each cluster, the cluster center was calculated and a box of 30x30 pixels (x-y) from
1310 the center was cropped; within this cropped volume, 7 optical sections (z-slices) were
1311 sum intensity projected to create a new 2D image, within which the center of mass of

1312 the Apex signal was calculated. Within the same 2D cropped projection, the Arm region
1313 signal was segmented and the pixels within the segmented region were split into three
1314 categories, for each of which their center-of-mass determined: 1) "Arm-close": 25%
1315 pixels closest to Apex; "Arm-far": 25% pixels farthest from Apex; "Arm-middle";
1316 remaining pixels. The DDX39B or THRAP3 and NS signals were thresholded using the
1317 Otsu function (Otsu, 1979). The shortest Euclidean distance between the center of each
1318 DNA-FISH spot (Apex or Arm) to the nearest edge of the segmented protein/speckle
1319 was measured.
1320

1321 **Distance measurements of E6 and mini-Dystrophin transgene RNAs relative to**
1322 **SON, THRAP3 and DDX39B foci**

1323 Distance measurements for transgene RNAs, tagged with MS2 repeats and
1324 MS2-binding proteins, relative to NS (SON/SRRM2), DDX39B, or THRAP3 foci were
1325 performed similarly to the RNA Poll II foci distance measurements. Nuclear regions
1326 were manually selected, and RNA spots within each nuclear region were identified
1327 using the 'Find Maxima' function, to generate binary images. NS areas were segmented
1328 using the Otsu' thresholding algorithm (Otsu, 1979) which effectively defined
1329 perispeckle and NS boundaries. For this data, plotting and statistical tests were
1330 performed using GraphPad Prism.
1331

1332 **Distance measurement of HSPH1 and HSPA1 RNAs relative to SON, THRAP3, and**
1333 **DDX39B foci**

1334 For HSPH1 and HSPA1 RNA-FISH analysis, images were denoised using the
1335 “despeckle” function in ImageJ and a Gaussian filter of 1 pixel radius applied afterwards
1336 Distance measurements relative to SON, THRAP3 and DDX39B foci were performed
1337 using the ImageJ plugin as described for DNA-FISH measurements of Type I and Type
1338 II SON TSA-seq peaks.
1339 For Mander’s coefficient calculations, we used a maximum-intensity projection of
1340 3 optical sections of the "despeckle" denoised and Gaussian fitered images. A nuclear
1341 mask was generated using the DAPI signal and Otsu thresholding (Otsu, 1979) and
1342 applied to the RNA and protein signals. These nuclear-masked images were then used
1343 for calculating Mander’s coefficient using the JaCoP plugin (Bolte and Cordelières,
1344 2006) in Fiji (Schindelin et al., 2012).
1345
1346 **Plotting and Statistical Analysis**
1347 All plots, unless otherwise stated, were generated using the ggplot2 package in
1348 R version R4.2.2. All analysis of variance (ANOVA) used type 3 comparison using the
1349 “car” package. The options were set as options (contrasts=c (“contr.sum”, “contr.poly”)).
1350 We used a generalized linear model with gamma distribution followed by the Tukey
1351 posthoc test. For RNA Pol II foci and RNA-FISH distance measurements, the Kruskal-
1352 Wallis test followed by the pairwise Wilcoxon test was used to calculate P-values as
1353 indicated in the figures. For Mander’s coefficient comparison, an unpaired t-test was
1354 used in R. All boxplots represent the interquartile range with the upper line indicating
1355 75% and the bottom line indicating 25%. Central line indicates median, and whiskers
1356 represent the range of data shown.

1357 **Figure legends:**

1358 **Figure 1: Screening for potential markers of alternative "gene expression hubs"**

1359 A. TSA-seq SON Type 1 (dark magenta) and Type 2 (dark green) peaks differ in their
1360 association with and average distance from NS. Type 2 peaks represent active genomic
1361 regions, weakly associated with NS, that might instead preferentially interact with an
1362 alternative nuclear active niche (yellow) present in the interchromatin (IC) space.
1363 Contact with this alternative active niche might boost gene expression (right panel).
1364 B. Screening pipeline for the identification of proteins that occupy IC space, illustrated
1365 with THRAP3 as an example candidate protein. (Left) Transient transfection of EGFP-
1366 tagged constructs (gray) in some cases showed varied distributions based on
1367 expression levels (gradient, left), which often accompanied changes in NS morphology.
1368 (Middle) Candidates showing a network-like pattern at low expression levels were
1369 validated by antibody staining of the endogenous protein. (Right) Candidate proteins
1370 were grouped into the same staining pattern if they showed extensive colocalization
1371 throughout the nucleus.
1372 C-D: Perispeckle THRAP3 Pattern (PSTP) (C) and Perispeckle DDX39B Pattern
1373 (PSDP) (D) represent two networks within the IC space that show protein
1374 concentrations in the vicinity of NS but also extend outwards in a network-type pattern.
1375 Insets: Box 1 (yellow borders): string of foci form linear thread-like structures; Box 2
1376 (white borders): thread-like extensions at the nuclear periphery; Box 3 (pink borders):
1377 thread-like extensions connecting nearby NS. PSTP proteins are present at similar
1378 concentration within and outside NS, but PSDP proteins are concentrated inside NS as
1379 compared to the network outside of NS.

1380 E-F: Colocalization of PSTP (E) and PSDP (F) proteins. (E) Immunostaining of BCLAF1
1381 (gray) relative to THRAP3 (magenta) and EGFP-SON (yellow). (F) Immunostaining of
1382 RBM8A (gray) relative to mCherry-DDX39B (green) and EGFP-SON (yellow). Line
1383 profiles along the arrows (shown in merged insets) show overlapping peaks
1384 (arrowheads) of BCLAF1 and THRAP3 (left) or RBM8A and DDX39B (right). Scalebars:
1385 5 μm (main images) and 1 μm (insets).
1386
1387 **Figure 2: Highly dynamic PSTP and PSDP networks appear, disappear, and**
1388 **reappear within the same or nearby IC space**
1389 A and B: Live-cell imaging of endogenously tagged EGFP-THRAP3 (A, Video 1) and
1390 mCherry-DDX39B (B, Video 2) along with SON (gray) over 1 second (s) intervals shows
1391 linear thread-like protein concentrations ("structures") appear and disappear within the
1392 vicinity of NS (see Videos 1 and 2). Time projections over 60 seconds (middle and right
1393 panels) show these thread-like structures more clearly, indicating they consistently recur
1394 within the same spatial locations, with some foci (arrows) showing a relative increase in
1395 brightness, suggesting more stable and/or frequent accumulation of protein at these
1396 regions over time. Scale bar=5 μm. Insets (A' and B') show the dynamics of single
1397 thread-like structures over 1 second intervals. Blue (A') and green (B') boxes show
1398 sequential frames in which thread-like structures form and remain stable over a number
1399 of seconds. These structures then disappear but reform at later times (arrowheads) in
1400 the same region. Sixty second time projection of the same structures are shown
1401 enlarged in insets ((A)and (B), right). Scale bar= 1 μm. THRAP3 and DDX39B
1402 intensities are scaled using a blue-orange LUT (Fiji, blue-orange-icb LUT).

1403 C and D: Endogenously tagged mCherry-THRAP3 (C; magenta, Video 3) and mCherry-
1404 DDX39B (D; magenta, Video 4) networks are stable within the interchromatin (IC) space
1405 over hours (~10-14 hours (h)) in live cells (see Videos 3 and 4). Insets (bottom panels)
1406 show boxed region (top panel, white borders) at multiple time-points. Nuclear speckles
1407 (yellow) form and fuse and/or remain stable (arrowheads) within the vicinity of
1408 perispeckle networks, while thread-like projections of THRAP3 or DDX39B appear,
1409 disappear, and then reappear repeatedly within the same regions (arrows). DNA (cyan)
1410 is visualized by SiR-Hoechst staining. Scale bar= 1 μm.
1411
1412 **Figure 3: PSTP and PSDP subdivide the interchromatin space and respond**
1413 **differently to functional perturbation**
1414 A: Wide-field imaging of immunostained THRAP3 (magenta) and DDX39B (green)
1415 relative to SON (EGFP-SON knock-in; yellow) in U2OS cells shows that the two
1416 perispeckle networks are juxtaposed outside of NS. Insets show enlargements of boxed
1417 regions (rectangles 1,2). Line profile plots (along white arrows within insets) show
1418 THRAP3 and DDX39B peaks are offset from each other. Scale bars- 5 μm main image;
1419 1 μm inset.
1420 B: STORM super-resolution imaging of immunostained THRAP3 (magenta) and
1421 DDX39B (green) demonstrates more clearly the spatial separation of THRAP3 versus
1422 DDX39B concentrations suggested by wide-field microscopy (A). Insets are
1423 enlargements of boxed regions (white rectangles 1, 2) and highlight nuclear regions
1424 showing THRAP3 and DDX39B occupying distinct spaces. Line profile plots (along
1425 yellow or white arrows within inset 1) show peaks of THRAP3 and DDX39B

1426 concentrations separated by distances of ~20-30 nm. Scale bars- 5 μm main image; 1
1427 μm inset.
1428 C-D: Transcriptional inhibition by 5,6-Dichloro-1-β-D-ribofuranosylbenzimidazole (DRB)
1429 treatment disrupts THRAP3 perispeckle pattern (C; magenta) but DDX39B perispeckle
1430 pattern (D; green) remains relatively unchanged. NS (yellow) are marked by SON (C-
1431 top) or SRRM2 (D-bottom). THRAP3 progressively condenses into distinct foci arranged
1432 frequently in thread-like structures and ultimately accumulates in cap-like accumulations
1433 adjacent to NS (Video 5). Scale bars- 5 μm main image; 1 μm inset.
1434 E-F: Box plots showing total skeleton length (E) and number of connections (F) of
1435 THRAP3 and DDX39B networks (SFig. 3A) upon DRB treatment (1, 2 hours (h)) as
1436 compared to DMSO (2 hours). Central line indicates median and square within the
1437 boxplot indicates mean. n (number of nuclei) = 10 for each condition. One-way ANOVA
1438 with Tukey post-hoc test was used to calculate P-values. ns : $P > 0.05$; ** : $P \leq 0.01$; ***:
1439 $P \leq 0.001$.
1440
1441 **Figure 4: RNA pol2 Ser2p foci localize in close proximity to PSTP and PSDP**
1442 A-F: Immunostaining of RNA Pol II serine 2 phosphorylated foci (white) (A-C) and serine
1443 5 phosphorylated foci (white) (D-F): RNA pol II foci (arrowheads) not near NS (SON,
1444 orange; endogenously tagged with EGFP) align adjacent to THRAP3 (magenta;
1445 immunostaining) and DDX39B (green; endogenously tagged with mCherry) foci within
1446 the IC space. RNA Pol II foci at the edge of SON-marked speckles indicated by yellow
1447 circles. Images A-B and D-E (gray boxes) show Pol II foci in the same nucleus relative
1448 to SON and DDX39B.

1449 G-H Distance distribution curves for the percentage of RNA Pol II serine 2
1450 phosphorylated foci (G) and serine 5 phosphorylated foci (H) relative to SON, THRAP3
1451 and DDX39B.
1452 I: Boxplots showing average distance of foci relative to RNA Pol II foci relative to SON,
1453 THRAP3 and DDX39B. Central line indicates median distance and square within the
1454 boxplot indicates mean distance. P-values calculated using Wilcoxson sum rank test; **:
1455 P ≤ 0.01; ****: P ≤ 0.0001. (n=9124-81267 RNAPII foci).
1456
1457 **Figure 5: Gene expression hot-zones interact preferentially with PSTP and PSDP**
1458 **in HCT116 cells**
1459 A: Representative TSA-seq plot for chromosome 2 in HCT116 cells for SON (blue),
1460 DDX39B (green), THRAP3 (magenta), Lamin B1 (black), and Lamin B1 Dam-ID (gray).
1461 Yellow and blue highlights mark Type I peaks and Type II peaks, respectively. Type I
1462 peaks show large magnitude peaks for SON but lower amplitude and broader peaks for
1463 DDX39B and THRAP3. Type II peaks show well-defined and higher magnitude peaks
1464 for DDX39B and THRAP3 as compared to SON.
1465 B: Scatterplots between two SON TSA-seq replicates (orange), SON vs DDX39B
1466 (green) and SON vs THRAP3 (magenta). Overall, TSA-seq scores for DDX39B and
1467 THRAP3 correlate closely with SON. Both DDX39B and THRAP3 versus SON
1468 scatterplots show two regions with distinct slopes: higher for negative SON scores
1469 (black dotted line) but lower for positive SON scores (white dotted line).
1470 C: DNA-FISH (yellow) in HCT116 cells for multiple Type I and Type II peaks (apex)
1471 shows higher frequency of association with NS (SON-cyan or SRRM2-blue) for Type I

versus Type II peaks. NS non-associated alleles show close proximity or locate adjacent to THRAP3 (magenta) or DDX39B (green) foci/accumulations. Regions highlighted in white boxes are shown on the right as insets. Scale bars- 5 μm main image; 1 μm inset.

D: Violin plots showing distance of DNA-FISH spots relative to SON, DDX39B and THRAP3 foci/accumulations. Central line indicates median distance and white square within the boxplot indicates mean distance. (n (alleles) as indicated: 67 (Type I) and 95 (Type II) SON; 114 (Type I) and 103 (Type II) DDX39B; 105 (Type I) and 96 (Type II) THRAP3). One-way ANOVA with Tukey post-hoc test was used to calculate P-values. ns : $P > 0.05$; *** : $P \leq 0.001$; **** : $P \leq 0.0001$.

E-G: Probability density plots for distance distribution of DNA-FISH spots relative to SON (E), DDX39B (F) and THRAP3 (G) foci/accumulations for Type I (yellow) and Type II (blue) peaks. (n (alleles) as indicated: 67 (Type I) and 95 (Type II) SON; 114 (Type I) and 103 (Type II) DDX39B; 105 (Type I) and 96 (Type II) THRAP3).

Figure 6: Mapping of chromosome trajectory- SON TSA-seq peak to nearest LAD- shows alignment along PSTP and PSDP foci / concentrations

(A-B) Left, top panels: Browser views showing SON, DDX39B, THRAP3, Lamin B1 TSA-seq and Lamin B1 DamID tracks corresponding to one Type I (A) or Type 2 (B) SON TSA-seq peak-to-valley chromosome trajectories mapped by DNA FISH. Highlights show locations of peak "Apex" (yellow) and multiple "Arm" (grey) DNA FISH probes.

1494 (A-B) Right: Sum-intensity projections of Type I (A) or Type II (B) Apex versus Arm
1495 probes along peak-to-valley chromosome trajectories and their spatial positioning
1496 relative to THRAP3 (magenta), DDX39B (green), and nuclear speckles (SON/SRRM2;
1497 blue) immunostaining. The percentage of DNA trajectories appearing aligned with
1498 perispeckle staining is higher for DDX39B versus THRAP3. Scalebar=1 μm.
1499 (A-B) Left, bottom panels: Statistics for Apex versus Arm chromosome orientation
1500 relative to foci of SON, THRAP3, and DDX39B summarized in box plots. Apex FISH
1501 signals are statistically significantly closer to SON, THRAP3, and DDX39B foci than to
1502 middle and distal Arm FISH signals for the Type I trajectory. Apex FISH signals are
1503 closer to middle and statistically significantly closer to distal Arm signals relative to
1504 THRAP3 foci, but not SON or DDX39B foci, consistent with the distal positioning of
1505 Type II trajectories relative to NS and the higher trajectory alignment seen relative to the
1506 DDX39B versus THRAP3 staining. Black squares represent mean distances and central
1507 line represents median distances. n (number of trajectories analyzed): Type I trajectory:
1508 THRAP3/SON = 40; DDX39B/SRRM2= 66; Type II trajectory: THRAP3/SON=82;
1509 DDX39B/SRRM2=54. Kruskal-Wallis test followed by Dunn's post-hoc test was used to
1510 calculate P-values. ns : $P > 0.05$; * : $P \leq 0.05$; ** : $P \leq 0.01$; *** : $P \leq 0.001$; **** : $P \leq$
1511 0.0001.
1512

1513 **Figure 7: RNA from intron-containing and intronless genes associate**
1514 **differentially with PSTP and PSDP**

1515 A-B: RNAs (yellow) produced by the transgene array expressing the "E6" (6 exons)
1516 construct with βeta-globin sequences (A) localize more closely to THRAP3 foci /

1517 concentrations (magenta) than RNAs produced by the transgene array expressing the
1518 "mini-Dystrophin" (B) construct with a single exon (no introns). SON (NS) is cyan. Both
1519 RNAs are tagged with MS2 repeats and visualized by expression of the MS2-coat
1520 protein fused with YFP.
1521 (C-D) RNAs produced by both the E6 (C) and mini-Dystrophin (D) constructs localize
1522 closely with DDX39B (green) foci / concentrations. SRMM2 (NS) is blue.
1523 (E-F) FISH signals (yellow) for RNAs produced by the endogenous HSPH1 gene with
1524 many introns (E) localize closer to THRAP3 foci / concentrations (magenta) than RNAs
1525 produced by the endogenous HSPA1A and HSPA1B genes with no introns (F). SON
1526 (NS) is cyan.
1527 (G-H) FISH signals (magenta) for RNAs produced by the endogenous HSPH1 gene
1528 with many introns (E) and the endogenous HSPA1A and HSPA1B genes with no introns
1529 (H) both localize close to DDX39B (green) SRRM2 (NS) is blue.
1530 I: Box-plots of distances of β-globin E6 and mini-Dystrophin RNAs relative to SON,
1531 THRAP3, SRRM2 and DDX39B. n (number of RNPs per sample)= 1212-2627. Kruskal-
1532 Wallis test followed by Dunn's multiple comparisons test was used to calculate P-
1533 values. ns : P > 0.05; * : P ≤ 0.05; ** : P ≤ 0.01; *** : P ≤ 0.001; **** : P ≤ 0.0001.
1534 J: Box plots of distances of HSPH1 and HSPA1 RNA relative to SON, THRAP3 and
1535 DDX39B. n (RNA spots) = 168-257. RNPs from 5-8 nuclei used for this analysis.
1536 Kruskal-Wallis test followed by pairwise Wilcoxon test was used to calculate P-values.
1537 ns : P > 0.05; * : P ≤ 0.05; ** : P ≤ 0.01; *** : P ≤ 0.001; **** : P ≤ 0.0001.
1538 K: Box plots showing average fraction overlap (Manders coefficient) between RNA
1539 signals and THRAP3 or DDX39B foci / concentrations for HSPH1 and HSPA1 RNAs.

1540 White squares represent mean and central line represents median. (n (number of
1541 nuclei): HSPH1 18; HSPA1 18). Kruskal-Wallis test followed by pairwise Wilcoxon test
1542 was used to calculate P-values. ns : P > 0.05; * : P ≤ 0.05; ** : P ≤ 0.01; *** : P ≤ 0.001;
1543 **** : P ≤ 0.0001.
1544 (A-D) Scale bar=1 μm. (E-H) Scale bar= 5 μm main image; 1 μm inset.
1545 (A-H) Regions highlighted within white boxes are shown as insets on the right.\
1546
1547 **Figure 8: Perispeckle networks and genome positioning are largely maintained**
1548 **after NS depletion but NS-proximal genes are downregulated**
1549 A: SON (mClover, green) and SRRM2 (mCherry, magenta) intensities (y-axis) as a
1550 function of time (x-axis, hours) after 5-Ph-IAA treatment as measured by flow cytometry
1551 reveals maximum double knockdown after ~ 4 hours in these HCT116 cells.
1552 B: Live-cell imaging reveals DDX39B distribution shows minimal changes during
1553 process of NS elimination (Video 6). Left: Pseudocolor intensity mapping of mClover-
1554 SON (endogenous gene expression, top panels) versus HaloTag-DDX39B (transiently
1555 expressed, bottom panels) at 20 (left) versus 65 (right) minutes after 5-Ph-IAA induced
1556 double knockdown (DKD) of SON and SRRM2. Right: Inset frames show SON (top) or
1557 DDX39B (bottom) over a single NS region at different times (minutes, m) after DKD.
1558 Percentages of SON (top) or DDX39B (bottom) remaining over NS region relative to the
1559 first frame intensities are shown as white numbers (bottom right, each frame).
1560 Scale bar- 5 μm main image; 1 μm inset.

1561 C: Immunostaining of DDX39B (cyan) and THRAP3 (magenta) without (top panel) or
1562 with 5-Ph-IAA treatment for 4 hours (bottom panel). SON (yellow) and SRRM2 (gray)
1563 marked NS undergo degradation within 4 hours.
1564 D: Loss of nuclear poly-A RNA concentrations within NS occurs after NS elimination by
1565 DKD (5-Ph-IAA treatment). Nucleus (upper left) with significant SON (green) and
1566 SRRM2 (magenta) still remaining in NS also still shows poly-A (middle panel, grey; right
1567 panel, yellow) FISH signal accumulations within NS; dispersal of poly-A accumulation is
1568 seen in two nuclei (right) with greater SON and SRRM2 DKD.
1569 E: DDX39B (green) and THRAP3 (magenta) TSA-seq profiles of chromosome 2 in
1570 HCT116 cells engineered with AID2-inducible degron tagged SON and SRRM2 alleles
1571 after DMSO (dark colors) versus 5-Ph-IAA (light colors) treatment for 4 hours. SON
1572 TSA-seq (black) from WT cells is shown in comparison. Type I (yellow highlights) and
1573 Type II (blue highlights) peaks show little or no change in DDX39B and THRAP3 peak
1574 amplitudes after DKD.
1575 F-H. Differentially expressed genes (DEG) near SON TSA-seq Type 1 peaks show a
1576 strong bias towards downregulation. In contrast, DEG near SON TSA-seq Type 2
1577 peaks show bias towards upregulation, particularly for SON TSA-seq peak amplitudes
1578 less than or equal to zero.
1579 F: Volcano plot showing log2 fold expression changes versus log10 (False Discovery
1580 Rate) for DEG present +/- 500 kb from SON TSA-seq Type I (yellow) and Type II (blue)
1581 peaks in HCT116 cells after 5-Ph-IAA-induced SON-SRRM2 degradation.
1582 G: Scatterplot showing mean SON TSA-seq score versus log2 fold changes for DEG
1583 present +/- 500 kb of Type I (yellow) and Type II (blue) peaks. Numbers of DEG flanking

1584 Type II peaks with SON TSA-seq peak amplitudes less than or equal to zero (left of
1585 grey dashed vertical line) are indicated in blue.
1586 H: Density plot with log2 fold change of upregulated and downregulated genes within
1587 Type I and Type II regions. Type I: 162 upregulated genes and 897 downregulated
1588 genes; Type II: 192 upregulated genes and 144 downregulated genes.
1589
1590 **Figure 9: Model showing organization of genes relative to NS and DDX39B (PSDP)**
1591 **and THRAP3 (PDTP) perispeckle patterns**
1592 A: We propose NS versus perispeckle patterns correspond to two different nuclear
1593 niches acting as gene expression "hubs" for two different sets of genes. These sets of
1594 genes are contained within chromosomal regions with similarly elevated levels of gene
1595 expression but differential localization relative to NS. Genes near SON TSA-seq Type I
1596 peaks (Type I gene expression hot-zones) associate closely with NS (blue). Genes
1597 near SON TSA-seq Type II peaks (Type II gene expression hot-zones) mostly locate
1598 away from NS but near perispeckle patterns marked by THRAP3 (magenta, PSTP) and
1599 DDX39B (green, PSDP). Transcripts from intron-rich genes (yellow) associate with
1600 PSTP and PSDP while transcripts from intronless genes (red) associate only with
1601 PSDP.
1602 B: After NS depletion, genome organization relative to PSTP and PSDP remains largely
1603 the same, although many of the Type I set of genes are downregulated in the absence
1604 of NS, suggesting that NS confer added gene expression amplification for this set of
1605 genes.

1606 C: We imagine that positive regulation of gene expression may result from one set of
1607 genes associating with NS and the other set of genes associating with perispeckle
1608 patterns. Previous observations of gene movements from the nuclear lamina towards
1609 the nuclear interior and/or towards NS would suggest this occurs, at least in some
1610 cases, through genes moving towards either of these two hubs (top), but this might also
1611 occur through NS and/or perispeckle patterns moving or extending towards genes
1612 (middle), nucleating near genes (not shown), or a combination of gene and hub
1613 movements towards each other (bottom).
1614

1615

1616 **Supplementary Figure Legends:**

1617 **Supplementary Figure 1: Screening for proteins exhibiting perispeckle patterns**

1618 A: Representative protein candidates showing different categories of distributions within
1619 the interchromatin space (ICS). (Left to right) SRRM2: NS-enriched protein with no
1620 extended staining network in ICS; DDX39B: NS-enriched protein with additional
1621 extended staining network in ICS; protein concentration is highest within NS and lower
1622 in ICS network than within NS; THRAP3: protein concentrations are similar in and/or
1623 surrounding NS as the extended staining network in ICS; EIF4A3: protein concentration
1624 is present within NS but protein has a diffuse distribution, rather than a network-like
1625 staining pattern, within ICS; SAF-B: protein is largely absent within NS but shows an
1626 extended staining network not obviously correlated with NS within ICS. Each protein
1627 distribution is shown in grey (top row) and relative to NS (SON or SRRM2, magenta)
1628 (top 2 rows; scalebar: 5 μm). Regions highlighted within the whole nuclear images
1629 magnified to show protein distribution (grey) relative to NS (magenta; 3rd and 4th rows;
1630 scalebar: 1 μm). Pseudo-color images show the protein distribution segmented into
1631 "protein within NS" and "protein outside NS" fractions. Intensity plots (bottom row) show
1632 protein intensities over every percentile for "protein within NS" (blue) and "protein
1633 outside NS" (orange) fractions.

1634 B: Plot showing fraction of total protein intensity found outside NS. (n (number of nuclei)
1635 =3). Each point represents mean± standard deviation (SD).

1636 C: Plot showing fraction of nuclear area occupied by protein distribution outside NS (n
1637 (number of nuclei)=3). Each point represents mean±SD.

1638 D: Representative images of protein distributions all candidates surveyed in the
1639 screening ordered based on fraction of protein staining outside of NS (low to high).
1640 Pseudocolor intensity-mapped images (middle and right panels) highlight the lower
1641 intensity protein distributions seen within the ICS.
1642 E: Protein distributions segmented into “Protein within NS” and “Protein outside NS”
1643 intensity-mapped images for each candidate.
1644 F: PLRG1 colocalizes with THRAP3 in staining network outside of NS but is enriched
1645 within NS: Immunostaining of PLRG1(gray) along with endogenously tagged mCh-
1646 THRAP3 (magenta) U2OS cells. (Main image-scalebar: 5 μm; inset- scalebar: 1 μm).
1647 G: Cells expressing lentiviral mediated mCherry MAGOH (gray) immunostained with
1648 DDX39B (green) show colocalization of both proteins within ICS. (Main image-scalebar:
1649 5 μm; inset- scalebar: 1 μm).
1650 H: RNA FISH (using oligonucleotide probes) distribution for MALAT1 (grey) relative to
1651 THRAP3 (magenta) and DDX39B (green) immunostaining within the ICS. Second and
1652 fourth rows represent enlargements of boxed regions (white borders) from first and third
1653 rows, respectively. Apart from NS-enriched MALAT1, diffraction-limited spots of
1654 MALAT-1 are seen in the ICS in the vicinity of NS and show close spatial relationship to
1655 THRAP3 and DDX39B foci. Box plot showing fraction of RNA signal outside NS
1656 overlapping with THRAP3 or DDX39B signals. (n (number of nuclei) =10 for each
1657 comparison). White square represents mean and central line represents median value.
1658 **Supplementary Figure 3: Transcriptional inhibition causes changes in perispeckle**
1659 **network PSTP.**

1660 A-B: Disruption of THRAP3 (magenta) network upon transcriptional inhibition also seen
1661 with Triptolide (A) and α-amanitin (B) treatments. NS marked by SON in yellow. The
1662 extent of disruption of the THRAP3 pattern after 2 hours of Triptolide and α-amanitin
1663 treatment resembles the disruption observed with 1 hour DRB treatment.
1664 C: Intensity-mapped images of THRAP3 (1st column) and DDX39B (3rd column) and
1665 their corresponding skeletons (2nd and 4th columns) upon treatment with 5,6-Dichloro-
1666 1-β-D-ribofuranosylbenzimidazole (DRB) comparing changes with DMSO control versus
1667 1 and 2 hours (h) of treatment.
1668 D: Multiple members of PSTP colocalize even as the networks are disrupted.
1669 Comparison of BCLAF1 (immunostaining, grey) and EGFP-THRAP3 (endogenous gene
1670 tagged, magenta) networks shows colocalization of BCLAF1 and THRAP3 as they are
1671 both disrupted upon DRB treatment (2 hours (h)). NS are marked by HaloTag-SON
1672 (endogenous gene tagged, yellow). Scale bar- 5 μm main image; 1 μm inset.
1673 E-F: Intensity mapped images and their corresponding skeletons of BCLAF1 (PSTP
1674 member) and RBM8A (PSDP member) upon DRB treatment as compared to DMSO
1675 shows similar disruption of PSTP network versus maintenance of PSDP network using
1676 staining against other PSTP (BCLAF1) and PSDP (RBM8A) components.
1677 G. Boxplot showing total skeleton length (in pixels) of BCLAF1 (left) and RBM8A (right)
1678 with DMSO or DRB treatment for 2 hours. n (number of nuclei) = 10-13 for each
1679 condition. One-way ANOVA with Tukey post-hoc test was used to calculate P-values.
1680 ns : $P > 0.05$; * : $P \leq 0.05$; ** : $P \leq 0.01$; *** : $P \leq 0.001$; **** : $P \leq 0.0001$.
1681

1682 **Supplementary Figure 4: RNA Polymerase II foci associate closely with PSTP as**
1683 **compared to PSDP**
1684 A-B: Representative images of RNA Pol II foci (Ser5p top rows, Ser2- bottom rows)
1685 detected for distance measurements from THRAP3 (magenta, A) and DDX39B
1686 (magenta, B) and SON (green, B). Shown alongside are line profile plots of RNA Pol II
1687 foci relative to the three compartments. RNA Pol II foci appear to frequently localize
1688 adjacent to or overlapping with staining concentrations of THRAP3 and DDX39B, as
1689 seen by offset of their peaks with RNA pol II foci. Images on the right show segmented
1690 THRAP3 (top) and DDX39B (bottom) networks used for distance measurements of RNA
1691 Pol II foci. Circled foci colored based on distance: Red: <0.15 μm; Blue: >0.15 μm and
1692 <0.45 μm; Yellow: ≥0.45μm.
1693
1694 **Supplementary Figure 5: TSA-seq reveals gene expression hot-zones**
1695 **preferentially associate with PSTP and PSDP also in U2OS cells**
1696 A: Representative TSA-seq and Lamin B1 DamID tracks for chromosome 2 in U2OS
1697 cells: SON (blue), DDX39B (green), THRAP3 (magenta) and Lamin B1 DamID (grey).
1698 Yellow highlights mark Type I peaks and blue highlights mark Type II peaks.
1699 B: Heat map showing Pearson's correlation coefficients for SON, THRAP3 and DDX39B
1700 TSA-seq datasets (mean of two replicates) in U2OS cells.
1701 C: DNA-FISH (yellow) for Type I and Type II peaks (Apex) relative to SON (cyan) and
1702 THRAP3 (magenta) or DDX39B (green) and SRRM2 (blue). Type I regions are NS-
1703 associated and remain in contact with THRAP3 and DDX39B. Type II regions that are
1704 away from a NS are also in contact or close proximity of THRAP3 or DDX39B

1705 accumulations. Regions highlighted in white boxes are shown on the right as insets.
1706 Scale bars- 5 μm main image; 1 μm inset.
1707 D: Violin plots showing distance of DNA-FISH spots relative to SON, DDX39B and
1708 THRAP3 in U2OS cells. Central line indicates median distance and white square within
1709 the boxplot indicates mean distance. (n (alleles) as indicated: 126 (Type I) and 104
1710 (Type II) SON; 130 (Type I) and 106 (Type II) DDX39B; 126 (Type I) and 104 (Type II)
1711 THRAP3). One-way ANOVA with Tukey post-hoc test was used to calculate P-values.
1712 ns : $P > 0.05$; *** : $P \leq 0.001$; **** : $P \leq 0.0001$.
1713 E-G: Probability density plots for distance distribution of DNA-FISH spots relative to
1714 SON (E), DDX39B (F) and THRAP3 (G) for Type I (yellow) and Type II (blue) peaks in
1715 U2OS cells. (n (alleles) as indicated: 126 (Type I) and 104 (Type II) SON; 130 (Type I)
1716 and 106 (Type II) DDX39B; 126 (Type I) and 104 (Type II) THRAP3).
1717
1718 **Supplementary Figure 8: NS knockdown does not alter spatial positioning of**
1719 **genome relative to DDX39B and THRAP3 in HCT116 cells**
1720 A: Representative images showing mClover-SON (green) and SRRM2-mCherry
1721 (magenta) fluorescence intensities change over time with 5-Ph-IAA treatment for 0 min,
1722 2 hours or 4 hours.
1723 B: Heat map showing Pearson's correlation coefficients across WT HCT116 (SON,
1724 THRAP3, DDX39B) and HCT116 SON-SRRM2 degron cells (DMSO THRAP3, 5-Ph-
1725 IAA THRAP3, DMSO DDX39B, 5-Ph-IAA DDX39B) TSA-seq datasets.
1726 C: TSA-seq score tracks for chromosome 2 in HCT116 SON-SRRM2 degron cells: SON
1727 (TSA-seq score from WT cells; black shown for comparison) Type I (yellow highlights)

1728 and Type II Peaks (blue highlights). Normalized TSA-seq scores between DMSO-
1729 treated and 5-Ph-IAA-treated cells show small changes all over the entire chromosome
1730 for THRAP3 (magenta; negative residual; P-value in grey significant) and DDX39B
1731 (green; positive residual; P-value in grey not significant). P-value threshold set at log10
1732 scale at 2 (red line).
1733 D: Ideogram plots of all chromosomes in percentile change (DMSO-treated minus 5-Ph-
1734 IAA treated) in TSA-seq scores in HCT116 SON-SRRM2 degron cells for DDX39B (left)
1735 and THRAP3 (right) show little or no changes (-5 to +5 green) except for very few bins
1736 showing higher changes (indigo -20 / yellow +20).
1737 E: Scatterplots between mean TSA-seq scores of DMSO-treated and 5-Ph-IAA-treated
1738 DDX39B (green) and THRAP3 (magenta) show similar correlation coefficient as two
1739 individual replicates of DMSO-treated DDX39B (blue) and THRAP3 (yellow) TSA-seq.
1740
1741 **Supplementary Information**
1742 Supplementary Table 1: Reagent information (Primers, antibodies, oligolibraries and
1743 related information).
1744 1. cDNA constructs generated for screening: Primer sequences used for PCR
1745 amplification and restriction enzymes used for cloning
1746 2. Antibodies: Details and dilutions used
1747 3. CRISPR-Cas9 mediated gene tagging: Target specific gRNA sequences,
1748 homology arm sequences for Donor template generation and genotyping primers
1749 used.

4. Selected Type I and Type II genomic regions for FISH validation of TSA-seq in HCT116 and U2OS cells
5. Oligolibrary DNA-FISH probe sequences for 7 Type I peaks
6. Oligolibrary DNA-FISH probe sequences for 8 Type II peaks
7. Genomic coordinates of selected regions of Trajectory FISH of TypeI peak to nearest LAD or Type II peak to nearest LAD region
8. Oligolibrary DNA-FISH probe sequences for Apex of Type I peak
9. Oligolibrary DNA-FISH probe sequences for Arm regions of Type I trajectory
10. Oligolibrary DNA-FISH probe sequences for Apex of Type II peak
11. Oligolibrary DNA-FISH probe sequences for Arm regions of Type II trajectory
12. Human MALAT1 oligolibrary RNA-FISH probe sequences
13. Human MALAT1 Stellaris RNA-FISH probe sequences
14. 4DN Data Portal Accession numbers of TSA-seq datasets generated for this study.
15. 4DN Data Portal Accession numbers of RNA-seq generated for this study.

Supplementary Table 2: Complete list of significantly affected genes after nuclear speckle knockdown

Supplementary Videos

Video 1: Rapid dynamics of THRAP3 network in U2OS

A video of EGFP-THRAP3 (left, green) and its corresponding intensity mapping (right) in live U2OS cells showing THRAP3 non-diffuse accumulations forming, disappearing and

1773 reforming in the same space within tens of seconds. Images are acquired at 1 second
1774 intervals. Video is displayed at 5 frames per second. NS are marked by HaloTag-SON
1775 (left, magenta).
1776
1777 **Video 2: Dynamics of DDX39B network in U2OS cells**
1778 A representative video of mCherry-DDX39B (left, green) and its corresponding intensity
1779 mapping (right) in live U2OS cells showing connections of DDX39B forming and
1780 disappearing in the vicinity of NS marked by EGFP-SON (left, magenta). Images are
1781 acquired at 1 second intervals. (Gamma 0.8 used to display DDX39B). Video is
1782 displayed at 5 frames per second.
1783
1784 **Video 3: Perispeckle THRAP3 network remains stable over many hours within the**
1785 **interchromatin space**
1786 A video of mCherry-THRAP3 (magenta), EGFP-SON (yellow) and SiR-Hoechst DNA
1787 (cyan) imaged over 16 hours (h) at 40-minute intervals. THRAP3 network is dynamic
1788 but remains overall stable over time within the interchromatin space.
1789
1790 **Video 4: Perispeckle DDX39B network within the interchromatin space remains**
1791 **stable over many hours**
1792 A video of mCherry-DDX39B (magenta), EGFP-SON (yellow) and SiR-Hoechst DNA
1793 (cyan) imaged over 13 hours (h) at 10-minute intervals. DDX39B connections fluctuate
1794 but reappear within the same space over time making the overall network highly stable.
1795

1796 **Video 5: Transcriptional inhibition by 5,6-Dichloro-1-β-D**
1797 **ribofuranosylbenzimidazole (DRB) causes gradual disruption of THRAP3 network**
1798 A video of EGFP-THRAP3 (left, green) and HaloTag-SON (left, red) along with intensity
1799 mapping of THRAP3 (right) shows the network of THRAP3 collapses into nuclear
1800 speckles over the course of DRB treatment. Imaging was started 10 minutes (min) after
1801 adding DRB and images were taken every 2 minutes for up to 2 hours.
1802
1803 **Video 6: Live imaging of DDX39B upon nuclear speckle knockdown**
1804 Live-cell imaging of transiently expressed HaloTag-DDX39B (green, center) along with
1805 intensity mapping (right) and mClover-SON (in magenta, left) and SRRM2-mCherry in
1806 HCT116 cells shows DDX39B network is maintained even after double knockdown of
1807 SON and SRRM2 and complete loss of nuclear speckles. DDX39B also shows minimal
1808 changes to “speckle-like” structures corresponding to the concentration of DDX39B in
1809 regions originally occupied by the NS identified by SON and SRRM2 concentrations.
1810 Images were taken every 5 minutes (min) beginning 20 minutes after start of 5-Ph-IAA
1811 treatment.
1812
1813 **Data Availability**
1814 All the raw image data are available upon request. All TSA-seq and RNA-Seq datasets
1815 (raw and processed files) generated in this study are available at the 4DN Data Portal
1816 (see Supplementary Table 1 for ID numbers) and the GEO (GSE304818)
1817
1818 **Code Availability**

All custom scripts generated for this study are available on Github (https://github.com/nehacv93/PerispecklePatterns_partitionICS).

Author Contributions:

N.C.V. and A.S.B. conceived of and designed the study; N.C.V. performed most experiments and analyzed data including the screening, fixed-cell imaging, TSA-seq, oligo library design and DNA-FISH. N.C.V. and S.M. performed short timescale live-cell imaging of networks and DRB treatments. J.K. performed long term live-cell imaging, STORM and image analysis for the Pol II distribution and reporter transgene RNP distances relative to the networks. G.F. performed experiments of E6 and mini-Dys transgene RNPs and STED imaging. S.M. and N.C.V. replicated the transgene data set and also performed RNA-FISH for endogenous genes. Endogenous RNA-distance measurements were by N.C.V. and S.M. performed Mander's coefficient analysis. A.B. and M.K. generated and validated the SON-SRRM2 degron cell line. G.H., N.C.V., J.K. and S.M. made the endogenous fluorescent tagged cell lines by CRISPR-Cas9. P.C. performed FACS analysis of degron cell line and RNA-Seq analysis. N.C.V. performed TSA-seq and RNA-Seq correlation analyses. J.D. helped design and supervised the initial implementation of primary screen. K.Y.H. and Y.S.T provided reagents and supervision. N.C.V. and A.S.B. wrote the manuscript with inputs from other authors.

Acknowledgements:

This work was supported by the National Institutes of Health Common Fund 4D Nucleome Program grant U01DK127422 (ASB, KYH, YS) and also NIH R01GM058460

(ASB) and JSPS KAKENHI JP23H04925 and JP25H00979 (MTK) grants. We acknowledge assistance provided by the DNA Services, Roy J. Carver Biotechnology Center, University of Illinois at Urbana-Champaign for quality control on TSA-seq libraries, RNA-seq library construction, and sequencing (TSA-Seq and RNA-Seq libraries). Custom RNA-Seq scripts for processing and analysis of data were provided by the High-Performance Computing in Biology group (HPCBio), Roy J. Carver Biotechnology Center, University of Illinois at Urbana-Champaign. We thank Ratna Karatgi for advice regarding statistical analysis and Mishal Assif for assistance with image analysis.

REFERENCES:

Ahn, E.-Y., R.C. DeKelver, M.-C. Lo, T.A. Nguyen, S. Matsuura, A. Boyapati, S. Pandit, X.-D. Fu, and D.-E. Zhang. 2011. SON Controls Cell-Cycle Progression by Coordinated Regulation of RNA Splicing. *Mol. Cell*. 42:185–198. doi:10.1016/j.molcel.2011.03.014.

Ajuh, P. 2000. Functional analysis of the human CDC5L complex and identification of its components by mass spectrometry. *EMBO J.* 19:6569–6581. doi:10.1093/emboj/19.23.6569.

Alexander, K.A., A. Cote, S.C. Nguyen, L. Zhang, O. Gholamalamdari, P. Agudelo-Garcia, E. Lin-Shiao, K.M.A. Tanim, J. Lim, N. Biddle, M.C. Dunagin, C.R. Good, M.R. Mendoza, S.C. Little, A. Belmont, E.F. Joyce, A. Raj, and S.L. Berger. 2021. p53 mediates target gene association with nuclear speckles for amplified RNA expression. *Mol Cell*. 81:1666-1681 e6. doi:10.1016/j.molcel.2021.03.006.

Arun, G., D. Aggarwal, and D.L. Spector. 2020. MALAT1 Long Non-Coding RNA: Functional Implications. *Non-Coding RNA*. 6:22. doi:10.3390/ncrna6020022.

Barutcu, A.R., M. Wu, U. Braunschweig, B.J.A. Dyakov, Z. Luo, K.M. Turner, T. Durbic, Z.-Y. Lin, R.J. Weatheritt, P.G. Maass, A.-C. Gingras, and B.J. Blencowe. 2022. Systematic mapping of nuclear domain-associated transcripts reveals speckles and lamina as hubs of functionally distinct retained introns. *Mol. Cell*. 82:1035-1052.e9. doi:10.1016/j.molcel.2021.12.010.

Bates, M., B. Huang, G.T. Dempsey, and X. Zhuang. 2007. Multicolor Super-Resolution Imaging with Photo-Switchable Fluorescent Probes. *Science*. 317:1749–1753. doi:10.1126/science.1146598.

Bates, M., S.A. Jones, and X. Zhuang. 2013. Preparation of Photoswitchable Labeled Antibodies for STORM Imaging. *Cold Spring Harb. Protoc.* 2013:pdb.prot075168. doi:10.1101/pdb.prot075168.

Beliveau, B.J., A.N. Boettiger, G. Nir, B. Bintu, P. Yin, X. Zhuang, and C.-T. Wu. 2017. In Situ Super-Resolution Imaging of Genomic DNA with OligoSTORM and OligoDNA-PAINT. *Methods Mol. Biol. Clifton NJ*. 1663:231–252. doi:10.1007/978-1-4939-7265-4_19.

Beliveau, B.J., E.F. Joyce, N. Apostolopoulos, F. Yilmaz, C.Y. Fonseka, R.B. McCole, Y. Chang, J.B. Li, T.N. Senaratne, B.R. Williams, J.-M. Rouillard, and C. Wu. 2012. Versatile design and synthesis platform for visualizing genomes with Oligopaint FISH probes. *Proc. Natl. Acad. Sci.* 109:21301–21306. doi:10.1073/pnas.1213818110.

1885 Bensaude, O. 2011. Inhibiting eukaryotic transcription. Which compound to choose? How
1886 to evaluate its activity?: Which compound to choose? How to evaluate its activity?
1887 *Transcription*. 2:103–108. doi:10.4161/trns.2.3.16172.

1888 Bhat, P., A. Chow, B. Emert, O. Ettlin, S.A. Quinodoz, M. Strehle, Y. Takei, A. Burr, I.N.
1889 Goronzy, A.W. Chen, W. Huang, J.L.M. Ferrer, E. Soehalim, S.-T. Goh, T. Chari, D.K.
1890 Sullivan, M.R. Blanco, and M. Guttman. 2024. Genome organization around nuclear
1891 speckles drives mRNA splicing efficiency. *Nature*. 629:1165–1173.
1892 doi:10.1038/s41586-024-07429-6.

1893 Björkman, A., S.L. Johansen, L. Lin, M. Schertzer, D.C. Kanellis, A.-M. Katsori, S.T.
1894 Christensen, Y. Luo, J.S. Andersen, S.J. Elsässer, A. Londono-Vallejo, J. Bartek, and
1895 K.B. Schou. 2020. Human RTEL1 associates with Poldip3 to facilitate responses to
1896 replication stress and R-loop resolution. *Genes Dev.* 34:1065–1074.
1897 doi:10.1101/gad.330050.119.

1898 Bolte, S., and F.P. Cordelières. 2006. A guided tour into subcellular colocalization analysis
1899 in light microscopy. *J. Microsc.* 224:213–232. doi:10.1111/j.1365-
1900 2818.2006.01706.x.

1901 Bradley, D., and G. Roth. 2007. Adaptive Thresholding using the Integral Image. *J. Graph.*
1902 *Tools*. 12:13–21. doi:10.1080/2151237X.2007.10129236.

1903 Brody, Y., N. Neufeld, N. Bieberstein, S.Z. Causse, E.-M. Böhnlein, K.M. Neugebauer, X.
1904 Darzacq, and Y. Shav-Tal. 2011. The In Vivo Kinetics of RNA Polymerase II Elongation
1905 during Co-Transcriptional Splicing. *PLoS Biol.* 9:e1000573.
1906 doi:10.1371/journal.pbio.1000573.

1907 Carter, K.C., D. Bowman, W. Carrington, K. Fogarty, J.A. McNeil, F.S. Fay, and J.B. Lawrence.
1908 1993. A Three-Dimensional View of Precursor Messenger RNA Metabolism Within
1909 the Mammalian Nucleus. *Science*. 259:1330–1335. doi:10.1126/science.8446902.

1910 Carter, K.C., K.L. Taneja, and J.B. Lawrence. 1991. Discrete nuclear domains of poly(A) RNA
1911 and their relationship to the functional organization of the nucleus. *J. Cell Biol.*
1912 115:1191–1202. doi:10.1083/jcb.115.5.1191.

1913 Chaturvedi, P., and A.S. Belmont. 2024. Nuclear speckle biology: At the cross-roads of
1914 discovery and functional analysis. *Curr. Opin. Cell Biol.* 91:102438.
1915 doi:10.1016/j.ceb.2024.102438.

1916 Chen, Y., and A.S. Belmont. 2019. Genome organization around nuclear speckles. *Curr.*
1917 *Opin. Genet. Dev.* 55:91–99. doi:10.1016/j.gde.2019.06.008.

1918 Chen, Y., Y. Zhang, Y. Wang, L. Zhang, E.K. Brinkman, S.A. Adam, R. Goldman, B. Van
1919 Steensel, J. Ma, and A.S. Belmont. 2018. Mapping 3D genome organization relative

1920 to nuclear compartments using TSA-Seq as a cytological ruler. *J. Cell Biol*.
1921 217:4025–4048. doi:10.1083/jcb.201807108.

1922 Choi, H., M. Kang, K.-H. Lee, and Y.-S. Kim. 2023. Elevated level of PLRG1 is critical for the
1923 proliferation and maintenance of genome stability of tumor cells. *BMB Rep*. 56:612–
1924 617. doi:10.5483/BMBRep.2023-0162.

1925 Chuang, T.-W., C.-C. Lu, C.-H. Su, P.-Y. Wu, S. Easwvaran, C.-C. Lee, H.-C. Kuo, K.-Y. Hung,
1926 K.-M. Lee, C.-Y. Tsai, and W.-Y. Tarn. 2019. The RNA Processing Factor Y14
1927 Participates in DNA Damage Response and Repair. *iScience*. 13:402–415.
1928 doi:10.1016/j.isci.2019.03.005.

1929 Chubb, J.R., S. Boyle, P. Perry, and W.A. Bickmore. 2002. Chromatin motion is constrained
1930 by association with nuclear compartments in human cells. *Curr Biol*. 12:439–45.

1931 Dias, A.P., K. Dufu, H. Lei, and R. Reed. 2010. A role for TREX components in the release of
1932 spliced mRNA from nuclear speckle domains. *Nat. Commun*. 1:97.
1933 doi:10.1038/ncomms1103.

1934 Dobin, A., C.A. Davis, F. Schlesinger, J. Drenkow, C. Zaleski, S. Jha, P. Batut, M. Chaisson,
1935 and T.R. Gingeras. 2013. STAR: ultrafast universal RNA-seq aligner. *Bioinformatics*.
1936 29:15–21. doi:10.1093/bioinformatics/bts635.

1937 Dopie, J., M.J. Sweredoski, A. Moradian, and A.S. Belmont. 2020. Tyramide signal
1938 amplification mass spectrometry (TSA-MS) ratio identifies nuclear speckle proteins.
1939 *J. Cell Biol*. 219:e201910207. doi:10.1083/jcb.201910207.

1940 Egloff, S., and S. Murphy. 2008. Cracking the RNA polymerase II CTD code. *Trends Genet*.
1941 24:280–288. doi:10.1016/j.tig.2008.03.008.

1942 Ester, M., H.-P. Kriegel, J. Sander, and X. Xu. 1996. A density-based algorithm for discovering
1943 clusters in large spatial databases with noise. *In* Proceedings of the Second
1944 International Conference on Knowledge Discovery and Data Mining. AAAI Press,
1945 Portland, Oregon. 226–231.

1946 Fan, J., B. Kuai, K. Wang, L. Wang, Y. Wang, X. Wu, B. Chi, G. Li, and H. Cheng. 2018. mRNAs
1947 are sorted for export or degradation before passing through nuclear speckles.
1948 *Nucleic Acids Res*. 46:8404–8416. doi:10.1093/nar/gky650.

1949 Fei, J., M. Jadaliha, T.S. Harmon, I.T.S. Li, B. Hua, Q. Hao, A.S. Holehouse, M. Reyer, Q. Sun,
1950 S.M. Freier, R.V. Pappu, K.V. Prasanth, and T. Ha. 2017. Quantitative analysis of
1951 multilayer organization of proteins and RNA in nuclear speckles at super resolution.
1952 *J. Cell Sci*. 130:4180–4192. doi:10.1242/jcs.206854.

Gatfield, D., H. Le Hir, C. Schmitt, I.C. Braun, T. Köcher, M. Wilm, and E. Izaurralde. 2001. The DExH/D box protein HEL/UAP56 is essential for mRNA nuclear export in Drosophila. *Curr. Biol.* 11:1716–1721. doi:10.1016/S0960-9822(01)00532-2.

Gholamalamdari, O., T. Van Schaik, Y. Wang, P. Kumar, L. Zhang, Y. Zhang, G.A.H. Gonzalez, A.E. Vouzas, P.A. Zhao, D.M. Gilbert, J. Ma, B. Van Steensel, and A.S. Belmont. 2025. Beyond A and B Compartments: how major nuclear locales define nuclear genome organization and function. doi:10.7554/eLife.99116.2.

Hall, L.L., K.P. Smith, M. Byron, and J.B. Lawrence. 2006. Molecular anatomy of a speckle. *Anat Rec Discov Mol Cell Evol Biol*. 288:664–75.

Harris, C.R., K.J. Millman, S.J. Van Der Walt, R. Gommers, P. Virtanen, D. Cournapeau, E. Wieser, J. Taylor, S. Berg, N.J. Smith, R. Kern, M. Picus, S. Hoyer, M.H. Van Kerkwijk, M. Brett, A. Haldane, J.F. Del Río, M. Wiebe, P. Peterson, P. Gérard-Marchant, K. Sheppard, T. Reddy, W. Weckesser, H. Abbasi, C. Gohlke, and T.E. Oliphant. 2020. Array programming with NumPy. *Nature*. 585:357–362. doi:10.1038/s41586-020-2649-2.

Hermanson, G.T. 2013. Bioconjugate Techniques. Third edition. Academic Press, an imprint of Elsevier, Amsterdam Boston Heidelberg. 1 pp.

Hondele, M., R. Sachdev, S. Heinrich, J. Wang, P. Vallotton, B.M.A. Fontoura, and K. Weis. 2019. DEAD-box ATPases are global regulators of phase-separated organelles. *Nature*. 573:144–148. doi:10.1038/s41586-019-1502-y.

Hu, Y., I. Kireev, M. Plutz, N. Ashourian, and A.S. Belmont. 2009. Large-scale chromatin structure of inducible genes: transcription on a condensed, linear template. *J. Cell Biol.* 185:87–100. doi:10.1083/jcb.200809196.

Hunter, J.D. 2007. Matplotlib: A 2D Graphics Environment. *Comput. Sci. Eng.* 9:90–95. doi:10.1109/mcse.2007.55.

Iborra, F.J., A. Pombo, D.A. Jackson, and P.R. Cook. 1996. Active RNA polymerases are localized within discrete transcription ‘factories’ in human nuclei. *J. Cell Sci.* 109:1427–1436. doi:10.1242/jcs.109.6.1427.

Ilik, İ.A., M. Malszycki, A.K. Lübke, C. Schade, D. Meierhofer, and T. Aktaş. 2020. SON and SRRM2 are essential for nuclear speckle formation. *eLife*. 9:e60579. doi:10.7554/eLife.60579.

Irgen-Gioro, S., S. Yoshida, V. Walling, and S. Chong. 2022. Fixation can change the appearance of phase separation in living cells. *eLife*. 11:e79903. doi:10.7554/eLife.79903.

Ito, M., C.-X. Yuan, S. Malik, W. Gu, J.D. Fondell, S. Yamamura, Z.-Y. Fu, X. Zhang, J. Qin, and R.G. Roeder. 1999. Identity between TRAP and SMCC Complexes Indicates Novel Pathways for the Function of Nuclear Receptors and Diverse Mammalian Activators. *Mol. Cell*. 3:361–370. doi:10.1016/S1097-2765(00)80463-3.

Jackson, D.A., A.B. Hassan, R.J. Errington, and P.R. Cook. 1993. Visualization of focal sites of transcription within human nuclei. *EMBO J.* 12:1059–1065. doi:10.1002/j.1460-2075.1993.tb05747.x.

JavanMoghadam-Kamrani, S., and K. Keyomarsi. 2008. Synchronization of the cell cycle using Lovastatin. *Cell Cycle*. 7:2434–2440. doi:10.4161/cc.6364.

Jensen, T.H., J. Boulay, M. Rosbash, and D. Libri. 2001. The DECD box putative ATPase Sub2p is an early mRNA export factor. *Curr. Biol.* 11:1711–1715. doi:10.1016/S0960-9822(01)00529-2.

Joo, J., S. Cho, S. Hong, S. Min, K. Kim, R. Kumar, J.-M. Choi, Y. Shin, and I. Jung. 2023. Probabilistic establishment of speckle-associated inter-chromosomal interactions. *Nucleic Acids Res.* 51:5377–5395. doi:10.1093/nar/gkad211.

Kang, H.J., H. Eom, H. Kim, K. Myung, H.M. Kwon, and J.H. Choi. 2021. Thrap3 promotes R-loop resolution via interaction with methylated DDX5. *Exp. Mol. Med.* 53:1602–1611. doi:10.1038/s12276-021-00689-6.

Khanna, N., Y. Hu, and A.S. Belmont. 2014. HSP70 transgene directed motion to nuclear speckles facilitates heat shock activation. *Curr. Biol. CB*. 24:1138–44. doi:10.1016/j.cub.2014.03.053.

Khyzha, N., K. Ahmad, and S. Henikoff. 2025. Profiling transcriptome composition and dynamics within nuclear compartments using SLAM-RT&Tag. *Mol. Cell*. 85:1366-1380.e4. doi:10.1016/j.molcel.2025.02.012.

Kim, J., G.A.H. Gonzalez, N.C. Venkata, K.Y. Han, and A.S. Belmont. 2025. Nonrandom interchromatin trafficking through dynamic multiphase speckle connections. doi:10.1101/2025.05.23.655761.

Kim, J., K.Y. Han, N. Khanna, T. Ha, and A.S. Belmont. 2019. Nuclear speckle fusion via long-range directional motion regulates speckle morphology after transcriptional inhibition. *J. Cell Sci.* jcs.226563. doi:10.1242/jcs.226563.

Kim, J., N.C. Venkata, G.A. Hernandez Gonzalez, N. Khanna, and A.S. Belmont. 2020. Gene expression amplification by nuclear speckle association. *J Cell Biol*. 219. doi:10.1083/jcb.201904046.

Kleinridders, A., H.-M. Pogoda, S. Irlenbusch, N. Smyth, C. Koncz, M. Hammerschmidt, and J.C. Brüning. 2009. PLRG1 Is an Essential Regulator of Cell Proliferation and

2022 Apoptosis during Vertebrate Development and Tissue Homeostasis. *Mol. Cell. Biol.*
2023 29:3173–3185. doi:10.1128/MCB.01807-08.

2024 Kota, K.P., S.R. Wagner, E. Huerta, J.M. Underwood, and J.A. Nickerson. 2008. Binding of
2025 ATP to UAP56 is necessary for mRNA export. *J. Cell Sci.* 121:1526–1537.
2026 doi:10.1242/jcs.021055.

2027 Kumar, P., O. Gholamalamdari, Y. Zhang, L. Zhang, A. Vertii, T. Van Schaik, D. Peric-Hupkes,
2028 T. Sasaki, D.M. Gilbert, B. Van Steensel, J. Ma, P.D. Kaufman, and A.S. Belmont.
2029 2024. Nucleolus and centromere Tyramide Signal Amplification-Seq reveals variable
2030 localization of heterochromatin in different cell types. *Commun. Biol.* 7:1135.
2031 doi:10.1038/s42003-024-06838-7.

2032 Lafontaine, D.L.J., J.A. Riback, R. Bascetin, and C.P. Brangwynne. 2021. The nucleolus as a
2033 multiphase liquid condensate. *Nat. Rev. Mol. Cell Biol.* 22:165–182.
2034 doi:10.1038/s41580-020-0272-6.

2035 Lee, K.-M., I.-W. Hsu, and W.-Y. Tarn. 2010. TRAP150 activates pre-mRNA splicing and
2036 promotes nuclear mRNA degradation. *Nucleic Acids Res.* 38:3340–3350.
2037 doi:10.1093/nar/gkq017.

2038 Lee, K.-M., and W.-Y. Tarn. 2014. TRAP150 activates splicing in composite terminal exons.
2039 *Nucleic Acids Res.* 42:12822–12832. doi:10.1093/nar/gku963.

2040 Levi, V., Q. Ruan, M. Plutz, A.S. Belmont, and E. Gratton. 2005. Chromatin Dynamics in
2041 Interphase Cells Revealed by Tracking in a Two-Photon Excitation Microscope.
2042 *Biophys J*. 89:4275–4285. doi:10.1529/biophysj.105.066670.

2043 Li, Y., M. Mund, P. Hoess, J. Deschamps, U. Matti, B. Nijmeijer, V.J. Sabinina, J. Ellenberg, I.
2044 Schoen, and J. Ries. 2018. Real-time 3D single-molecule localization using
2045 experimental point spread functions. *Nat. Methods*. 15:367–369.
2046 doi:10.1038/nmeth.4661.

2047 Llères, D., M. Denegri, M. Biggiogera, P. Ajuh, and A.I. Lamond. 2010. Direct interaction
2048 between hnRNP-M and CDC5L/PLRG1 proteins affects alternative splice site
2049 choice. *EMBO Rep.* 11:445–451. doi:10.1038/embor.2010.64.

2050 Love, M.I., W. Huber, and S. Anders. 2014. Moderated estimation of fold change and
2051 dispersion for RNA-seq data with DESeq2. *Genome Biol.* 15. doi:10.1186/s13059-
2052 014-0550-8.

2053 Luo, M.-J., Z. Zhou, K. Magni, C. Christoforides, J. Rappsilber, M. Mann, and R. Reed. 2001.
2054 Pre-mRNA splicing and mRNA export linked by direct interactions between UAP56
2055 and Aly. *Nature*. 413:644–647. doi:10.1038/35098106.

Marshall, W.F., A. Straight, J.F. Marko, J. Swedlow, A. Dernburg, A. Belmont, A.W. Murray, D.A. Agard, and J.W. Sedat. 1997. Interphase chromosomes undergo constrained diffusional motion in living cells. *Curr Biol*. 7:930–9.

Martin, S., and A. Pombo. 2003. Transcription factories: quantitative studies of nanostructures in the mammalian nucleus. *Chromosome Res.* 11:461–470. doi:10.1023/A:1024926710797.

Miao, H., F. Wu, Y. Li, C. Qin, Y. Zhao, M. Xie, H. Dai, H. Yao, H. Cai, Q. Wang, X. Song, and L. Li. 2022. MALAT1 modulates alternative splicing by cooperating with the splicing factors PTBP1 and PSF. *Sci. Adv.* 8. doi:10.1126/sciadv.abq7289.

Mor, A., S. Suliman, R. Ben-Yishay, S. Yunger, Y. Brody, and Y. Shav-Tal. 2010. Dynamics of single mRNP nucleocytoplasmic transport and export through the nuclear pore in living cells. *Nat. Cell Biol.* 12:543–552. doi:10.1038/ncb2056.

Nguyen, V. 1996. In vivo degradation of RNA polymerase II largest subunit triggered by alpha-amanitin. *Nucleic Acids Res.* 24:2924–2929. doi:10.1093/nar/24.15.2924.

Otsu, N. 1979. A Threshold Selection Method from Gray-Level Histograms. *IEEE Trans. Syst. Man Cybern.* 9:62–66. doi:10.1109/tsmc.1979.4310076.

Pérez-Calero, C., A. Bayona-Feliu, X. Xue, S.I. Barroso, S. Muñoz, V.M. González-Basallote, P. Sung, and A. Aguilera. 2020. UAP56/DDX39B is a major cotranscriptional RNA–DNA helicase that unwinds harmful R loops genome-wide. *Genes Dev.* 34:898–912. doi:10.1101/gad.336024.119.

Pombo, A. 1999. Regional specialization in human nuclei: visualization of discrete sites of transcription by RNA polymerase III. *EMBO J.* 18:2241–2253. doi:10.1093/emboj/18.8.2241.

Pontén, F., M. Gry, L. Fagerberg, E. Lundberg, A. Asplund, L. Berglund, P. Oksvold, E. Björling, S. Hober, C. Kampf, S. Navani, P. Nilsson, J. Ottosson, A. Persson, H. Wernérus, K. Wester, and M. Uhlén. 2009. A global view of protein expression in human cells, tissues, and organs. *Mol. Syst. Biol.* 5:337. doi:10.1038/msb.2009.93.

Quinodoz, S.A., N. Ollikainen, B. Tabak, A. Palla, J.M. Schmidt, E. Detmar, M.M. Lai, A.A. Shishkin, P. Bhat, Y. Takei, V. Trinh, E. Aznauryan, P. Russell, C. Cheng, M. Jovanovic, A. Chow, L. Cai, P. McDonel, M. Garber, and M. Guttman. 2018. Higher-Order Inter-chromosomal Hubs Shape 3D Genome Organization in the Nucleus. *Cell*. 174:744-757 e24. doi:10.1016/j.cell.2018.05.024.

Ries, J. 2020. SMAP: a modular super-resolution microscopy analysis platform for SMLM data. *Nat. Methods*. 17:870–872. doi:10.1038/s41592-020-0938-1.

Schindelin, J., I. Arganda-Carreras, E. Frise, V. Kaynig, M. Longair, T. Pietzsch, S. Preibisch, C. Rueden, S. Saalfeld, B. Schmid, J.-Y. Tinevez, D.J. White, V. Hartenstein, K. Eliceiri, P. Tomancak, and A. Cardona. 2012. Fiji: an open-source platform for biological-image analysis. *Nat. Methods*. 9:676–682. doi:10.1038/nmeth.2019.

Shang, Y., T. Jiang, L. Ran, W. Hu, Y. Wu, J. Ye, Z. Peng, L. Chen, and R. Wang. 2022. TET2–BCLAF1 transcription repression complex epigenetically regulates the expression of colorectal cancer gene Ascl2 via methylation of its promoter. *J. Biol. Chem*. 298:102095. doi:10.1016/j.jbc.2022.102095.

Sharma, A., H. Takata, K. Shibahara, A. Bubulya, and P.A. Bubulya. 2010. Son Is Essential for Nuclear Speckle Organization and Cell Cycle Progression. *Mol. Biol. Cell*. 21:650–663. doi:10.1091/mbc.e09-02-0126.

Shen, H., X. Zheng, J. Shen, L. Zhang, R. Zhao, and M.R. Green. 2008. Distinct activities of the DExD/H-box splicing factor hUAP56 facilitate stepwise assembly of the spliceosome. *Genes Dev.* 22:1796–1803. doi:10.1101/gad.1657308.

Smith, K.P., L.L. Hall, and J.B. Lawrence. 2020. Nuclear hubs built on RNAs and clustered organization of the genome. *Curr. Opin. Cell Biol*. 64:67–76. doi:10.1016/j.ceb.2020.02.015.

Smith, K.P., P.T. Moen, K.L. Wydner, J.R. Coleman, and J.B. Lawrence. 1999. Processing of endogenous pre-mRNAs in association with SC-35 domains is gene specific. *J Cell Biol*. 144:617–29.

Solovei, I., and M. Cremer. 2010. 3D-FISH on cultured cells combined with immunostaining. *Methods Mol. Biol. Clifton NJ*. 659:117–126. doi:10.1007/978-1-60761-789-1_8.

Spector, D.L., and A.I. Lamond. 2011. Nuclear Speckles. *Cold Spring Harb. Perspect. Biol.* 3:a000646–a000646. doi:10.1101/cshperspect.a000646.

Su, J.H., P. Zheng, S.S. Kinrot, B. Bintu, and X. Zhuang. 2020. Genome-Scale Imaging of the 3D Organization and Transcriptional Activity of Chromatin. *Cell*. 182:1641-1659 e26. doi:10.1016/j.cell.2020.07.032.

Takei, Y., Y. Yang, J. White, J. Yun, M. Prasad, L.J. Ombelets, S. Schindler, and L. Cai. 2023. High-resolution spatial multi-omics reveals cell-type specific nuclear compartments. 2023.05.07.539762. doi:10.1101/2023.05.07.539762.

Takei, Y., J. Yun, S. Zheng, N. Ollikainen, N. Pierson, J. White, S. Shah, J. Thomassie, S. Suo, C.L. Eng, M. Guttman, G.C. Yuan, and L. Cai. 2021. Integrated spatial genomics reveals global architecture of single nuclei. *Nature*. 590:344–350. doi:10.1038/s41586-020-03126-2.

Taniguchi, I., and M. Ohno. 2008. ATP-Dependent Recruitment of Export Factor Aly/REF onto Intronless mRNAs by RNA Helicase UAP56. *Mol. Cell. Biol.* 28:601–608. doi:10.1128/MCB.01341-07.

Titov, D.V., B. Gilman, Q.-L. He, S. Bhat, W.-K. Low, Y. Dang, M. Smeaton, A.L. Demain, P.S. Miller, J.F. Kugel, J.A. Goodrich, and J.O. Liu. 2011. XPB, a subunit of TFIIH, is a target of the natural product triptolide. *Nat. Chem. Biol.* 7:182–188. doi:10.1038/nchembio.522.

Van Der Walt, S., J.L. Schönberger, J. Nunez-Iglesias, F. Boulogne, J.D. Warner, N. Yager, E. Gouillart, and T. Yu. 2014. scikit-image: image processing in Python. *PeerJ*. 2:e453. doi:10.7717/peerj.453.

Varia, S., D. Potabathula, Z. Deng, A. Bubulya, and P.A. Bubulya. 2013. Btf and TRAP150 have distinct roles in regulating subcellular mRNA distribution. *Nucleus*. 4:229–240. doi:10.4161/nucl.25187.

Vohhodina, J., E.M. Barros, A.L. Savage, F.G. Liberante, L. Manti, P. Bankhead, N. Cosgrove, A.F. Madden, D.P. Harkin, and K.I. Savage. 2017. The RNA processing factors THRAP3 and BCLAF1 promote the DNA damage response through selective mRNA splicing and nuclear export. *Nucleic Acids Res.* 45:12816–12833. doi:10.1093/nar/gkx1046.

Wang, K., L. Wang, J. Wang, S. Chen, M. Shi, and H. Cheng. 2018. Intronless mRNAs transit through nuclear speckles to gain export competence. *J. Cell Biol.* 217:3912–3929. doi:10.1083/jcb.201801184.

Wang, Y., Y. Zhang, R. Zhang, T. van Schaik, L. Zhang, T. Sasaki, D. Peric-Hupkes, Y. Chen, D.M. Gilbert, B. van Steensel, A.S. Belmont, and J. Ma. 2021. SPIN reveals genome-wide landscape of nuclear compartmentalization. *Genome Biol*. 22:36. doi:10.1186/s13059-020-02253-3.

Wu, J., Y. Xiao, Y. Liu, L. Wen, C. Jin, S. Liu, S. Paul, C. He, O. Regev, and J. Fei. 2024. Dynamics of RNA localization to nuclear speckles are connected to splicing efficiency. *Sci. Adv.* 10:eadp7727. doi:10.1126/sciadv.adp7727.

Xie, S.Q., S. Martin, P.V. Guillot, D.L. Bentley, and A. Pombo. 2006. Splicing Speckles Are Not Reservoirs of RNA Polymerase II, but Contain an Inactive Form, Phosphorylated on Serine[2] Residues of the C-Terminal Domain. *Mol. Biol. Cell*. 17:1723–1733. doi:10.1091/mbc.e05-08-0726.

Xie, Y., S. Gao, K. Zhang, P. Bhat, B.P. Clarke, K. Batten, M. Mei, M. Gazzara, J.W. Shay, K.W. Lynch, A.E. Angelos, P.S. Hill, A.L. Ivey, B.M.A. Fontoura, and Y. Ren. 2023. Structural basis for high-order complex of SARNP and DDX39B to facilitate mRNP assembly. *Cell Rep.* 42:112988. doi:10.1016/j.celrep.2023.112988.

Xu, Z., X. Li, H. Li, C. Nie, W. Liu, S. Li, Z. Liu, W. Wang, and J. Wang. 2020. Suppression of DDX39B sensitizes ovarian cancer cells to DNA-damaging chemotherapeutic agents via destabilizing BRCA1 mRNA. *Oncogene*. 39:7051–7062. doi:10.1038/s41388-020-01482-x.

Yankulov, K., K. Yamashita, R. Roy, J.-M. Egly, and D.L. Bentley. 1995. The Transcriptional Elongation Inhibitor 5,6-Dichloro-1-β-D-ribofuranosylbenzimidazole Inhibits Transcription Factor IIH-associated Protein Kinase. *J. Biol. Chem.* 270:23922–23925. doi:10.1074/jbc.270.41.23922.

Yesbolatova, A., Y. Saito, N. Kitamoto, H. Makino-Itou, R. Ajima, R. Nakano, H. Nakaoka, K. Fukui, K. Gamo, Y. Tominari, H. Takeuchi, Y. Saga, K. Hayashi, and M.T. Kanemaki. 2020. The auxin-inducible degron 2 technology provides sharp degradation control in yeast, mammalian cells, and mice. *Nat. Commun.* 11. doi:10.1038/s41467-020-19532-z.

Yu, C.-L., T.-W. Chuang, S.Y. Samuel, Y.-C. Lou, and W.-Y. Tarn. 2023a. Co-phase separation of Y14 and RNA in vitro and its implication for DNA repair. *RNA*. 29:1007–1019. doi:10.1261/rna.079514.122.

Yu, R., S. Roseman, A.P. Siegenfeld, S.C. Nguyen, E.F. Joyce, B.B. Liau, I.D. Krantz, K.A. Alexander, and S.L. Berger. 2023b. CTCF/cohesin organize the ground state of chromatin-nuclear speckle association. 2023.07.22.550178. doi:10.1101/2023.07.22.550178.

Zhang, L., Y. Chen, and A.S. Belmont. 2022. Measuring Cytological Proximity of Chromosomal Loci to Defined Nuclear Compartments with TSA-seq. *In* Spatial Genome Organization. T. Sexton, editor. Springer US, New York, NY. 145–186.

Zhang, L., Y. Zhang, Y. Chen, O. Gholamalamdari, Y. Wang, J. Ma, and A.S. Belmont. 2021. TSA-seq reveals a largely conserved genome organization relative to nuclear speckles with small position changes tightly correlated with gene expression changes. *Genome Res.* 31:251–264. doi:10.1101/gr.266239.120.

Zhang, M., Z. Gu, S. Guo, Y. Sun, S. Ma, S. Yang, J. Guo, C. Fang, L. Shu, Y. Ge, Z. Chen, and B. Wang. 2024. SRRM2 phase separation drives assembly of nuclear speckle subcompartments. *Cell Rep.* 43:113827. doi:10.1016/j.celrep.2024.113827.

Zhang, N., R. Kaur, S. Akhter, and R.J. Legerski. 2009. Cdc5L interacts with ATR and is required for the S-phase cell-cycle checkpoint. *EMBO Rep.* 10:1029–1035. doi:10.1038/embor.2009.122.

Zhang, N., R. Kaur, X. Lu, X. Shen, L. Li, and R.J. Legerski. 2005. The Pso4 mRNA Splicing and DNA Repair Complex Interacts with WRN for Processing of DNA Interstrand Cross-links. *J. Biol. Chem.* 280:40559–40567. doi:10.1074/jbc.M508453200.

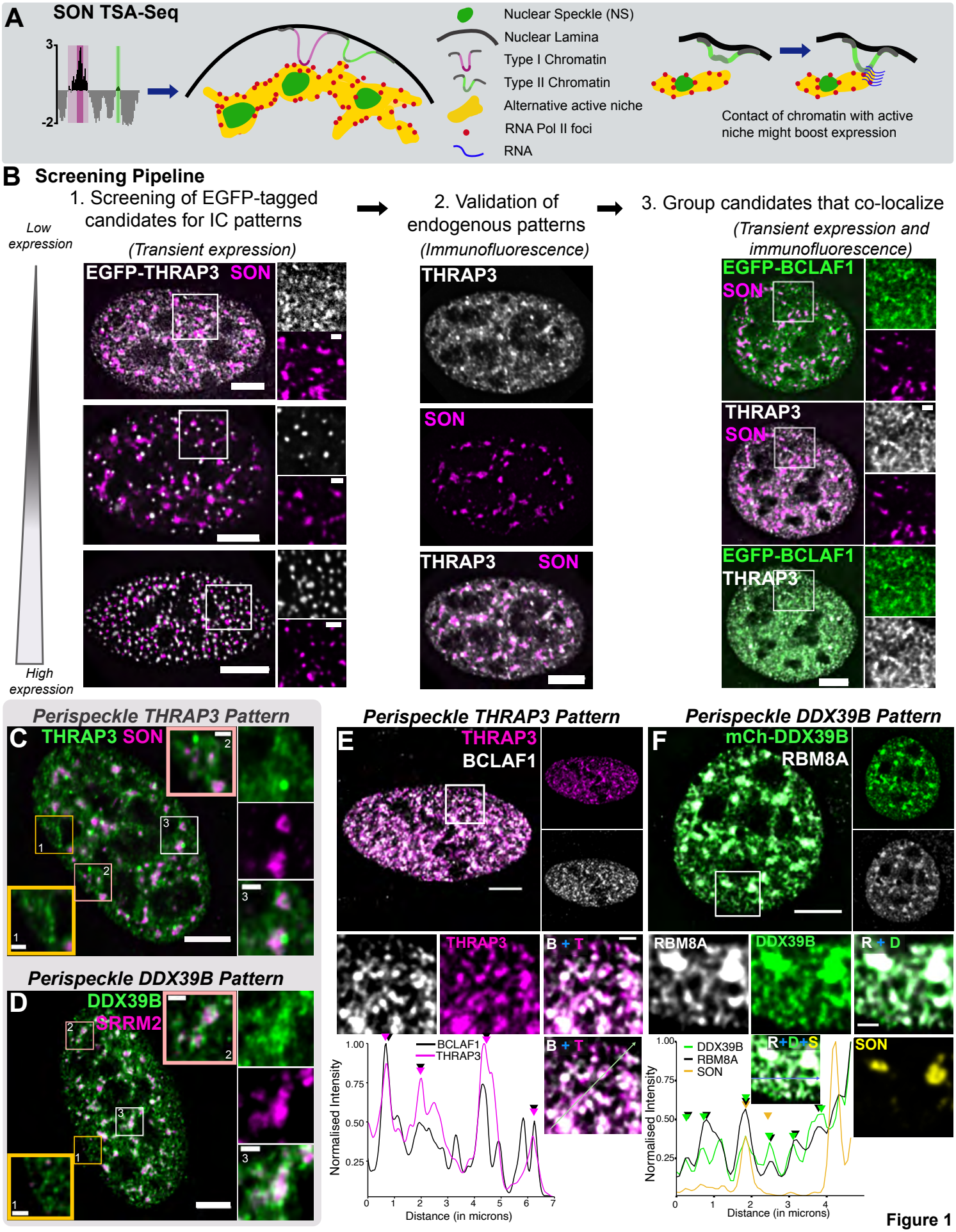
A
SON TSA-Seq
3
-2
Nuclear Speckle (NS)
Nuclear Lamina
Type I Chromatin
Type II Chromatin
Alternative active niche
RNA Pol II foci
RNA
Contact of chromatin with active niche might boost expression
B
Screening Pipeline
1. Screening of EGFP-tagged candidates for IC patterns
(Transient expression)
Low expression
High expression
EGFP-THRAP3 SON
2. Validation of endogenous patterns
(Immunofluorescence)
THRAP3
SON
THRAP3 SON
3. Group candidates that co-localize
(Transient expression and immunofluorescence)
EGFP-BCLAF1
SON
THRAP3
SON
EGFP-BCLAF1
THRAP3
Perispeckle THRAP3 Pattern
C
THRAP3 SON
Perispeckle DDX39B Pattern
D
DDX39B
SRRM2
Perispeckle THRAP3 Pattern
E
THRAP3
BCLAF1
THRAP3
B + T
BCLAF1
THRAP3
Normalised Intensity
Distance (in microns)
Perispeckle DDX39B Pattern
F
mCh-DDX39B
RBM8A
RBM8A
DDX39B
R + D
R+D+S
SON
DDX39B
RBM8A
SON
Normalised Intensity
Distance (in microns)

Figure 1

Single connection: Dynamic over seconds

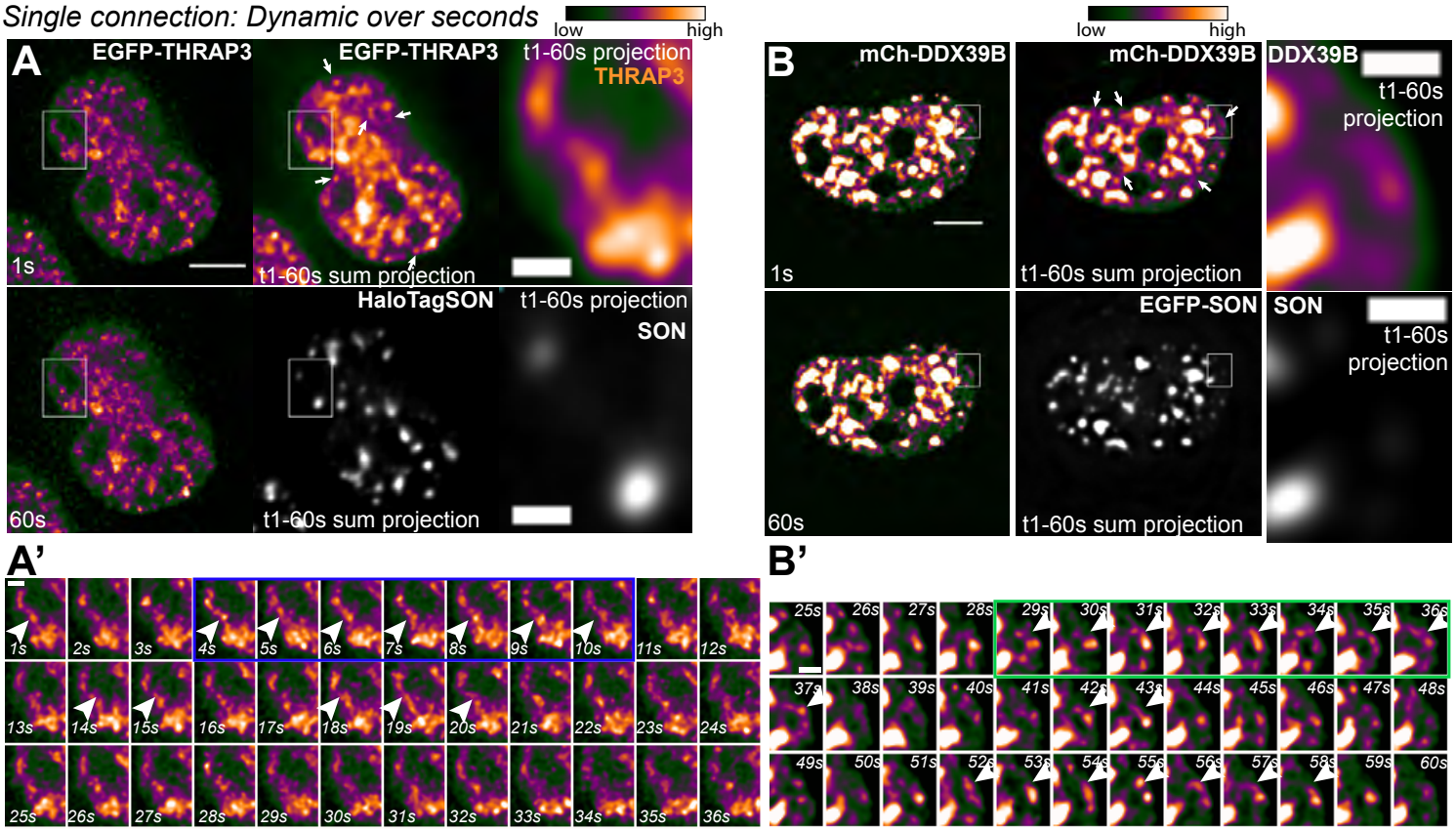

Network: Stable over hours

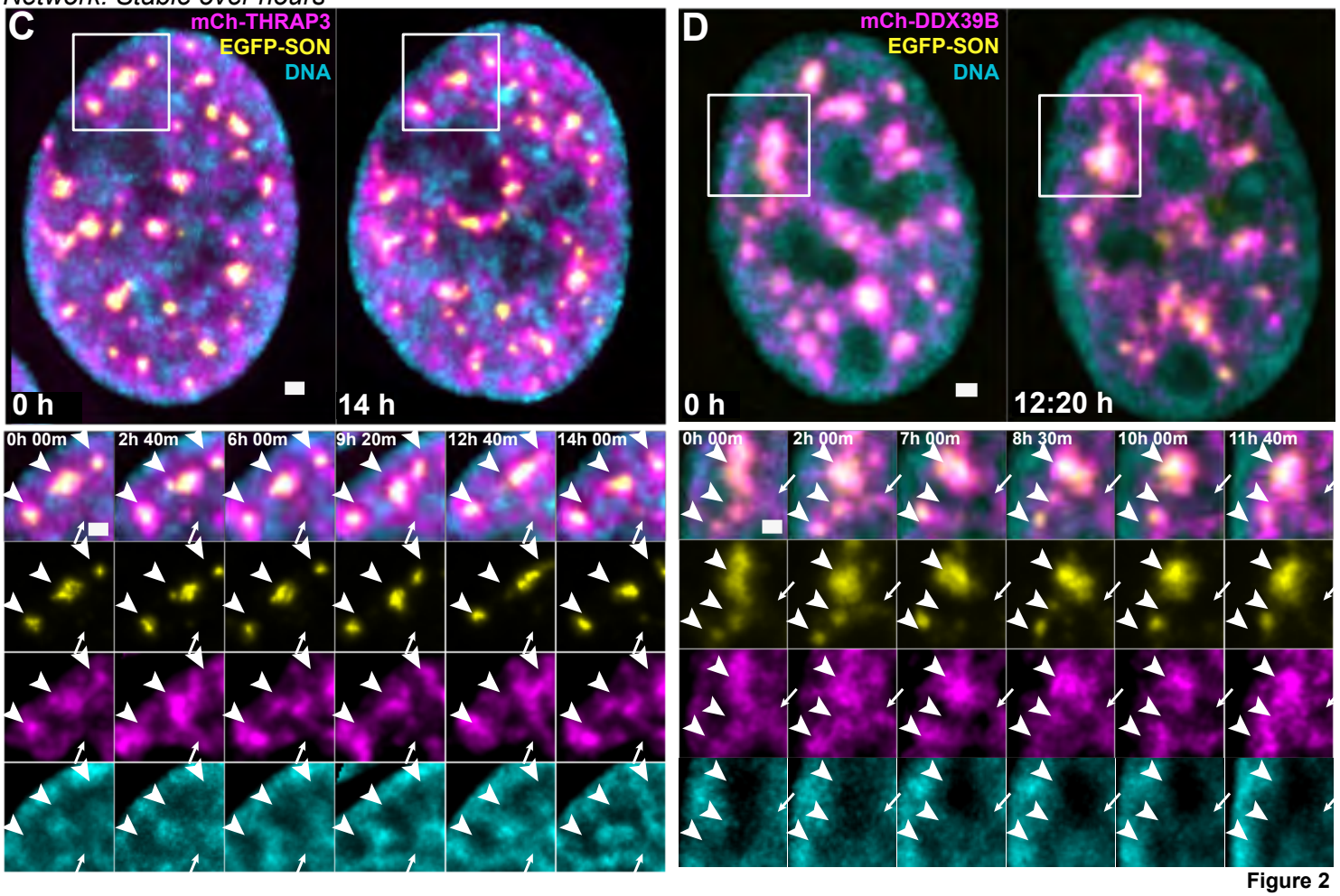

Figure 2

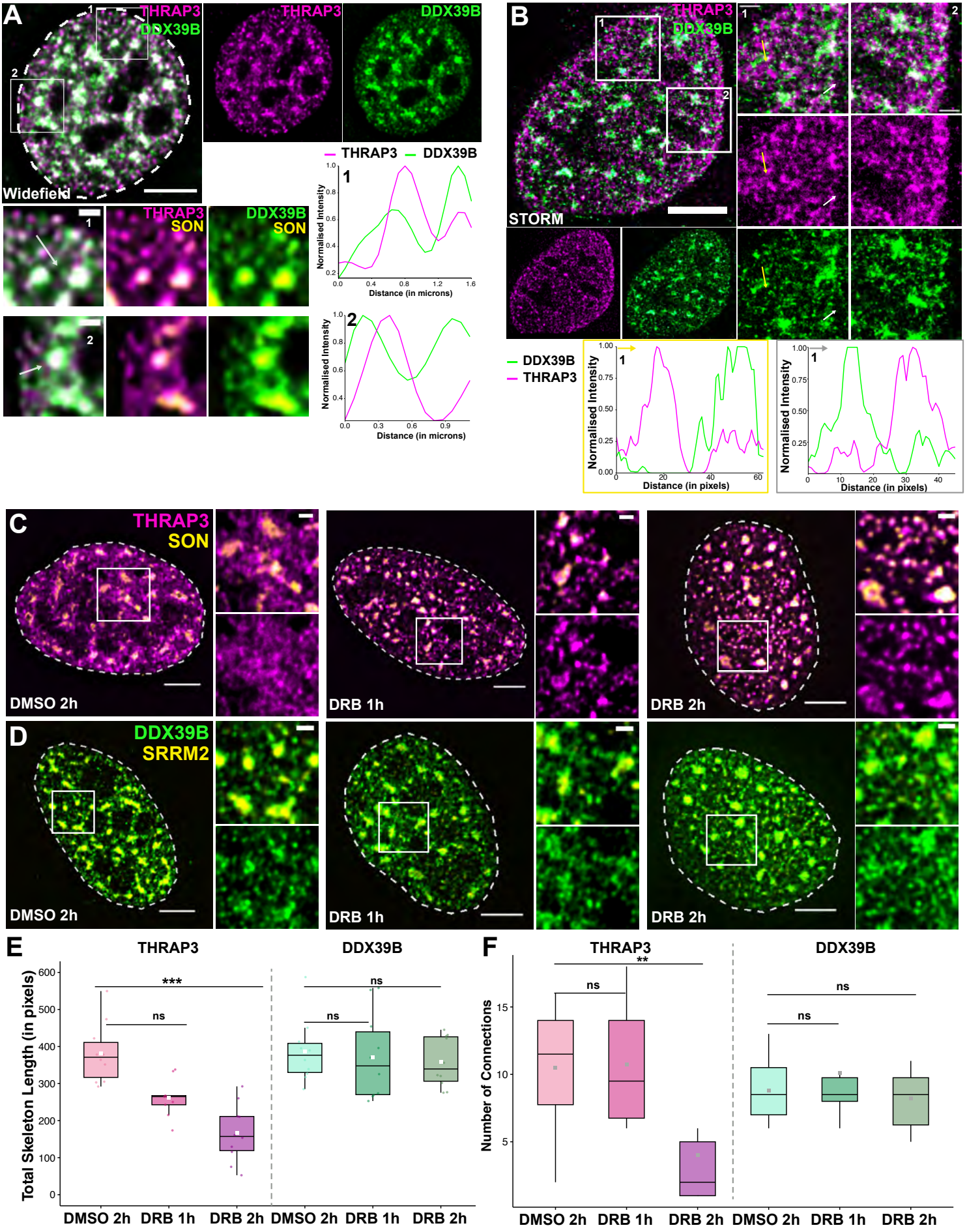
A
THRAP3
DDX39B
Widefield
THRAP3
DDX39B
THRAP3
SON
DDX39B
SON
THRAP3
DDX39B
Normalised Intensity
Distance (in microns)
B
THRAP3
DDX39B
STORM
DDX39B
THRAP3
Normalised Intensity
Distance (in pixels)
C
THRAP3
SON
DMSO 2h
DRB 1h
DRB 2h
D
DDX39B
SRRM2
DMSO 2h
DRB 1h
DRB 2h
E
THRAP3
DDX39B
Total Skeleton Length (in pixels)
***
ns
ns
ns
DMSO 2h
DRB 1h
DRB 2h
DMSO 2h
DRB 1h
DRB 2h
F
THRAP3
DDX39B
Number of Connections
**
ns
ns
ns
DMSO 2h
DRB 1h
DRB 2h
DMSO 2h
DRB 1h
DRB 2h

Figure 3

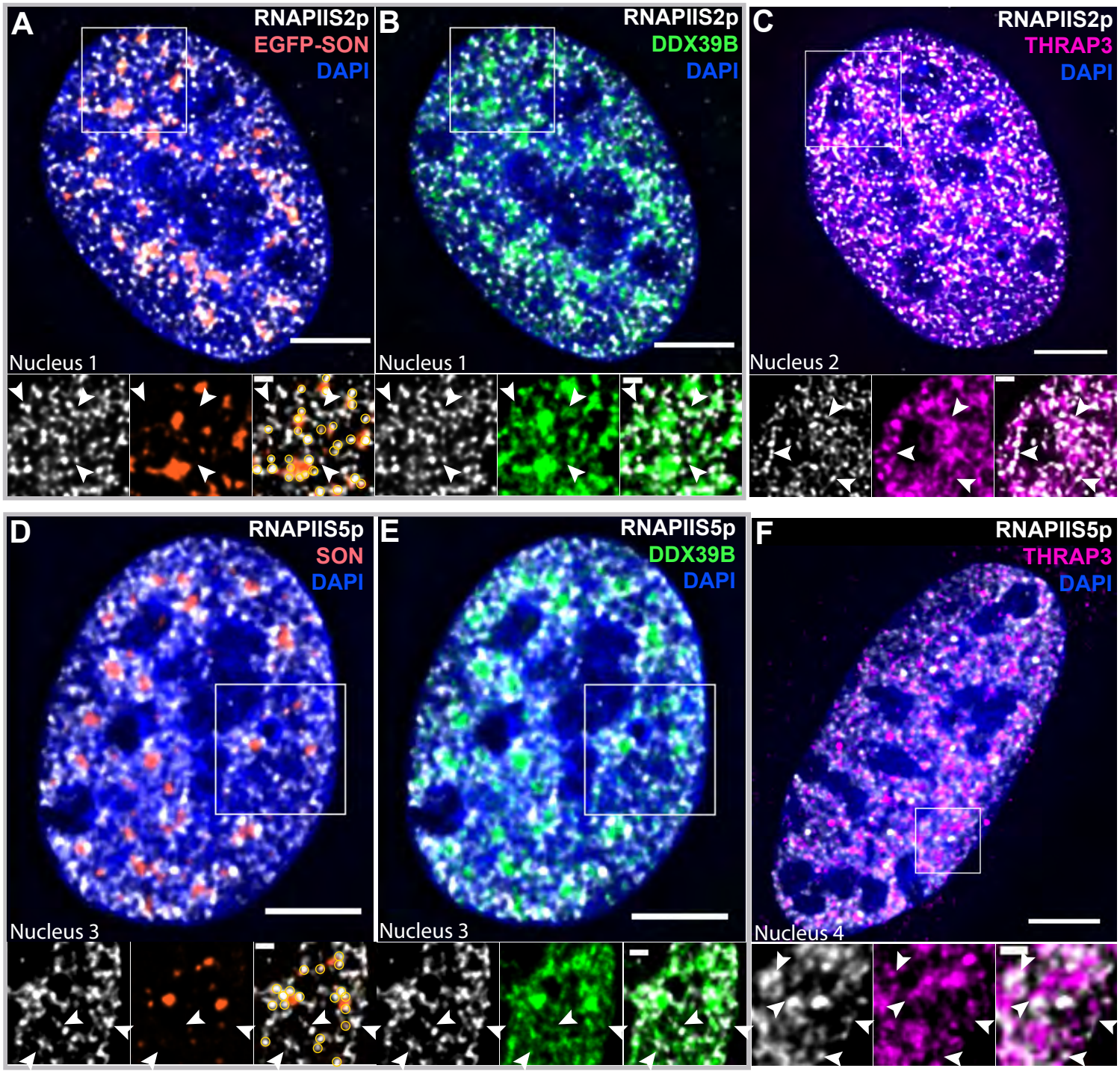
A
RNAPIIS2p
EGFP-SON
DAPI
Nucleus 1
B
RNAPIIS2p
DDX39B
DAPI
Nucleus 1
C
RNAPIIS2p
THRAP3
DAPI
Nucleus 2
D
RNAPIIS5p
SON
DAPI
Nucleus 3
E
RNAPIIS5p
DDX39B
DAPI
Nucleus 3
F
RNAPIIS5p
THRAP3
DAPI
Nucleus 4

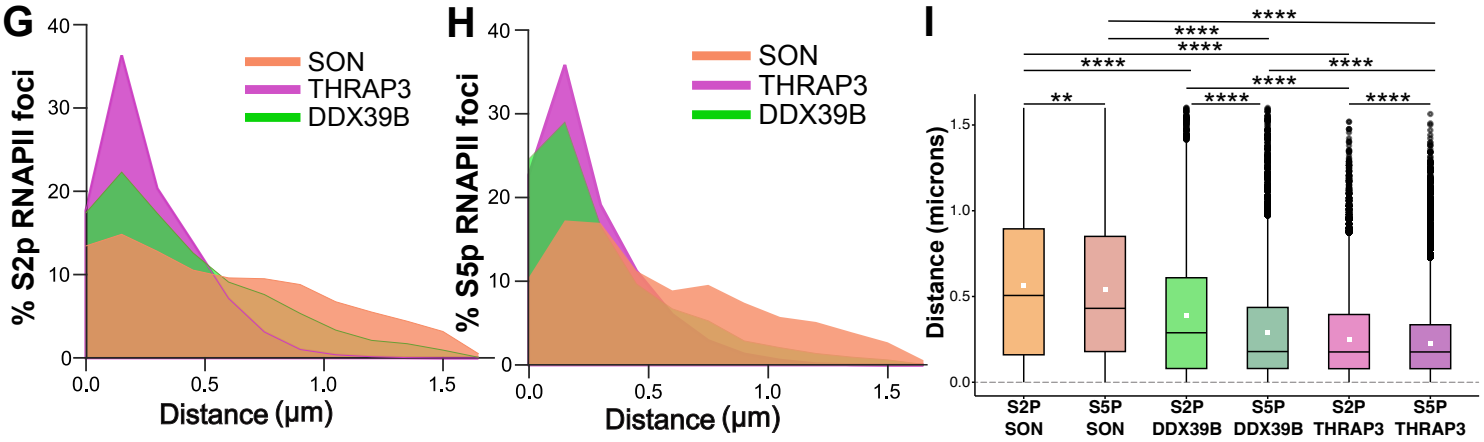
G
% S2p RNAPII foci
Distance (µm)
SON
THRAP3
DDX39B
H
% S5p RNAPII foci
Distance (µm)
SON
THRAP3
DDX39B
I
Distance (microns)
S2P SON
S5P SON
S2P DDX39B
S5P DDX39B
S2P THRAP3
S5P THRAP3

Figure 4

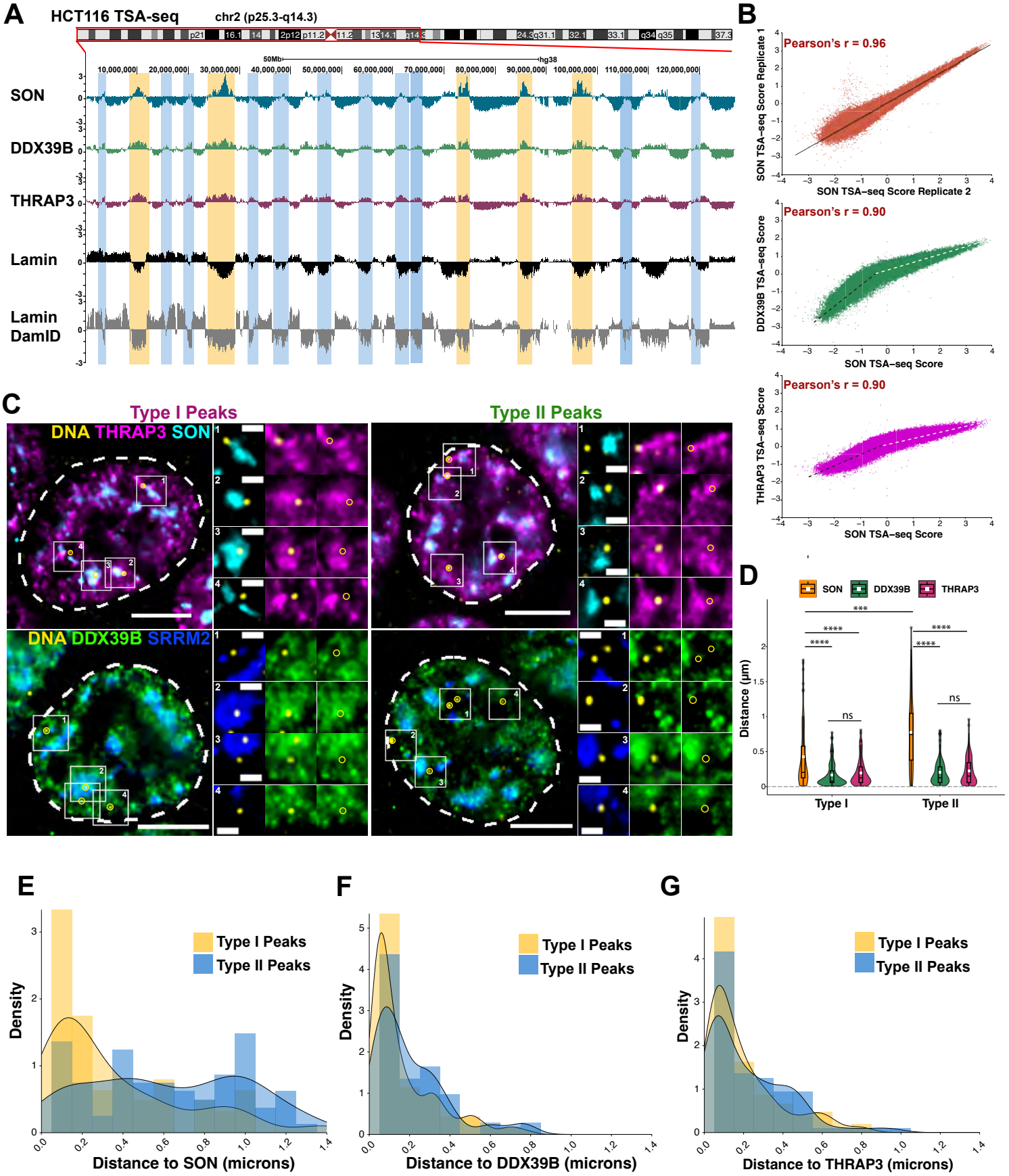
A
HCT116 TSA-seq
chr2 (p25.3-q14.3)
SON
DDX39B
THRAP3
Lamin
Lamin DamID
B
Pearson's r = 0.96
SON TSA-seq Score Replicate 1
SON TSA-seq Score Replicate 2
Pearson's r = 0.90
DDX39B TSA-seq Score
SON TSA-seq Score
Pearson's r = 0.90
THRAP3 TSA-seq Score
SON TSA-seq Score
C
Type I Peaks
Type II Peaks
DNA THRAP3 SON
DNA DDX39B SRRM2
D
SON
DDX39B
THRAP3
Distance (µm)
Type I
Type II
E
Type I Peaks
Type II Peaks
Density
Distance to SON (microns)
F
Type I Peaks
Type II Peaks
Density
Distance to DDX39B (microns)
G
Type I Peaks
Type II Peaks
Density
Distance to THRAP3 (microns)

Figure 5

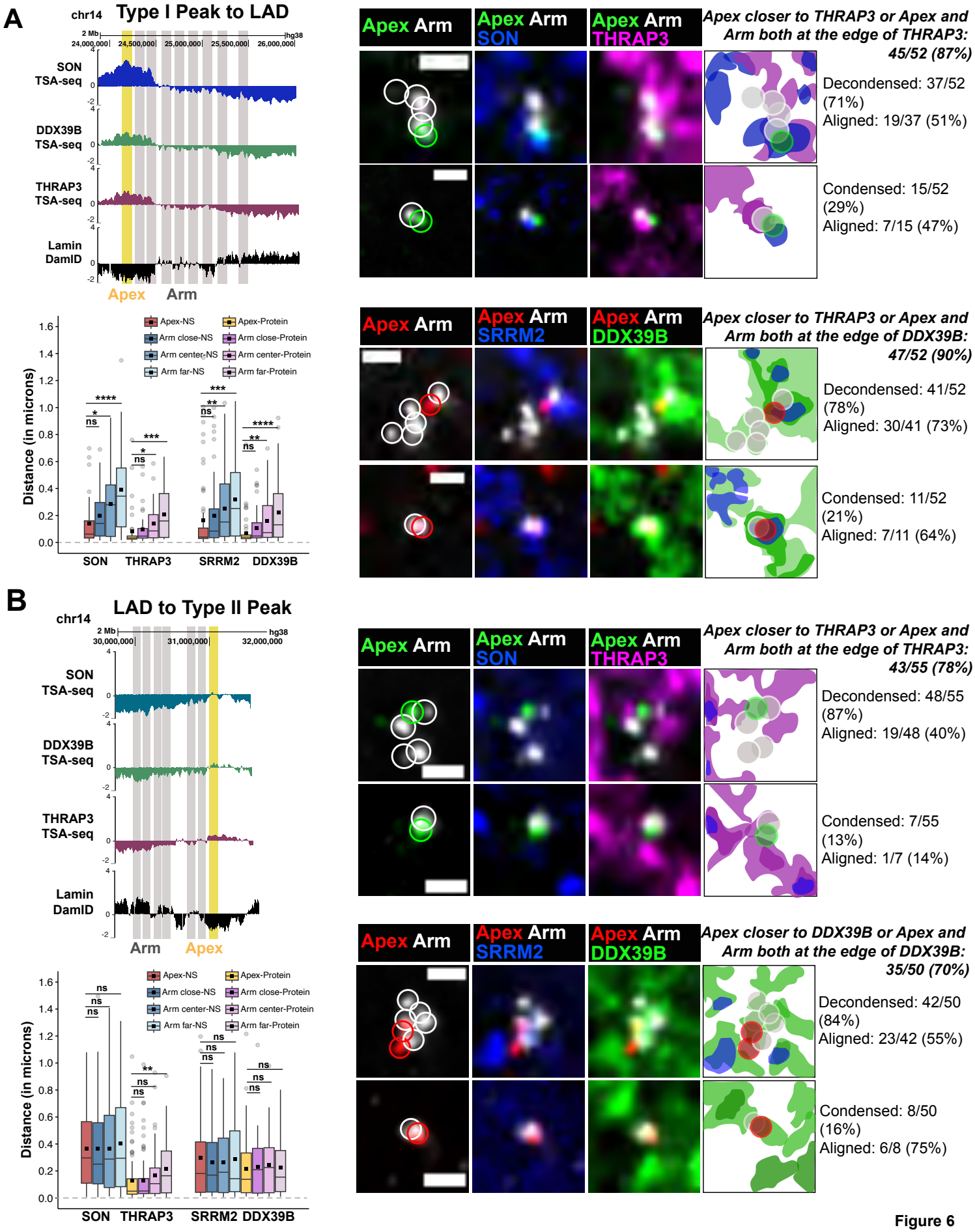
A
chr14
Type I Peak to LAD
2 Mb
hg38
24,000,000
24,500,000
25,000,000
25,500,000
26,000,000
SON TSA-seq
DDX39B TSA-seq
THRAP3 TSA-seq
Lamin DamID
Apex
Arm
Apex-NS
Apex-Protein
Arm close-NS
Arm close-Protein
Arm center-NS
Arm center-Protein
Arm far-NS
Arm far-Protein
Distance (in microns)
SON
THRAP3
SRRM2
DDX39B
Apex Arm
Apex Arm SON
Apex Arm THRAP3
Apex closer to THRAP3 or Apex and Arm both at the edge of THRAP3: 45/52 (87%)
Decondensed: 37/52 (71%)
Aligned: 19/37 (51%)
Condensed: 15/52 (29%)
Aligned: 7/15 (47%)
Apex Arm SRRM2
Apex Arm DDX39B
Apex closer to THRAP3 or Apex and Arm both at the edge of DDX39B: 47/52 (90%)
Decondensed: 41/52 (78%)
Aligned: 30/41 (73%)
Condensed: 11/52 (21%)
Aligned: 7/11 (64%)
B
LAD to Type II Peak
30,000,000
31,000,000
32,000,000
Apex closer to THRAP3 or Apex and Arm both at the edge of THRAP3: 43/55 (78%)
Decondensed: 48/55 (87%)
Aligned: 19/48 (40%)
Condensed: 7/55 (13%)
Aligned: 1/7 (14%)
Apex closer to DDX39B or Apex and Arm both at the edge of DDX39B: 35/50 (70%)
Decondensed: 42/50 (84%)
Aligned: 23/42 (55%)
Condensed: 8/50 (16%)
Aligned: 6/8 (75%)

Figure 6

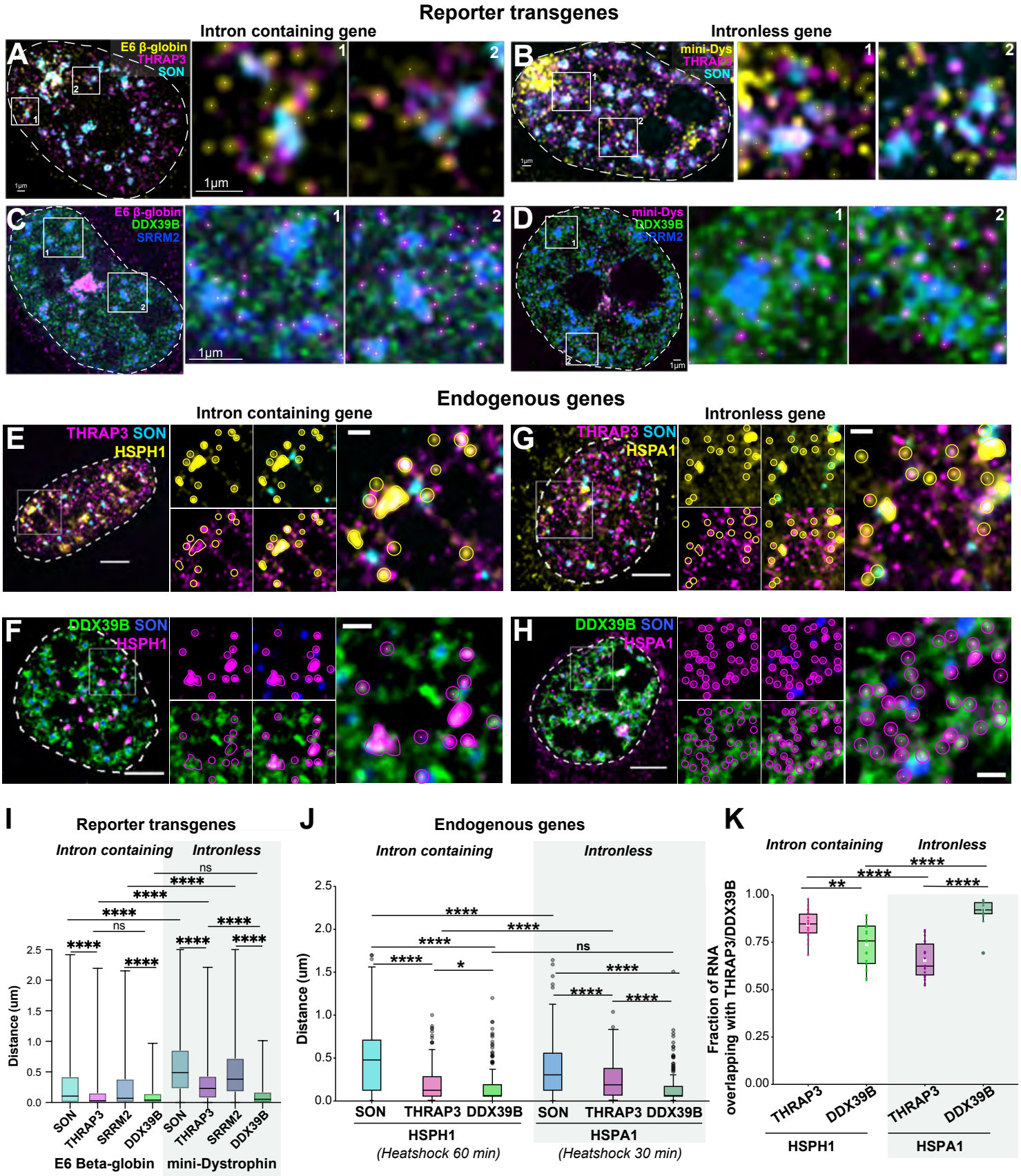
Reporter transgenes
Intron containing gene
Intronless gene
A
E6 β-globin
THRAP3
SON
B
mini-Dys
THRAP3
SON
C
E6 β-globin
DDX39B
SRRM2
D
mini-Dys
DDX39B
SRRM2
1μm
Endogenous genes
Intron containing gene
Intronless gene
E
THRAP3 SON
HSPH1
G
THRAP3 SON
HSPA1
F
DDX39B SON
HSPH1
H
DDX39B SON
HSPA1
I
Reporter transgenes
Intron containing
Intronless
Distance (um)
SON
THRAP3
SRRM2
DDX39B
E6 Beta-globin
mini-Dystrophin
J
Endogenous genes
Intron containing
Intronless
Distance (um)
SON
THRAP3
DDX39B
HSPH1
(Heatshock 60 min)
HSPA1
(Heatshock 30 min)
K
Intron containing
Intronless
Fraction of RNA overlapping with THRAP3/DDX39B
THRAP3
DDX39B
HSPH1
HSPA1

Figure 7

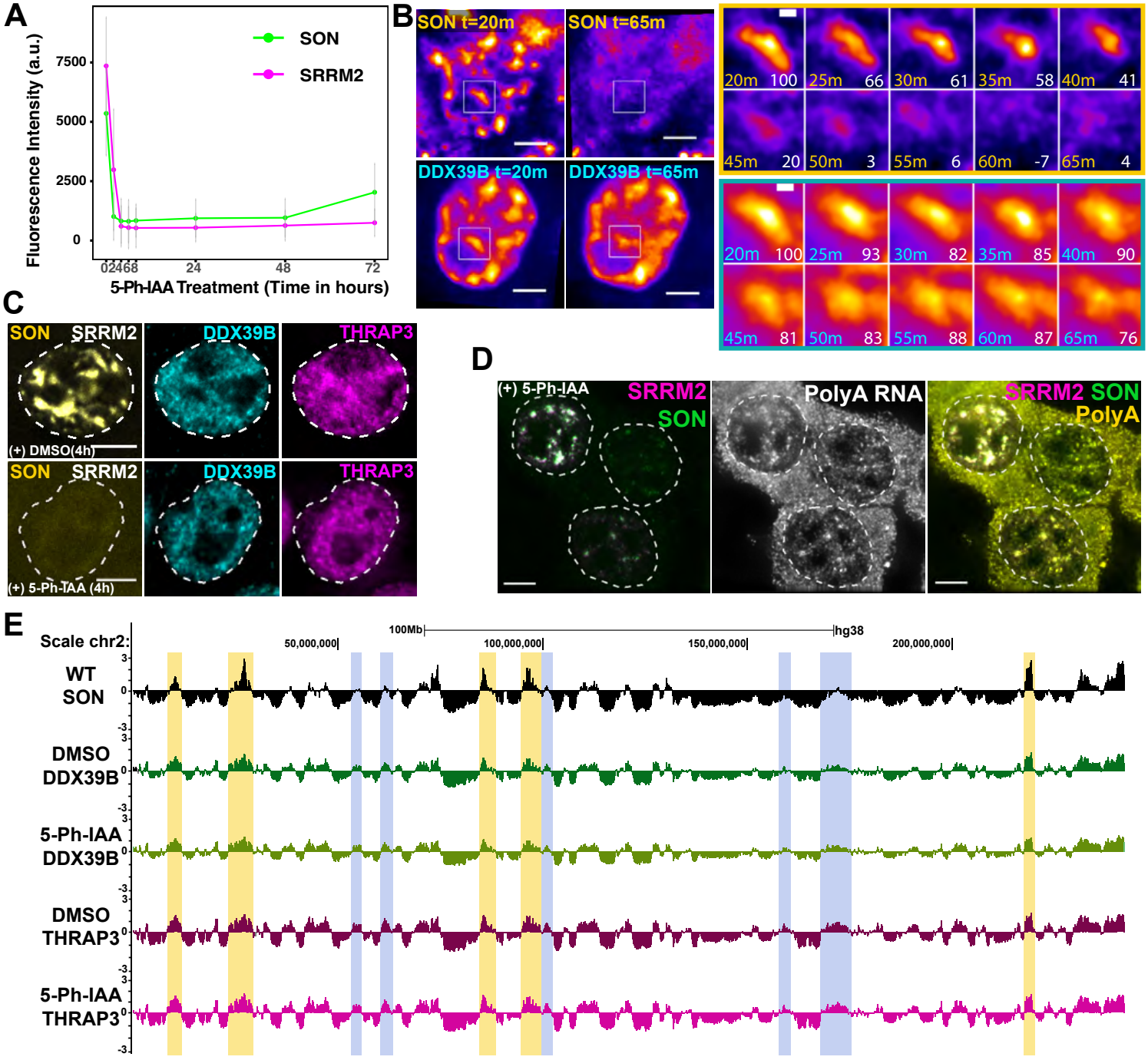
A
Fluorescence Intensity (a.u.)
7500
5000
2500
0
SON
SRRM2
02468
24
48
72
5-Ph-IAA Treatment (Time in hours)
B
SON t=20m
SON t=65m
DDX39B t=20m
DDX39B t=65m
20m 100
25m 66
30m 61
35m 58
40m 41
45m 20
50m 3
55m 6
60m -7
65m 4
20m 100
25m 93
30m 82
35m 85
40m 90
45m 81
50m 83
55m 88
60m 87
65m 76
C
SON
SRRM2
DDX39B
THRAP3
(+) DMSO(4h)
(+) 5-Ph-IAA (4h)
D
(+) 5-Ph-IAA
SRRM2
SON
PolyA RNA
SRRM2 SON
PolyA
E
Scale chr2:
100Mb
hg38
50,000,000
100,000,000
150,000,000
200,000,000
WT SON
DMSO DDX39B
5-Ph-IAA DDX39B
DMSO THRAP3
5-Ph-IAA THRAP3
F
Genes within Type I peaks
Genes within Type II peaks
−log10(FDR)
log FC
G
Genes within Type I peaks
Genes within Type II peaks
123 Upregulated
62 Downregulated
log FC
Mean SON TSA−seq Score
H
Genes within Type I peaks
Genes within Type II peaks
Upregulated 162 192
Downregulated 897 144
log FC
Density

Figure 8

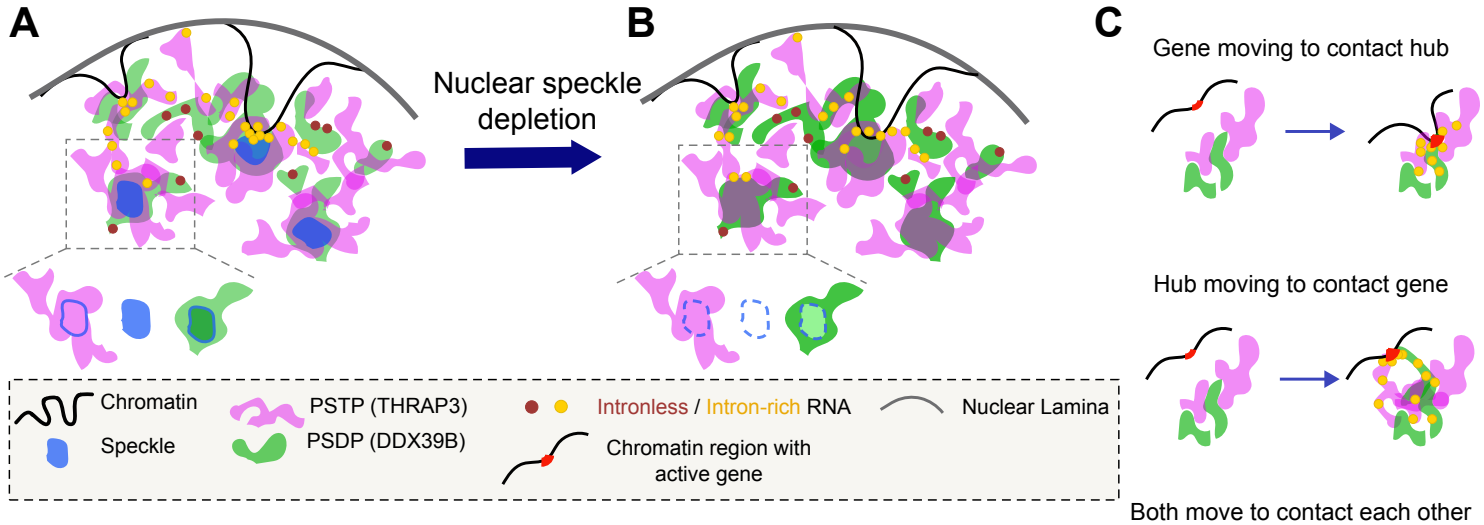

Interchromatin space divided into distinct networks in addition to nuclear speckles.

These networks interact with active DNA.

PSTP and PSDP foci overlap differentially with different subsets of RNPs as they move through the IC space

Networks maintained even after speckles are depleted.

Gene positioning remains unaltered.

Are speckles specialized bodies for added efficiency above the basal function of these networks?

Figure 9